# FIRST-PRINCIPLES STUDY OF LATTICE DYNAMICS IN CRYSTALS

A THESIS

SUBMITTED TO THE FACULTY OF THE GRADUATE SCHOOL

OF THE UNIVERSITY OF MINNESOTA

BY

**SHUTONG LI**

IN PARTIAL FULFILLMENT OF THE REQUIREMENTS

FOR THE DEGREE OF

DOCTOR OF PHILOSOPHY

June, 2022

# Acknowledgments

The past five year have been an adventurous yet interesting journey, which I could not have finished without the help of many people. First I would like to acknowledge my advisor Turan Birol and Bharat Jalan. They are great advisors who offered me generous suggestions, both academic and life. There are many ways to do a good research, but I found their way to be the most proper one for me. Second I would like to thank so many friends in the graduate school, life in the past few years would be tough without you - especially during the pandemic time, which is the most unusual time period I had ever experienced. Then I would like to express my gratitude to my family and my partner. It is your support that encourages me achieve things I would never imagine. Last, I would like to acknowledge National Science Foundation and Minnesota Materials Research Science and Engineering Center, my work is generously sponsored by NSF through these funding numbers: DMR-2011401, DMR-1420013.

## Abstract

Lattice dynamics is a key component in solid state physics. It helps the understanding of many physical properties like structural phase transitions and ferroelectricity. Density functional theory, as a first-principles method, is used to investigate the lattice dynamics in this thesis. Followed by an introduction of density functional theory and lattice dynamics, I first study the strain-suppresed polarization switching barriers in layered perovskites. It is shown that the epitaxial strain is strongly coupled with the free energy of different crystal structures, which enables us to tune the energy difference between stable and transition states. The concept of distortion symmetry group is also utilized here to model the switching process accurately. Second, the idea of free-carriers-induced ferroelectricity is introduced. Free charge carriers is typically detrimental to proper ferroelectricity, but it is not the case for hybrid improper ferroelectrics. This unexpected phenomenon will be explained by the electron-enhancement of oxygen octahedral rotation. Group theory analysis and Landau free energy are also carefully looked into in this system. Third, the nature of chemical bonding in transition metal dichalcogenides (TMD) is investigated using Wannier functions. My DFPT results indicate anomalous ionic charges of $HfS_2$ in the in-plane direction, which is also confirmed by infrared and Raman spectrum from our collaborators. The study of Wannier functions attributes this robust ionicity to the hybridization of Hf and S orbitals. Finally, this dissertation is concluded by a brief comment of future opportunities and challenges in this research field.

# Contents

# List of Figures

# List of Tables

# List of Abbreviations

| | |
|---|---|
| DFT | Density functional theory |
| DFPT | Density functional perturbation theory |
| DM | Dzyaloshinskii–Moriya interaction |
| GGA | Generalized-gradient-approximation |
| HIF | Hybrid improper ferroelectricity |
| Irrep | Irreducible representation |
| MEP | Minimum energy path |
| NEB | Nudged elastic band |
| OOT | Oxygen octahedra tilting |
| OOR | Oxygen octahedra rotation |
| PBE | Perdew-Burke-Ernzerhof |
| RP | Ruddlesden-popper phase perovskite |
| TEM | Transmission electron microscope |

| | |
|---|---|
| VASP | Vienna Ab initio simulation package |
| TMD | Transition Metal Dichalcogenides |
| LO-TO | Longitudinal Optical - Transverse Optical |

# Chapter 1

# Introduction

*The ability to reduce everything to simple fundamental laws does not imply the ability to start from those laws and reconstruct the universe.*

P. W. Anderson, *More is different*[5]

A first-principles method, or ab initio method, is a bottom-up strategy to model a system. It does not require any knowledge of empirical rules or parameters other than the most fundamental physics laws[6]. In this dissertation, we aim to solve some previously unsolved problems in materials science, in a "constructionalist" manner[5]. Thanks to quantum mechanics, the electronic structure of solid states system can be solved in a first principles manner with certain degrees of approximations but no experimental parameters. Heisenberg is believed to be the first one to attempt solving multielectron problem using quantum mechanics and multi-body theory in early 1920s[7]. In 1960s, Kohn and Hohenberg proposed the concept of density functional theory(DFT)[8]. DFT has become the standard method for materials modeling nowadays due to its low computational cost and reproducibility[9]. Later in 1998, Walter Kohn was awarded the Nobel Prize in Chemistry for his contribution

to the DFT.

Lattice dynamics is the study of atomic vibrations in solid states crystalline systems. It is the key to understand many physical properties, including heat capacity, structural phase transitions, thermal expansion, ferroelectricity and even conventional superconductivity[10]. Plenty of experimental techniques have been developed to utilize the lattice dynamics for the study of interactions between atoms. For example, Raman and IR spectroscopies areboth powerful tools to directly measure the vibration frequency of atom displacements in crystals. The study of lattice dynamics has been a focus of solid states physics since almost a century ago and still plays an important role in today's materials science research[11].

Over the last 30 years, a unprecedented growth of computational power is taking place. The increasing computational power and development of advanced techniques have led to a surge of computational study on lattice dynamics in crystals[12]. It is shown that computational study of lattice dynamics can reveal the real physics behind some phenomenon: The lattice dynamics origin of ferroelectricity in $BaTiO_3$ was precisely modeled by Ronald Cohen in 1992 using only first-principles method[13]. Thermal conductivity in the insulators can also be predicted accurately through the calculation of phonon-phonon interactions[14]. The electron-phonon interactions are also intensively studied using density functional theory[15], which can even be used to calculate the critical temperature for certain conventional superconductors. Needless to say, DFT is such handy and precise that makes it a perfect tool to model the lattice dynamics.

That being said, there are plenty of problems in lattice dynamics that hasn't been properly addressed using DFT yet. In this thesis, I will introduce and explain some of our most recent first-principles studies on perovskite oxides, and transition metal dichalcogenides

about their multiple physical properties. These studies will be presented as three connected but self-contained chapters:

- **Lowering the polarization switching barriers of layered perovskite oxides.** I will introduce a systematic theoretical investigation over the crystal structures and ferroelectricity of Ruddlesden-Popper phase perovskites. Furthermore, a strain-engineering method is proposed to lower the polarization switching barrier.

- **Free-charge-carrier enhanced/induced ferroelectrics.** Free charge carriers were believed to be detrimental to ferroelectricity until recently. Our research on $Sr_3Sn_2O_7$ indicates the opposite phenomenon is possible, with a reasonable explanation.

- **The origin of anomalous effective charge in $HfS_2$.** The Born effective charge of Hf in $HfS_2$ is unexpectedly high when compared with other metals in dichalcogenides, leading to a strong LO-TO splitting in the Raman spectrum. We investigate the different nature of the bonding in this system using Wannier functions.

Before we discuss our own results, it is the best practice to introduce the theoretical background of our methods. In fact, the idea of density functional theory is a result of 'trade-off' between computational power and approximations, rather than a direct deduction of quantum mechanics. There are several significant advantages and limitations of DFT, which we will discuss in detail.

## 1.1 Many-body Schrödinger equation and relevant approximations

To model a material system at atomic scale, typically the materials is viewed as collections of electrons and nuclei:

$$\text{material} = \text{electrons} + \text{nuclei}$$

Theoretically, the wavefunction of electrons and nuclei $\psi(\mathbf{r})$ can be solved through the Schrödinger equation - a many-body Schrödinger equation[6], particularly:

$$\left[ -\sum_{i=1}^{i=N} \frac{\hbar^2}{2m_e}\nabla_i^2 - \sum_{1}^{I=M} \frac{\hbar^2}{2M_I}\nabla_I^2 + \frac{1}{2}\sum_{i\neq j} \frac{e^2}{4\pi\epsilon_0}\frac{1}{|\mathbf{r_i}-\mathbf{r_j}|} + \frac{1}{2}\sum_{I\neq J} \frac{e^2}{4\pi\epsilon_0}\frac{Z_I Z_J}{|\mathbf{R_I}-\mathbf{R_J}|} - \sum_{i,I} \frac{e^2}{4\pi\epsilon_0}\frac{Z_I}{|\mathbf{r_i}-\mathbf{R_I}|} \right] \psi = E_{tot}\psi \qquad (1.1)$$

Index i represents the electrons in the system and index j stands for the nuclei. $m_e$ and $M_i$ are mass of electron and nucleus j. $e$ is the charge of one electron, which is $1.602 \times 10^{-19} C$ and $\hbar$ is the reduced Planck's Constant. There are five energy terms in this Schrödinger equation. From left to right, the first two are the kinetic energy of electrons and nuclei respectively. The rest three are from the Coulomb interactions of electron-electron, nucleus-nucleus and electron-nucleus terms, respectively. The solution wavefunction $\psi$ is a function of electrons' and nuclei's position:

$$\psi = \psi(r_1, r_2, \ldots, r_N, R_1, R_2, \ldots, R_M) \qquad (1.2)$$

For any real-world material, the number of electrons and nuclei is at the magnitude of $10^{23}$. Even with periodic conditions, the amount of calculations is still beyond the modern computational capacity. Though the number of atoms and electrons can be greatly reduced, the problem's exponentially scaling nature makes any precise solution impossible, even with the state-of-art computational power. As a result, appropriate approximations are necessary for the technically feasible first-principles study and has been studied extensively.

Among those approximations, one of them is simple yet powerful: the Born-Oppenheimer approximation. It states that the wavefunction of a material system can be written as a product of electrons and nuclei wavefunction, because the nuclei are much heavier than electrons. In fact, the nuclei are heavy enough that they can be treated as immobile when solving the ground state of electron wavefunction, which simplifies the equation (1.1) into:

$$\left[ -\sum_{i=1}^{i=N} \frac{\hbar^2}{2m_e} \nabla_i^2 + \frac{1}{2} \sum_{i \neq j} \frac{e^2}{4\pi\epsilon_0} \frac{1}{|\mathbf{r_i} - \mathbf{r_j}|} - \sum_{i,I} \frac{e^2}{4\pi\epsilon_0} \frac{Z_I}{|\mathbf{r_i} - \mathbf{R_I}|} \right] \psi_e = E_e \psi_e \tag{1.3}$$

The new wavefunction $\psi_e$ here only depends on the position of electrons and the nuclei are assumed to be static. This approximation is called clamped-nuclei approximation[16]. It reduces the complexity of the original multi-body Schrödinger equation significantly.

Nevertheless, the new equation remains practically unsolvable because there are too many electrons. One possible way to further simplify equation (1.3) is by introducing mean-field theory and unentangled electrons approximation, which leads to the Hartree-Fock method[17,18]:

$$\left[-\frac{\hbar^2}{2m_e}\nabla^2 + V_n(\mathbf{r}) + V_H(\mathbf{r})\right]\phi_i(\mathbf{r}) + \int d\mathbf{r}' V_x(\mathbf{r},\mathbf{r}')\phi_i(\mathbf{r}') = \varepsilon_i\phi_i(\mathbf{r}) \tag{1.4}$$

$$V_n(\mathbf{r}) = -\sum_{i,I}\frac{e^2}{4\pi\epsilon_0}\frac{Z_I}{|\mathbf{r}-\mathbf{R_I}|} \tag{1.5}$$

$$V_H(\mathbf{r}) = \frac{e^2}{4\pi\epsilon_0}\int d\mathbf{r}'\frac{n(\mathbf{r}')}{|\mathbf{r}-\mathbf{r}'|} \tag{1.6}$$

$$n(\mathbf{r}) = \sum_i |\phi_i(\mathbf{r})|^2 \tag{1.7}$$

$$V_x(\mathbf{r},\mathbf{r}') = -\sum_j \frac{\phi_j^*(\mathbf{r}')\phi_j(\mathbf{r})}{|\mathbf{r}-\mathbf{r}'|} \tag{1.8}$$

The equation 1.4 is called Hartree-Fock equation and it has four energy terms: kinetics energy, electron-nucleus Coulomb interaction $V_n(\mathbf{r})$, Hartree interaction$V_H(\mathbf{r})$ and a non-local interaction$V_x(\mathbf{r},\mathbf{r}')$. Note that $\phi_i(\mathbf{r})$ here is a set of orthonormal single electron wavefunction. Since electron is a fermion, the total electron wavefunction $\psi_e$ can be constructed from these single electron wavefunctions by a matrix determinant called Slater determinant[19].

The first three energy terms describe a collection of non-interacting electrons, with the Coulomb potential being considered as a mean field. The solution is rather straightforward if there are only three local interaction terms, but the existence of a non-local term $V_x$ prevents a direct solution of equation. This exception $V_x$ term is called as Fock exchange potential, which is to prevent two electrons from occupying the same states[6]. With that being said, the biggest advantage of Hartree-Fock method is the reduction of a single unsolvable N-variables equation into N coupled equations, which can be solved in a self-consistent manner: The initial value could be a set of basis function and then minimize the total energy using variational principles[20].

This algorithm was actually implemented even more than half a century ago: Perkins calculated a two electron system (the ground state energy of the He atom) in 1958 and the result is very close to the experimental values[21]. And it is still a very commonly used and developing method that can be found in multiple commercial and open source first-principles software packages. This being said, apparently the very important electron-electron Coulomb interaction is not taken into account precisely in this method through the very simple mean-field approximation. Thus Kohn and Sham proposed a elegant solution to this problem by a similar yet different equation[22]:

$$\left[-\frac{\hbar^2}{2m_e}\nabla^2 + V_n(\mathbf{r}) + V_H(\mathbf{r}) + V_x(\mathbf{r}) + V_c(\mathbf{r})\right]\phi_i(\mathbf{r}) = \varepsilon_i\phi_i(\mathbf{r}) \tag{1.9}$$

These two new terms $V_x(\mathbf{r})$ and $V_c(\mathbf{r})$ are approximations for exchange and correlation functions, which are often written as one function $V_{xc}$. This equation is commonly known as the Kohn-Sham equation. The approximation seems over-simplified but it is in principle exact (if the exchange-correlation term $V_{xc}$ is known - it isn't unfortunately). It greatly simplifies the calculations while achieving good agreement with experiments, which will be discussed in the next section.

## 1.2 Density functional theory

In the previous sections, we have seen that the quantum states of a system with N electrons involves 3N Cartensian coordinates. Though the single electron approximation reduces the total wavefunction $\psi$ into the product of individual electrons wavefunctions $\phi_i$, the system is still complex for practical solutions. Density functional theory, or DFT, provides

a framework to describe the system with density function, of which only three degrees of freedom are present.

The whole idea of DFT stems from a rather simple statement, the Hohenberg-Kohn theorem[23]. It states that: "the energy of the ground state is a functional of the electron density only"[6], which means:

$$E = F[n(\mathbf{r})] \tag{1.10}$$

$n(\mathbf{r})$ is the electron density, which only consists of three variables $x, y, z$ only. The proof of this theorem is based on the three facts that:

- The electron density determines uniquely the nuclei-electrons interaction.
- The nuclei-electron interaction determines uniquely the electron wavefunction.
- The electron wavefunction determines uniquely the total energy.

Proof of these three statements are rather intuitive[23] but the conclusion is important - In principle, the ground state energy can be calculated precisely through the equation 1.9 if the exchange-correlation function is accurate:

$$\begin{aligned} E &= \langle \psi[n] | \left[ -\frac{\hbar^2}{2m_e}\nabla^2 + \hat{V}_n + \hat{V}_H + \hat{V}_{xc} \right] | \psi[n] \rangle \\ &= -\sum_i \int d\mathbf{r} \frac{\hbar^2}{2m_e} \phi_i^*(\mathbf{r}) \nabla^2 \phi_i(\mathbf{r}) + \int d\mathbf{r} n(\mathbf{r}) \left[ V_n(\mathbf{r}) + V_H(\mathbf{r}) + V_{xc}(\mathbf{r}) \right] \\ &= \sum_i \varepsilon_i \end{aligned} \tag{1.11}$$

Here the $\phi_i(\mathbf{r})$ are Kohn-Sham wavefunctions which are set of orthornormal basis functions. The external potential $V_n(\mathbf{r})$ is a function that is solely determined by the nuclei positions.

The Hartree energy term $V_H(\mathbf{r})$ can be calculated using the electron density:

$$\nabla^2 V_H(\mathbf{r}) = \frac{n(\mathbf{r})}{\epsilon_0} \tag{1.12}$$

And the last term $V_{xc}(\mathbf{r})$ is also determined by the electron density:

$$V_{xc}(\mathbf{r}) = \frac{\delta E_{xc}}{\delta n(\mathbf{r})} \tag{1.13}$$

Unfortunately, in reality the exact form of exchange-correlation function is unknown. While numerous efforts have been made to develop approximate exchange-correlation functionals, there isn't a single approximation that works well for every scenario[24]. Nevertheless, most of the approximations we are using in our work has been tested thoroughly and works very well for our applications. In the simplest case, the exchange-correlation energy at $\mathbf{r}$ can be treated as that of a homogeneous electron gas with the equal amount of local electron density $n(\mathbf{r})$. That value can be calculated numerically using Monte Carlo method with good precision[25]. This approximation is called Local Density Approximation(LDA), and it is the fundamental for all other approximations. LDA works well when the long-range part of $V_{xc}$ is not a dominant effect[26]. For example the volume of many crystal unit cell can be predicted very well using LDA: Haas et al showed that[27], the relative errors between LDA-calculated and experimental values are less than 0.5% for the majority of solids they tested. There are also approximations that take into account of the derivative of electron density, which is called generalized gradient approximations(GGAs). However, they are still approximations that work well for most cases but might fail especially when the electron-electron interactions become important[28].

With all the term specified, the ground state energy and electron density can be solved in an iterative self-consistent way:

1. Make initial guess of the electron density $n(\mathbf{r})$.

2. Calculate the external potential $V_n$, the Hartree potential $V_H$ and exchange-correlation potential $V_{xc}$ using the electron density from step 1.

3. Calculate discretized Kohn-Sham wavefunctions $\phi_i(\mathbf{r})$ (in either real space or plane wave form) by diagnolizing the discretized Kohn-Sham equation.

4. Calculate the new electron density using $n(\mathbf{r}) = \sum_i \phi_i(\mathbf{r})^2$.

5. If the new electron density is different from the old one, start again from step 2 and calculate the new potential energy. Otherwise the new electron density can be used as the final output.

That being said, this is purely an illustration of our method and not the most commonly used scheme, although this real space method is becoming more and more popular for some specific applications like point defects[29] and other disordered systems. In practice, the calculation is usually performed in the reciprocal space under the Bloch-wave scheme[30], with the Bloch function represented by plane waves. It could take advantage of the translational symmetry in crystal and represent the whole system using a unit cell of few electrons and small numbers of discretized k-points.

In our study, we use Projected Augmented Wave (PAW) method which provides a computationally convenient way with high accuracy[31]. There is a problem by using plane wave basis: near the nuclei, the electron wavefunction can be very confined and requires

large numbers of plane wave functions to describe accurately, which is a waste of computational resources. PAW allows us to take advantage of both reciprocal space and real space: near the nuclei, the wavefunctions are expanded using atomic orbitals; whereas outside the augmentation region, plane wave are used. At the boundary, the derivative and value of wavefunction is equal from either side to ensure the result is smooth.

## 1.3 Lattice dynamics

In the study of lattice dynamics, atomic motions are can be expanded by using harmonic traveling waves (phonons). Each individual harmonic traveling wave is always associated with a wavevector $\mathbf{k}$ and an angular frequency $\omega$. The wavevector $\mathbf{k}$ determines the traveling direction and wavelength:$\lambda = \frac{2\pi}{|\mathbf{k}|}$, and the frequency is a function of wavevector. In any periodic system, there is a limitation of wavevector because the wavelength cannot be smaller than the periodicity of lattice. For example, in 1-D atomic chain, the wavevector can only vary from $-\frac{\pi}{a}$ to $\frac{\pi}{a}$ ($a$ is the lattice parameter).

Lattice dynamics is a powerful tool for the study of structural phase transitions, where some symmetry elements are broken through a collective motion of atoms in the original high symmetry structures. This collective motion is often a 'soft' phonon, which has a very low frequency. For second-order structural phase transition, the soft phonon mode even has a imaginary frequency. By calculating the frequencies of phonons and combining this information with group theory arguments, one can predict the possible structural phase transitions of any crystal structure. In chapter 2 and chapter 3, a systematic study on the possible crystal structures of layered perovskites is conducted using this method.

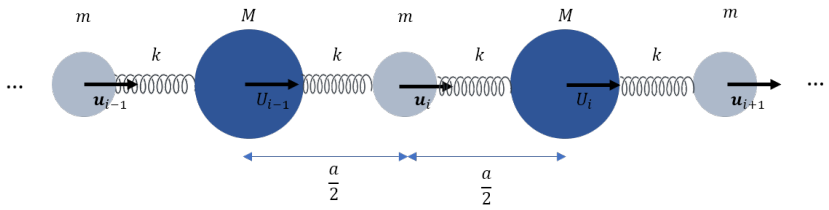


Figure 1.1: The diatomic chain model is an 1-D periodic system, with 2 atoms in each unit cell. Each atom is separated by $\frac{a}{2}$ in equilibrium. The displacement of the smaller atom in unit cell $i$ from its equilibrium position is noted as $u_i$, and the displacement of the larger one is noted as $U_i$.

### 1.3.1 Diatomic chain model

The diatomic chain is a simple yet effective 1-D model to demonstrate the basic concepts in lattice dynamics. There are two kinds of atoms in this diatomic chain: atoms of mass $M$ and atoms of mass $m$. Atoms are 'connected' by springs with spring constant of $k$. In the equilibrium state, atoms are evenly spaced with intervals of $\frac{a}{2}$. The displacements of the $i$th smaller atom and larger atom are noted as $u_i$ and $U_i$ respectively. The classical equations of motion for these two types of atoms can be written as:

$$\begin{aligned} m\frac{d^2u_i}{dt^2} &= -k(2u_i - U_{i-1} - U_i) \\ M\frac{d^2U_i}{dt^2} &= -k(2U_i - u_i - u_{i+1}) \end{aligned} \tag{1.14}$$

Here is a solution that could take advantage of the periodicity in both time and space[10]:

$$\begin{aligned} u_i(t) &= u_0 e^{i(qna-\omega t)} \\ U_i(t) &= U_0 e^{i(qna+qa/2-\omega t)} \end{aligned} \tag{1.15}$$

where $q$ is the wavevector and $\omega$ is the frequency. Notice that, the solution remains unchanged by adding any integer multiples of $\frac{2\pi}{a}$ to the wavevector $q$. As a result, $q$ should be confined within the interval of $[-\frac{\pi}{a}, \frac{\pi}{a})$, which is defined as first Brillouin zone[30]. Substitute this solution back into the dynamic equation, we will have:

$$\begin{aligned} -m\omega^2 u_0 &= -k(2u_0 - U_0 e^{-iqa/2} - U_0 e^{iqa/2}) \\ -M\omega^2 U_0 &= -k(2U_0 - u_0 e^{-iqa/2} - u_0 e^{iqa/2}) \end{aligned} \tag{1.16}$$

By canceling out the $u_0$ and $U_0$ in both equations, the frequency $\omega$ can be written as a function of wavevector $q$:

$$\omega^2 = k(\frac{1}{m} + \frac{1}{M}) \pm k\sqrt{(\frac{1}{m} + \frac{1}{M})^2 - \frac{4\sin^2(qa/2)}{mM}} \tag{1.17}$$

And we can also solve the original equations and get the relation between $u_0$ and $U_0$:

$$\frac{u_0}{U_0} = \frac{2k\cos(qa/2)}{2k - m\omega^2} \tag{1.18}$$

The dispersion relation in equation (1.17) corresponds to two separate phonon branches, as shown in figure (1.2). The lower branch is called the acoustic branch while the higher one is called the optical branch. The physical meaning behind the names is related to their atomic displacement patterns. In the long wavelength limit, where $qa \ll 1$, the dispersion

relation can be approximated as:

$$\omega^2_{acoustic} \approx \frac{2k}{m+M}\frac{a^2q^2}{4}$$
$$\omega^2_{optical} \approx \frac{2k(m+M)}{mM} \tag{1.19}$$

Substituting them back into the equation (1.18):

$$u_0 = U_0 \quad \text{in acoustic branch}$$
$$u_0 = -\frac{M}{m}U_0 \quad \text{in optical branch} \tag{1.20}$$

In the long wavelength limit, any two adjacent atoms will move in the opposite directions in the optical branch and in the same direction for the acoustic branch. If the atoms carry charges, the optical mode will induce a dynamic dipole which could interact with the electromagnetic fields. This phonon-EM wave coupling can even lead to a frequency shift and cause LO-TO splitting which we will discuss in detail in chapter 4.

In the diatomic model only the nearest neighbor harmonic interaction is taken into account here, which gives rise to the simple 2-branches dispersion curve. In real-world three-dimensional materials, the dimensional effects have to be taken into considerations, along with the long-range interactions. There are usually more than 2 atoms per unit cells, which further increases the number of phonon branches. In reality, the 'spring constant' is rather complicated and takes the form of a matrix, known as 'force constant matrix', which is defined by the second-order derivative of total energy about structural equilibrium

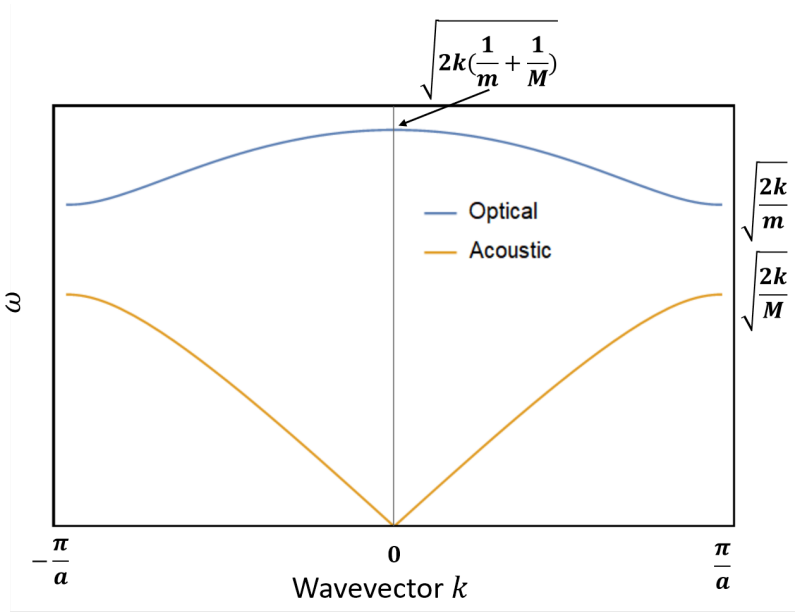


Figure 1.2: The phonon dispersion relation of diatomic chain model. There are two branches: the lower one is acoustic branch and the higher one is optical branch. $k$ is the spring constant and $m, M$ are the masses of smaller and larger atoms respectively.

coordinates:

$$D^{\nu,\nu'}_{n\alpha,n'\alpha'} = \frac{\partial^2 E}{\partial \mathbf{u}_{\mathbf{n}\nu,\alpha} \partial \mathbf{u}_{\mathbf{n}'\nu',\alpha'}} \tag{1.21}$$

where $n$ and $n'$ are indices for the $n$-th and $n'$-th unit cells, $\nu$ and $\nu'$ are the $\nu$-th and $\nu'$-th atoms in a unit cell, $\alpha$ and $\alpha'$ are indices for the Cartesian coordinates. The displacement of $\nu$-th atom in unit cell $n$ from its equilibrium position is labeld as $\mathbf{u}_{n\nu}$. Since a crystal has long-range translational symmetry, the force constant matrix can also take the form as a function of wavevectors $D(\mathbf{q})$.

The precise calculation of the force constant matrix is typically the first yet the most computationally demanding step for any further study of lattice dynamics. It can be done in two ways through density functional theory: frozen phonon and dynamical functional perturbation theory(DFPT).

### 1.3.2 Frozen phonon method

Under the harmonic approximation, the classical equation used in the diatomic model can be generalized to develop a general method for any three dimension crystals. The energy of any electronic-nuclear system can be expanded to second order about the atomic displacement:

$$E(\{\mathbf{u}_{n\nu}\}) = E_0(\mathbf{0}) + \frac{1}{2} \sum_{n\nu\alpha, n'\nu'\alpha'} D_{n\nu\alpha, n'\nu'\alpha'} u_{n\nu\alpha} u_{n'\nu'\alpha'} \tag{1.22}$$

There is no linear term present in the energy expansion because the crystal structure in equilibrium state is fully relaxed, meaning forces on atoms are zero. There is also a hidden adiabatic approximation here: the electrons move much faster than the nuclei and they are always in the ground state.

Similar to what we have in the diatomic model, the dynamical equation is:

$$M_\nu \ddot{u}_{n\nu\alpha} = - \sum_{n'\nu'\alpha'} D_{n\nu\alpha, n'\nu'\alpha'} u_{n\nu\alpha} u_{n'\nu'\alpha'} \tag{1.23}$$

Here the $M_\nu$ is the mass of $\nu$-th atom. A solution that has translation symmetry in both time and space is desired here as well, due to the periodic nature of crystals:

$$\mathbf{u}_{n\nu} = \mathbf{u}^0_\nu(\mathbf{q}, \omega) e^{i(\mathbf{q}\cdot\mathbf{r_n} - \omega t)} \tag{1.24}$$

The $\mathbf{u}^0_\nu$ is the amplitude of atomic displacement, and $\mathbf{q}$ is the wavevector. $r_n$ is the trans-

lation vectors of the $n$-th unit cell. Substitute it back into equation (1.23), it becomes:

$$M_\nu \omega^2 \mathbf{u}_\nu^0 = -\sum_{n'\nu'\alpha'} D_{n\nu\alpha,n'\nu'\alpha'} e^{-i\mathbf{q}\cdot\mathbf{r}_{nn'}} \mathbf{u}_\nu^0 \tag{1.25}$$

where $\mathbf{r}_{nn'}$ is the translation vector between the $n$-th and $n'$-th unit cell. Equation in this form is known as secular equation, of which the non-trivial solutions can be obtained by a determinant equation:

$$|D_{n\nu\alpha,n'\nu'\alpha'}(\mathbf{q}) - M_\nu \omega^2 \delta_{\alpha\alpha'} \delta_{\nu\nu'}| = 0 \tag{1.26}$$

where the force constant matrix $D_{n\nu\alpha,n'\nu'\alpha'}$ is Fourier-transformed into the reciprocal space for convenience:

$$D_{n\nu\alpha,n'\nu'\alpha'}(\mathbf{q}) = \sum_{n'} D_{n\nu\alpha,n'\nu'\alpha'} e^{-i\mathbf{q}\cdot\mathbf{r}_{\mathbf{nn'}}} \tag{1.27}$$

By solving equation 1.26, the frequency and displacement pattern of the phonons can be calculated. The force constant matrix cannot be directly measured experimentally. But thanks to the Hellmann–Feynman theorem, density functional theory can be a powerful tool for calculating the force constant matrix without any prior knowledge of the system. Hellmann–Feynman theorem states that, any first order derivative $\partial E/\partial\lambda$ only depends on the ground state density. For example, force is first-order derivative of energy with respect to spatial coordinates[6]:

$$\mathbf{F}_{n\nu} = \frac{\partial E}{\partial \mathbf{u}_{n\nu}} = \int n(\mathbf{r}) \frac{\partial V}{\partial \mathbf{u}_{n\nu}} d\mathbf{r} \tag{1.28}$$

where the $V$ is the total coulomb potential and $\mathbf{F}_{n\nu}$ is the force on atom $\nu$ in the $n$-th unit cell.

The idea of frozen phonon method is to explicitly displace each individual atom by

a small amount and then calculate the retraction forces on all atoms. The second-order derivatives, elements of force constant matrix, can be found via:

$$D_{n\nu\alpha,n'\nu'\alpha'} = -\frac{\partial F_{n'\nu'\alpha'}}{\partial \mathbf{u}_{n\nu}} \tag{1.29}$$

In practice, this perturbation $\mathbf{u}_{n\nu}(\mathbf{q})$ is often applied in the form of a monochromatic wave:

$$\mathbf{u}_{n\nu}(\mathbf{q}) = \tau e^{-i\mathbf{q}\cdot\mathbf{r_n}} \tag{1.30}$$

where $\tau$ is a small displacement vector. To calculate the force constant matrix at $\mathbf{q}$, only the perturbation with the wavevector $\mathbf{q}$ is needed.

In the frozen phonon method, the phonon can only be calculated at some $\mathbf{q}$ points, because the wavevector determines size of the supercell for the DFT calculation. As we can see from equation 1.30, the wavelength can be very long at small $\mathbf{q}$ and results in a very large system for calculation. Take a cubic unit cell as an example: the same atom in all unit cells will be displaced by the same amount when $\mathbf{q} = (0, 0, 0)$, according to equation 1.30. There is no need to increase the size of the original unit cell in order to accommodate this perturbation. However, for phonons at $(\frac{\pi}{a}, \frac{\pi}{a}, \frac{\pi}{a})$, there is no way for one unit cell to accommodate this displacement - because the same atom in any two adjacent unit cells will be displaced in the opposite direction. Thus the unit cell has to be doubled in all three directions, which is 8 times larger than the original system. This newly constructed unit cell is referred to as 'supercell'.

Though frozen-phonon method is good at accuracy and easy to be implemented, there is no practical way to sample a large number of wavevectors in the first Brillouin zone using

it. The supercell size can be unacceptably large especially in the long wavelength limit. This is the major disadvantage of frozen phonon method and the reason why we are looking for a better-scaling algorithm in the next section.

### 1.3.3 Density functional perturbation theory

Unlike the frozen phonon method, density functional perturbation theory (DFPT) offers a way to calculate the force constant matrix at any arbitrary **q** point without worrying about supercells. DFPT can also be used for other perturbations like electric field, just like the frozen phonon method.

The basic idea behind using DFPT is to calculate the second-order derivative without actually displacing the atoms[32]:

$$D_{n\nu\alpha,n'\nu'\alpha'} = \frac{\partial^2 E}{\partial u_{n\nu\alpha} u_{n'\nu'\alpha'}} = \int \frac{\partial V(\mathbf{r})}{\partial u_{n\nu\alpha}} \frac{\partial n(\mathbf{r})}{\partial u_{n'\nu'\alpha'}} d\mathbf{r} + \int n(\mathbf{r}) \frac{\partial^2 V(\mathbf{r})}{\partial u_{n\nu\alpha} \partial u_{n'\nu'\alpha'}} d\mathbf{r} \qquad (1.31)$$

Where the $V(\mathbf{r})$ is the total Coulomb potential, which includes all electron-nucleus and nucleus-nucleus interaction, Hartree potential and exchange-correlation energy. In principle, any $(2n+1)$ derivative of energy can be determined by the $n$-th order derivative of the charge density $n(\mathbf{r})$. This theorem, known as $(2n+1)$ theorem, allows the capability of calculating the force constant matrix at any wavevectors without constructing supercells. In practice, the perturbation $\frac{\partial n(\mathbf{r})}{\partial \lambda}$ has to be determined in a self-consistent way: the second-order derivative of energy will be minimized as a function of the perturbation $\frac{\partial n(\mathbf{r})}{\partial \lambda}$. The method is also readily extendable to the projector-augmented wave (PAW) framework[33].

# Chapter 2

# Suppressing the ferroelectric switching barrier in hybrid improper ferroelectrics

This chapter is adapted from my work *Suppressing the ferroelectric switching barrier in hybrid improper ferroelectrics*[34].

Ferroelectricity is a property of certain materials which have spontaneous electric polarization, that can be reversed by applying an external field. Density functional theory and lattice dynamics have long been used for the investigation of origin of ferroelectricity[13]. In this chapter, we will discuss a special type of ferroelectricity - hybrid improper ferroelectricity, and a potential way to control its switching energy barrier. Integration of ferroelectric materials into novel technological applications requires low coercive field materials, and consequently, design strategies to reduce the ferroelectric switching barriers. We will show

that biaxial strain, which has a strong effect on the ferroelectric ground states, can be used to tune the switching barrier of hybrid improper ferroelectric Ruddlesden-Popper oxides. We identify the region of the strain – tolerance factor phase diagram where this intrinsic barrier is suppressed, and show that it can be explained in relation to strain induced phase transitions to nonpolar phases.

## 2.1 Background

Since the discovery of ferroelectricity in $BaTiO_3$ [35], perovskite oxides have been heavily studied and utilized in applications as ferroelectric materials. Versatility of the perovskite structure allows a large number of complex oxides to be synthesized, but among those, only a small fraction are ferroelectrics [36]. A major breakthrough in perovskite-related ferroelectrics is the discovery of hybrid improper ferroelectricity (HIF) as a materials design route in 2011, which led to an explosion in the predictions of novel ferroelectric oxides [37]. Among those, the list of examples that are experimentally verified includes $A_3B_2O_7$ HIFs $(Ca,Sr)_3Ti_2O_7$ [38], $(Sr,Ca)_3Sn_2O_7$, $Sr_3Zr_2O_7$ [39–41], as well as a weak ferromagnetic $(Ca_{0.69}Sr_{0.46}Tb_{1.85}Fe_2O_7)$ [42].

Despite the prediction of ferroelectricity and observation of a polar crystal structure in many compounds, experimentally observing the switching of polarization is challenging. For example, the original HIF $Ca_3Ti_2O_7$ was reported to have a polar structure 20 years before the idea of HIFs was introduced [43], but the direct evidence of polarization switching was not observed until 2015 [38]. The reason behind the absence of switching in these materials was initially believed to be large intrinsic coercive fields, or defects in the

materials, which typically increase the coercive field[44,45]. The high experimental coercive field is not surprising, because the energy scale that needs to be overcome for switching is considered to be determined by the octahedral rotations, which often have an energy scale significantly higher than that of the ferroelectric distortions in typical perovskite oxides. Switching was observed in other HIF materials with coercive fields ranging from 120 to 200 $kV{\cdot}cm^{-1}$ [38,39,41], and very recently, the smallest coercive field of 39 $kV{\cdot}cm^{-1}$ was observed in single crystals of $Sr_3Sn_2O_7$ [46]. Though these coercive fields are comparable to values suitable for integration to silicon chips ($E_c \approx 50$ $kV{\cdot}cm^{-1}$), applications such as high-power actuators and low-voltage logic and memory elements ask for ferroelectrics with robust polarizations that can be switched by a lower coercive field[47–50]. Ultra-low coercive fields as low as 5 $kV{\cdot}cm^{-1}$ were observed in pulsed laser deposition grown $Ca_3Ti_2O_7$ thin films, but the reason behind this reduction (and whether it is an intrinsic or an extrinsic effect) is not clarified yet[51].

Understanding the intrinsic mechanisms that affect the coercive field of HIF materials, and finding new design strategies to reduce these fields are important for their applications. In the following subsections, we will illustrate that strain can be an effective means to achieve this. Epitaxial strain, obtained by growing thin films on lattice mismatched substrates, has been used extensively as a way to tune the ferroelectric and dielectric properties of perovskites[52,53]. Both the octahedral rotations, and the proper ferroelectric order parameter are strongly coupled with the biaxial strain in most materials, and strain is shown to change the switching energy barrier of ferroelectrics as well.[54] HIFs are shown to undergo interesting structural phase transitions under strain as well[55], but there is no detailed study of the switching behavior of HIFs under biaxial strain. The original study

on HIFs[37] showed that the lowest energy switching path and energy (which is correlated with the coercive field) is strain dependent, but the recent work that illustrate the richness of possible switching paths makes it necessary to re-evaluate the polarization switching behavior of strained HIFs[56,57].

In this chapter, we present density functional theory (DFT) calculations on 13 different $A_3B_2O_7$ Ruddlesden-Popper compounds to map out the strain-tolerance factor phase diagram, and show that the strain induced non-polar or anti-polar phases emerge in compounds with a finite range of tolerance factors. We then show, by performing nudged elastic band (NEB) calculations, that the intrinsic coherent polarization switching energy barrier decreases as the compounds get closer to phase boundaries by biaxial strain. This suppression of switching barrier is not always accompanied with a decrease in the polarization, which makes strain tuning of HIF Ruddlesden-Poppers a viable tool to obtain low coercive field ferroelectrics with a robust polarization. We also show that the tensile and compressive strains favor different switching pathways, which can be intuitively understood in terms of which octahedral rotations or tilts are favored by strain.

This chapter is organized as follows: We start by explaining the crystal structures and important normal modes. We then present and discuss the strain - tolerance factor phase diagram of HIF RP's. Then, we present the trends of the intrinsic switching barrier as a function of strain.

## 2.2 Methods

Density functional theory calculations are performed using the projector augmented wave approach[31] as implemented in the Vienna Ab-initio Simulation Package (VASP)[58,59], and using the PBEsol generalized gradient approximation[60]. All calculations are done in a 48-atom (4 formula unit) supercell, which can be viewed as a $\sqrt{2} \times \sqrt{2} \times 2$ multiple of the primitive cell of the reference $I4/mmm$ structure. A $\Gamma$-centered $6 \times 6 \times 2$ grid of k-points is used for the Brillouin zone integrals.

We consider all $A_3B_2O_7$ compounds with A = Ca, Sr, Ba and B = Ti, Zr, Sn, Ge, as well as $Cd_3Ti_2O_7$[2,39–41,61–64]. These compounds are all band insulators with sizable gaps, so using the PBEsol generalized gradient approximation is expected to reproduce the crystal structures with reasonable accuracy. Biaxial strain boundary conditions are simulated by fixing the in-plane lattice constants, and allowing the out of plane component, as well as internal atomic positions, to relax with an force threshold of 2 $meV/$Å. The zero strain is defined for each compound by the $a$ lattice constant obtained by completely relaxing the structure in the reference high symmetry structure $I4/mmm$.

The Goldschmidt tolerance factor[65], which is used as a simple measure to predict tendency towards octahedral rotations, and is originally defined in terms of the ionic radii $r$ using

$$\tau = \frac{r_A + r_O}{\sqrt{2}\,(r_B + r_O)} \tag{2.1}$$

is instead calculated using the bond lengths for 12 coordinated A-site ($d_{AO}$) and 6 coordi-

nated B-site ($d_{BO}$) ions from the bond valence model as

$$\tau = \frac{d_{AO}}{\sqrt{2} \cdot d_{BO}}. \tag{2.2}$$

(This approach is following Ref.[66].)

In order to calculate the minimum energy barrier for polarization switching, climbing-image nudged elastic band (CI-NEB) method was used to further relax linearly interpolated switching paths to the minimum energy path[67]. The spring constant was set to 5 eV/Å$^2$, and a convergence criterion of 1 meV per supercell was used. Distortion symmetry groups[68,69] are used to enumerate and name the possible initial pathways following Ref.[57] with the help of the DiSPy package[70]. All the switching pathways reported in the text retain their symmetry for all values of the reaction coordinate under NEB calculation.

As various points in this paper, symmetry and group theory related arguments are built using the Isotropy Software Package[71] and the Bilbao Crystallographic Server[72–74]. VESTA software was used for visualization of crystal structures.[75]

## 2.3 Crystal structures of RP-phase perovskites

The $A_3B_2O_7$ compounds considered in this chapter are the $n = 2$ members of the Ruddlesden-Popper series[76,77]. They can be considered as layered perovskites with an extra AO layer inserted after every 2 perovskite bi-layers (i.e. 4 atomic layers) along the [001] direction (Figure 2.1a). The extra AO layers cause a shift by ($a/2$, $a/2$, 0) on the $ab$ plane, and hence the structure becomes body centered tetragonal with space group $I4/mmm$ (#139). This shift also breaks the connectivity of the oxygen octahedra, and the AO double layer is held

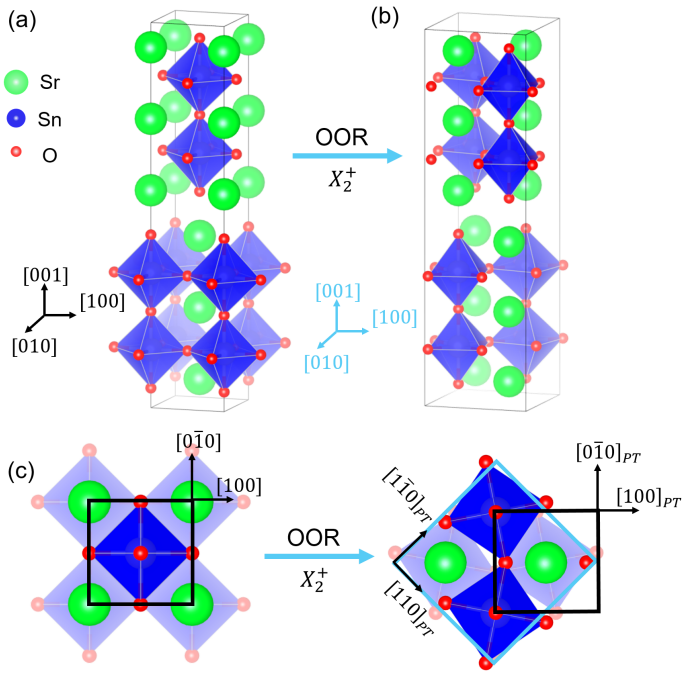


Figure 2.1: **The $n = 2$ Ruddlesden-Popper Structure** (a) The high symmetry body-centered-tetragonal phase ($I4/mmm$) of $A_3B_2O_7$ RP-phase perovskites. (b) Compounds with tolerance factor less than one develop octahedral rotation/tilt distortions, which are usually associated with normal modes at the X point of the Brillouin zone. (The figure shows the $X_2^+$ mode.) These distortions double the original unit cell and symmetry becomes orthorhombic. (c) Orientations of the crystal axes in the orthorhombic cell are different from those in the high symmetry tetragonal cell. Throughout this paper, we use the axes of a pseudo-tetragonal cell (shown in black) that can be defined within the orthorhombic cell (shown in light blue).

together by mostly ionic bonds between the A-site cations and O anions. The resulting dimensional reduction has important consequences on the electronic structure and lattice response (For example, Ref.'s[1,78–80]). Apart from the dimensional effects, the different periodicity of the Ruddlesden-Popper phases along the layering direction ($c$ axis, or the [001] direction) leads to a smaller Brillouin zone than $ABO_3$ perovskites. The equivalents of various structural instabilities that are at different points of the Brillouin zone in the $ABO_3$ perovskites can fold back onto the same point in $A_3B_2O_7$ Ruddlesden-Poppers, which leads

to interesting couplings between them as discussed below. (This point can be qualitatively understood in analogy to a subduction problem, where a zone boundary mode of the parent group corresponds to a zone center mode of the subgroup. For example, when the unitcell of a cubic perovskite is doubled along the [001] axis as a result of cation order, the spacegroup becomes $P4/mmm$ and the zone boundary $X_5^-$ mode splits into $\Gamma_5^- \oplus X_2^- \oplus X_3^-$, where $\Gamma_5^-$ is polar. While there is no direct group-subgroup relationship between the Ruddlesden-Popper and perovskite structures, the $n = 2$ Ruddlesden-Poppers have 2 perovskite blocks in their unitcells, and it is thus possible to recognize some phonon modes folded onto the $k_z = 0$ plane.)

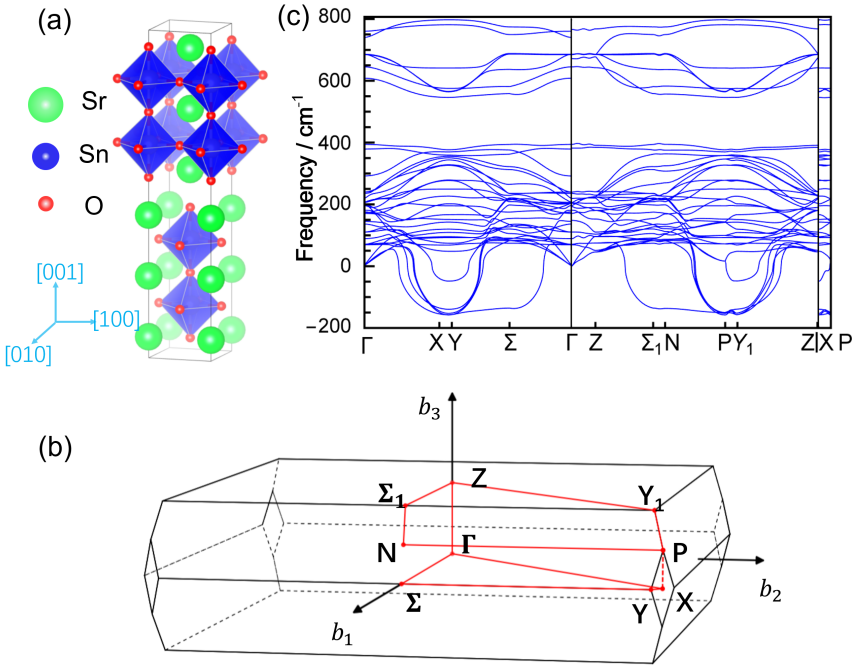


Figure 2.2: **Phonon Spectrum of $Sr_3Sn_2O_7$:** (a) The conventional unit cell of $Sr_3Sn_2O_7$ in high-symmetry $I4/mmm$ structure. (b) The first Brillouin zone of this structure. (c) The phonon spectrum of this structure. The instabilities are strongest at the $X$ point, but the unstable branch remains unstable for a sizable volume that covers other high symmetry k-points around the $X$ point.

By far the most common structural distortions that decrease the symmetry of oxide perovskites is the oxygen octahedral rotations: About 90% of all oxide perovskites have this type of distortion in their crystal structures, which reduces the symmetry of the parent $Pm\bar{3}m$ phase[66]. These distortions can be described in terms of symmetry-adapted-modes, which can be classified by irreducible representations (irreps) of the parent spacegroup $Pm\bar{3}m$[81]. The phonon modes that correspond to these distortions are the M point mode $M_2^+$, which is an in-phase rotation of octahedra around one axis, and the R point mode $R_5^-$, which is an out-of-phase rotation of octahedra around one axis. The former is denoted by a '+' superscript in the Glazer notation, such as $a^0a^0c^+$, and the latter is denoted by a '−' superscript, such as $a^-a^-a^-$. The most common rotation pattern that more than half of all oxide perovskites have is $a^-a^-c^+$, which leads to the space group $Pnma$ (#62)[82]. Another distortion that is often significant in the $Pnma$ structure is the $X_5^-$ out-of-phase A-site displacement. Unlike the $M_2^+$ and $R_5^-$, the $X_5^-$ often does not show up as an unstable phonon mode in the high symmetry ($Pm\bar{3}m$) phase. Rather, it is an improper order parameter, which attains a nonzero magnitude only because of a trilinear coupling in the Landau free energy

$$\mathcal{F}_{\text{trilinear}} = \gamma M_2^+ \cdot R_5^- \cdot X_5^- . \tag{2.3}$$

The presence of $\mathcal{F}_{\text{trilinear}}$ in the free energy expansion, which is imposed by group theory, guarantees a nonzero $X_5^-$ distortion whenever the octahedral rotations $M_2^+$ and $R_5^-$ are present, no matter the sign of the coupling $\gamma$.

Instabilities in the $A_3B_2O_7$ Ruddlesden-Poppers that are similar to the $M_2^+$ and $R_5^-$ normal modes in the $ABO_3$ perovskites give rise to a wider range of different combinations

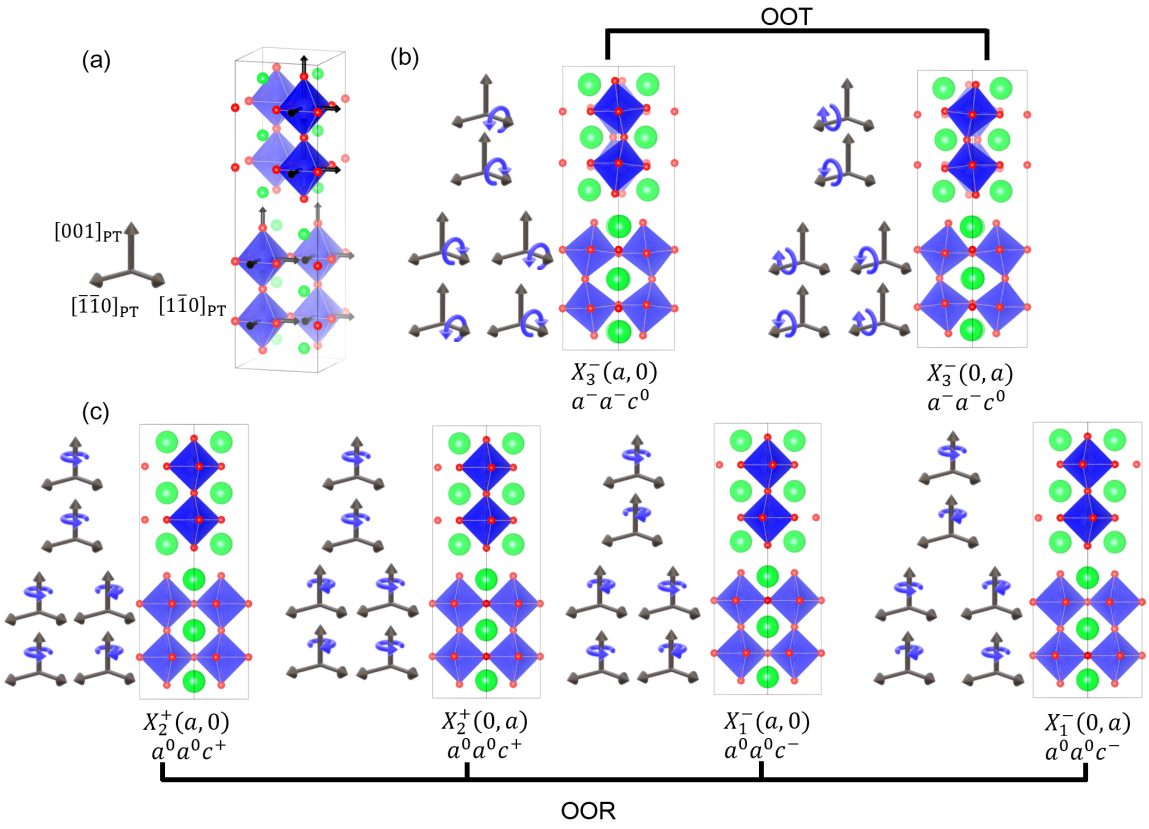


Figure 2.3: **The unstable modes at the $X$ point.** (a) The undistorted structure in the orthorhombic supercell. The arrows on the octahedra are along the orthorhombic axes, and are parallel to the arrows in the other panels which denote the direction of octahedral rotations and tilts. (b)-(d) Distortion modes that correspond to different irreps. Both $X_2^+$ and $X_1^-$ modes are rotations around the c-axis. The $X_2^+$ modes are in-phase while $X_1^-$ modes are out-of-phase. The two components of the $X_3^-$ mode are tilts around axes on $ab$ plane. While the words 'rotations' and 'tilts' are often used interchangeably in the literature, throughout this manuscript we consistently refer to rotations around the c-axis ($X_2^+$ and $X_1^-$) as oxygen octahedral rotations (OOR), and rotations around the axes on the ab plane ($X_3^-$) as oxygen octahedral tilting (OOT).

and resultant symmetries. (For simplicity, we follow the convention to refer octahedral rotations around the out-of-plane ($c$) axis as 'rotations' (OOR), and the rotations around the in-plane axes as 'tilts' (OOT).) One reason for this is that there is a new degree of freedom, since the body-centered primitive cell now contains two oxygen octahedra. Also, the double AO layers break the connectivity of oxygen octahedra, and hence the relative phase of neighboring octahedra on either side of the double layer is not fixed. As an example, we consider the modes relevant to the $A2_1am$ phase observed in $Ca_3Ti_2O_7$ and many other HIF Ruddlesden-Popper compounds in Figure 2.3. In $ABO_3$ perovskites, there are two possible rotation patterns around, for example, the $c$ axis: in-phase ($M_2^+$, $a^0a^0c^+$) or out-of-phase ($R_5^-$, $a^0a^0c^-$). In the $A_3B_2O_7$, on the other hand, there are four instabilities from our phonon calculation results in figure 2.2: The $X_2^+$ mode corresponds to an in-phase rotation of the two octahedra in one perovskite slab that consists of 5 atomic layers, and is the primitive unit cell. However, $X_2^+$ is a two dimensional irrep, and depending on its direction a particular pair of octahedra on either side of a double AO layer can have either in-phase or out-of-phase rotations, as shown on the left two panels of Figure 2.3c. Similarly, the rotations that are out-of-phase within one perovskite slab transform as the two dimensional irrep $X_1^-$, as shown in the right panels of Figure 2.3c.

The most relevant octahedral rotation modes in $A_3B_2O_7$ all have the same wavevector: they correspond to X point normal modes. This leads to a richer set of possibilities for the modes induced by trilinear couplings compared to $ABO_3$ perovskites. In the trilinear coupling terms in $ABO_3$ perovskites, an M and an R mode has to couple with an X mode due to the translational symmetry. In $A_3B_2O_7$ compounds, on the other hand, the trilinear couplings that contain two separate X modes can contain either an M mode or a $\Gamma$ mode

as the third mode. (M point is denoted as the Z point in the convention of Ref.[83].) The reason is that there are two separate X points on the Brillouin zone that are related to each other via a four-fold rotation, and depending on which pair of X wavevectors are chosen, their sum can either give the Γ or the M wavevector. In Table 2.1, we list the possible trilinear couplings between two X modes and a third mode in the $A_3B_2O_7$ structure, and in Figure 2.4, we display the polarization patterns of some of these structures.

| Irrep 1 | Irrep 2 | Coupled irreps | Space group |
|---|---|---|---|
| $X_1^-(a,0)$ | | | $Aeaa$ (#68) |
| $X_2^+(a,0)$ | | | $Aeam$ (#64) |
| $X_3^-(a,0)$ | | | $Amam$ (#63) |
| $X_3^-(a,a)$ | | $M_2^+(c)$ | $P4_2/mnm$ (#136) |
| $X_1^-(a,0)$ | $X_3^-(0,b)$ | $M_5^+(c,0)$ | $Pnab$ (#60) |
| $X_1^-(a,0)$ | $X_3^-(b,0)$ | $\Gamma_5^+(c,0)$ | $C/2c$ (#15) |
| $X_1^-(a,a)$ | $X_3^-(b,b)$ | $M_1^+(c), M_2^+(c), \Gamma_4^+(c), \Gamma_5^+(c,0)$ | $C/2m$ (#12) |
| $X_2^+(a,0)$ | $X_3^-(b,0)$ | $\Gamma_5^-(c,-c)$ | $A2_1am$ (#36) |
| $X_2^+(0,a)$ | $X_3^-(b,0)$ | $M_5^-(0,c)$ | $Pnam$ (#62) |
| $X_2^+(a,a)$ | $X_3^-(b,b)$ | $M_1^+(c), M_2^+(c), \Gamma_4^+(c), \Gamma_5^-(c,0)$ | $C2mm$ (#38) |

Table 2.1: List of structures that can be obtained by combining the unstable $X$ modes. The trilinear couplings are obtained using the 'Invariants' tool in the Isotropy Software Suite[4]. All the phases in this table are considered in the DFT calculations.

Hybrid improper ferroelectricity in the $A_3B_2O_7$ compounds emerges due to the trilinear coupling between $X_2^+$ and $X_3^-$ modes, which induces a polar displacement $\Gamma_5^-$. In the HIF structure with space group $A2_1am$ (#36), each AO layer has a polarization, which are in alternating directions within each perovskite slab, and hence cancel each other - but only partially. As a result, every perovskite slab between the double AO layers have a net dipole moment. These moments order in parallel and give rise to a macroscopic polarization (Figure 2.4a). A different combination of the same X modes can couple to the $M_5^-$ mode, leading to anti-parallel slab dipoles, and hence to an anti-polar phase shown in Fig. 2.4b. (We refer to phases with nonzero dipole moments of each perovskite slab as either polar

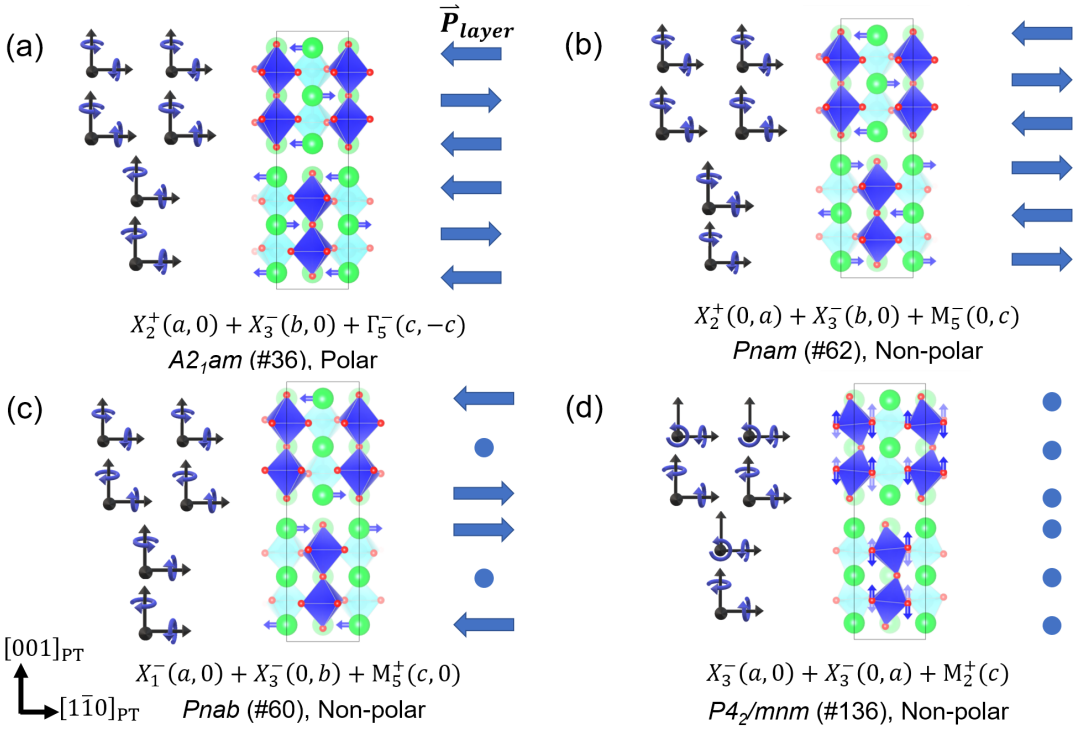


Figure 2.4: **Possible low energy stable and metastable structures** of RP-phase perovskites $A_3B_2O_7$ with more than one oxygen octahedral rotation modes. Analysis of these modes are presented in Table 2.1.

or antipolar.) Other combinations of the X modes couple with different M modes, such as $M_5^+$ or $M_2^+$, and give rise to nonpolar phases, where the dipole moments of each atomic layer cancel each other within each perovskite slab between to double AO layers (Fig. 2.4c-d). (We refer to phases where dipole moments of each slab are zero as 'nonpolar'.) Many of these phases are observed to emerge in various $A_3B_2O_7$ oxides under biaxial strain or equivalent doping, and are also shown to be important as intermediate states in the coherent switching of polarization[40,51,55–57,61]. This is in addition to single-tilt systems observed, for example, at finite temperature[42]. In the next subsection, we draw the strain–tolerance factor phase diagram of these compounds to identify regions where these antipolar and nonpolar multi-tilt phases emerge.

### 2.3.1 Strain Phase Diagram

Most –more than half– of oxide perovskites have a tolerance factor of $\tau < 1$, and attain the space group $Pnma$ at low temperatures[66]. The corresponding octahedral rotation pattern $a^-a^-c^+$ is also common in $A_3B_2O_7$ Ruddlesden-Poppers, and gives rise to the polar space group $A2_1am$ observed in HIFs. In addition to the polar phase, strain phase diagrams of these compounds often abound with transitions to nonpolar phases introduced in the preceding subsection. As an example, in Fig. 2.6a, we present the energy of three lowest energy structures for $Sr_3Sn_2O_7$ as a function of biaxial strain[84]. The zero temperature DFT calculations reproduce the experimentally observed room temperature phase $A2_1am$ in the unstrained compound. Both tensile and compressive strain decrease the energy difference between this phase and the next lowest energy state, and there are phase transitions to nonpolar phases for strain $\gtrsim 2.5\%$ on either direction. Similar strain driven transitions have been predicted for $Sr_3Zr_2O_7$ and $Ca_3Ti_2O_7$ HIF compounds previously, and the pattern of octahedral rotations often change under strain in the $ABO_3$ compounds as well. A common trend in $A^{2+}B^{4+}O_3$ perovskites is that tensile biaxial strain suppresses OOR around the out-of-plane axis, whereas compressive strain enhances it. $Sr_3Sn_2O_7$ follows a similar trend: The transition under tensile strain is to the $P4_2/mnm$ phase, which has only $X_3^-$ tilts, whereas the transition under compressive strain is to the $Aeaa$ phase, which has only the $X_1^-$ rotations around the $c$ axis. The transition to these nonpolar phases is not a result of a continuous suppression of polarization by strain: the magnitudes of polarization in the $A2_1am$ phase on both phase boundaries are sizable, and is even enhanced under tensile strain, as shown in Fig. 2.6(b).

The DFT-calculated energy and polarization of all the 11 compounds in different phases are shown in the Figure 2.5. To be clear, only part of the phases with low energy in the table 2.1 are plotted.

In order to elucidate the behavior of different HIF compounds under strain, in Fig. 2.7 we map out the strain – tolerance factor phase diagram by considering 11 different $A_3B_2O_7$ compounds. (We do not include 2 compounds with larger tolerance factors, since they do not display any OOR or OOT. Most of these compounds have been studied from first principles before, but to the best of our knowledge, this is the first time that this information is compiled to display all compounds together. We consider a strain range of $\pm 4\%$, which covers the experimentally feasible range. For most of the compounds with $\tau < 1$ that we consider, the lowest energy unstrained structure is $A2_1am$, which corresponds to the HIF phase. For $0.92 \lesssim \tau \lesssim 1$, nonpolar structures emerge under both tensile and compressive strain. We observe three different nonpolar structures: $Pnab$ and $P4_2/mnm$ under tensile strain, and $Pnab$ and $Aeaa$ under compressive strain. They correspond to the following changes in the octahedral rotations and tilts:

- **Compressive strain induced OOT suppression (leads to $Aeaa$):** This is observed in $Sr_3Sn_2O_7$ and $Ca_3Ge_2O_7$. The OOT mode amplitude drops to zero and OOR mode phase changes under compressive strain as shown in Fig. 2.10(c),(d).

- **Tensile strain induced OOR suppression (leads to $P4_2/mnm$):** This is observed in $Sr_3Zr_2O_7$ and $Sr_3Sn_2O_7$. Similar to the first situation, but the OOR mode drops to zero under tensile strain instead of OOT mode, as shown in Fig. 2.10(b-c).

- **Tensile/compressive strain induced OOR phase change (leads to $Pnab$):**

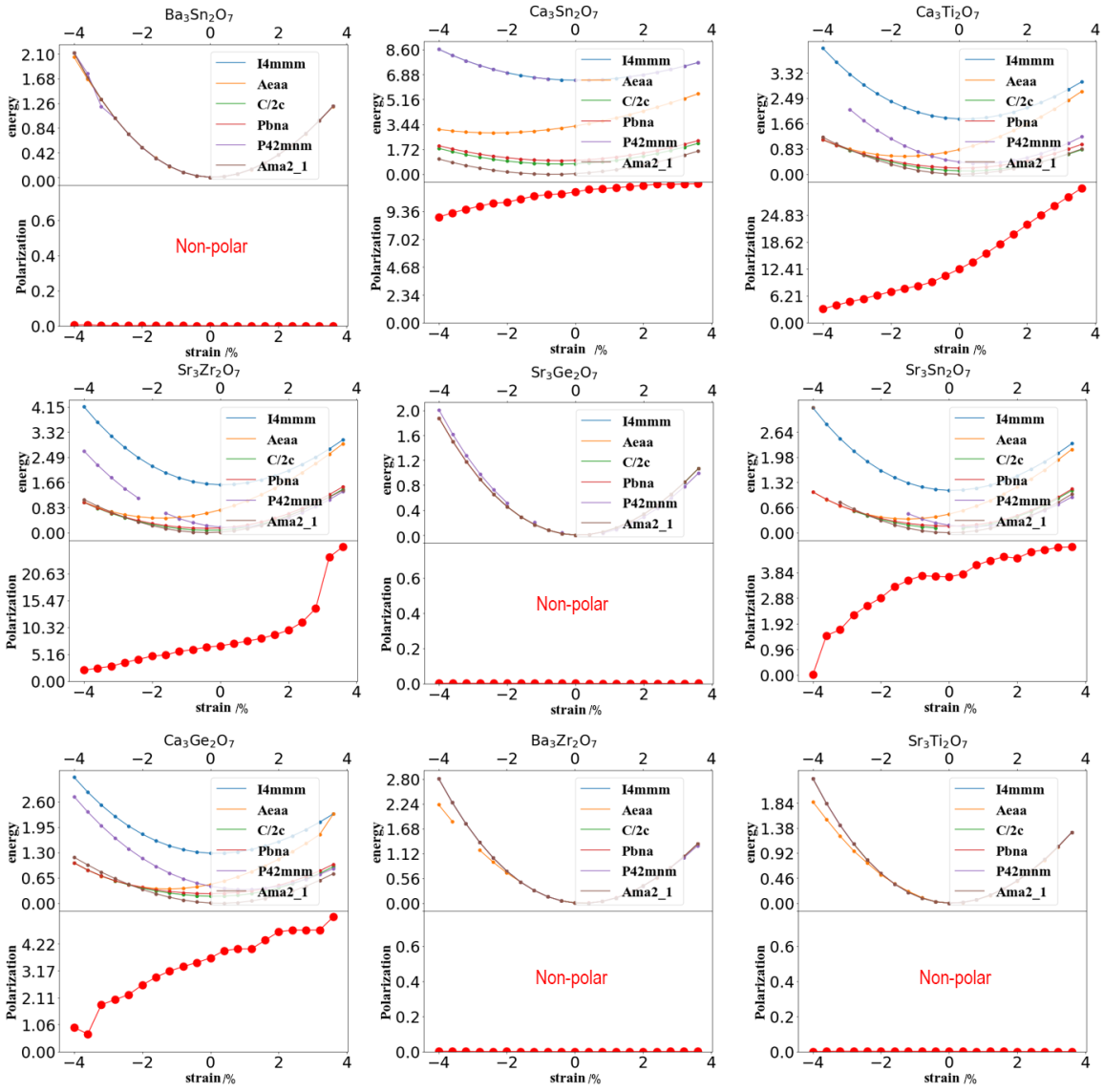


Figure 2.5: Energy and polarization strength of 9 compounds mentioned in the text, with respect to the biaxial strain. The unit of energy is $eV$ and the unit of polarization is $\mu C/cm^2$. Biaxial strain is given by the percentage difference of the in-plane lattice constant from the ground state structure.

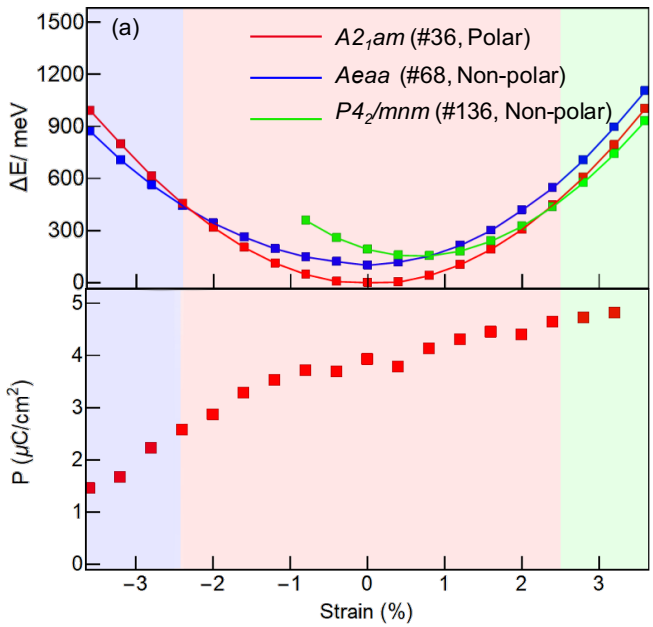


Figure 2.6: **Effect of strain on $Sr_3Sn_2O_7$.**(a) The energy of different metastable phases vary with biaxial strain. Transitions to nonpolar phases are observed on both tensile and compressive strain. (b) The polarization strength of the polar phase as a function of strain. The background colors indicate different ground state structures.

This is observed in $Ca_3Ti_2O_7$ under both tensile and compressive strain, in $Sr_3Zr_2O_7$ under compressive strain, or in $Cd_3Ti_2O_7$ under small tensile as well as compressive strains. (Fig. 2.10(a-b)). Amplitudes of both the OOR and OOT mode retain non-zero, but the in-phase OOR mode changes into out-of-phase manner. This structure is shown in figure 2.4(b). The A-site cations around two interfaces move in the opposite direction, which cancels the polarization in bulk.

Some of these transitions are explained by local measures such as the global instability index (GII), which is known to predict the octahedral rotation patterns and angles in $ABO_3$ perovskites successfully[66,85]. GII is a concept in bond valence model, which is a strong tool to describe the stability of the structures. If the calculated bond valence of a cation/anion is far different from the nominal charge state, it means either that the cation

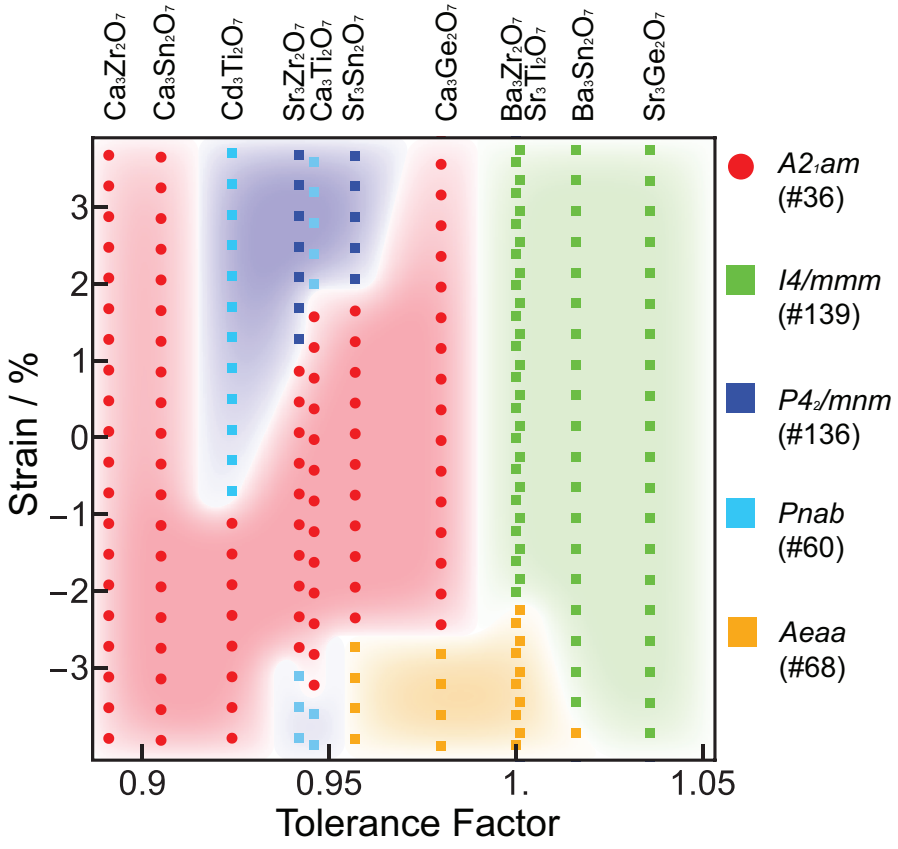


Figure 2.7: **Phase diagram of HIF $A_3B_2O_7$ compounds under biaxial strain.** Red color represents ferroelectric (HIF) phase, the others are all non-polar structures. Results for $Ba_3Ti_2O_7$ (t=1.06) and $Ba_3Ge_2O_7$ (t=1.10), which don't display any rotation or tilting, are not shown here. Proper ferroelectric phases of large tolerance factor compounds, such as the one in $Sr_3Ti_2O_7$ under large tensile strain[1,2], are not displayed either.

is either under-bonded or over-bonded, and it has a tendency to be displaced in order to minimize the energy. Lufaso et al.[66] define a global instability index (GII) to predict overall structural stability:

$$GII = \sqrt{\frac{\sum_{i=1}^{N}[V_{i(ox)} - V_{i(calc)}]^2}{n}} \tag{2.4}$$

Here the $V_{i(ox)}$ is the formal valence of ion i and the $V_{i(calc)}$ is calculated from the bond valence model:

$$V_{i(calc)} = \sum_{j} e^{[R_{ij} - d_{ij}]/B} \tag{2.5}$$

and $d_{ij}$ is the cation–oxygen distance. $R_{ij}$ and B are empirically determined and tabulated. We use the data from IUCr database here.

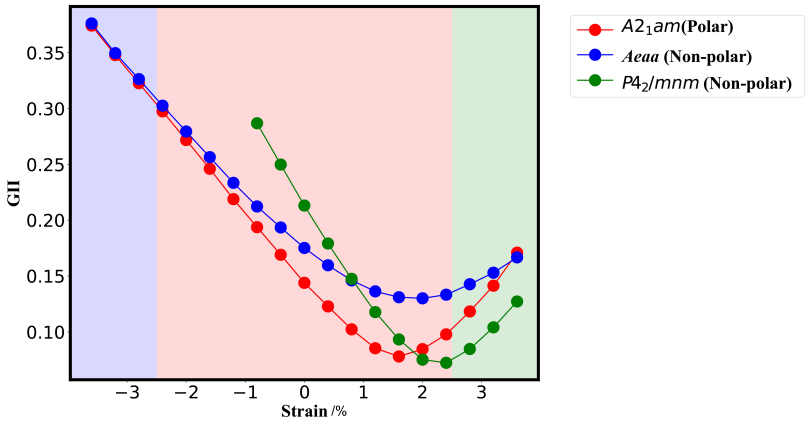


Figure 2.8: The GII calculated for the different phases of $Sr_3Sn_2O_7$. The background color indicates which phases are stabilized from DFT calculation. The tensile-strain induced phase transition is successfully predicted by the bond-valence model.

For $Sr_3Sn_2O_7$, GII calculation successfully predicts the tensile strain induced phase transition, as shown in Figure 2.8. It also provides insight about the driving force of the transition under tensile strain: In Figure 2.9, we plot the bond valence sums for individual

cations. It is seen that the Sr's on the double rocksalt layers (denoted 'interlayer) can satisfy bonding requirements almost equally well in all phases and strain values, possibly thanks to the rumpling degree of freedom. The polar phase $A2_1am$ is causes an unfavorable bond valence sum for the Sr's in the center layer (denoted 'in-layer'). On the other hand, the polar phase leads to a favorable bond valence for the Sn ions, which explains the stability of the polar phase in the low strain region.

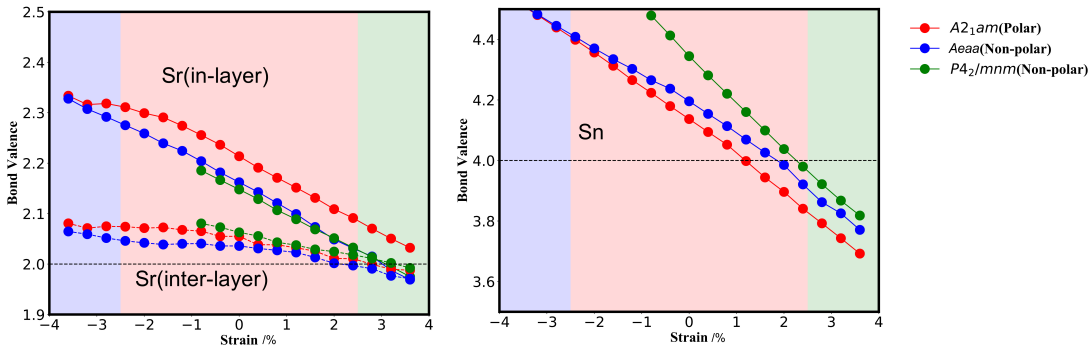


Figure 2.9: The bond valence of different ions in $Sr_3Sn_2O_7$ with respect to strain. Different color represents different phases, the background color indicates the ground state phase.

However, the GII by itself does not explain why the polar $A2_1am$ structure is preferred over the *Aeaa* one, for these two phases have very similar GII values under compressive strain. It is possible that the interplay of GII with the long-range Coulomb interaction (which is an important factor in stabilizing the polarization in proper ferroelectrics such as $BaTiO_3$ [86]) is responsible of the transition to the *Aeaa* phase.

The transition to a single-tilt system can be explained phenomenologically by the cross term between OOR and OOT – a large OOR might suppress OOT and vice versa. All compounds in the $A2_1am$ follow the same aforementioned trend as many $ABO_3$ perovskites that compressive strain enhances OOR, whereas tensile strain enhances OOT (Fig. 2.10a-d). (For example, see Ref's [55,87,88].) This trend is likely the result of the strain reducing

particular B–O bond lengths, which can be increased by the OOT or OOR distortions. The lowest order cross term between the OOR and OOT in the free energy is $F \sim \beta R^2 T^2$ (where we denote the amplitudes of rotations and tilts by $R$ and $T$ respectively). For fixed value of $R$, this term renormalizes the coefficient of the $T^2$ term $\sim \alpha T^2$ as $\sim (\alpha + \beta R^2)$, and hence for large OOR $R^2 > -\alpha/\beta$, the tilting instability is suppressed, and it becomes energetically favorable to have no tilts, as is the case in compressively strained $Sr_3Sn_2O_7$ in the *Aeaa* phase.

A phenomenological explanation of the strain induced transition to nonpolar *Pnab* structure requires not only the biquadratic terms between the OOR and the OOT modes, but also various trilinear terms that couple these modes to other antiferrodistortive displacements[55]. It is particularly interesting that in $Ca_3Ti_2O_7$, this transition is re-entrant in the sense that it happens under both tensile and compressive strains. The GII does not have an obvious trend that explains this transition, and the electrostatic interaction between the O ions on different layers is possibly important. We leave the microscopic explanation of this transition to a future study.

### 2.3.2 Strain tuning of the ferroelectric switching barrier

Enhanced susceptibilities near second order phase transitions can be exploited to design materials with large responses, for example, magnetic permeability or dielectric constants. While no such enhancement of linear susceptibility is mandated near first order transitions, it is nevertheless possible to obtain large response near a first order phase boundary if the external field can induce the transition. Examples of demonstrations of this approach include Terfenol, $Pb(Zr,Ti)O_3$, and $BiFeO_3$[89–91]. The phase boundaries of structural tran-

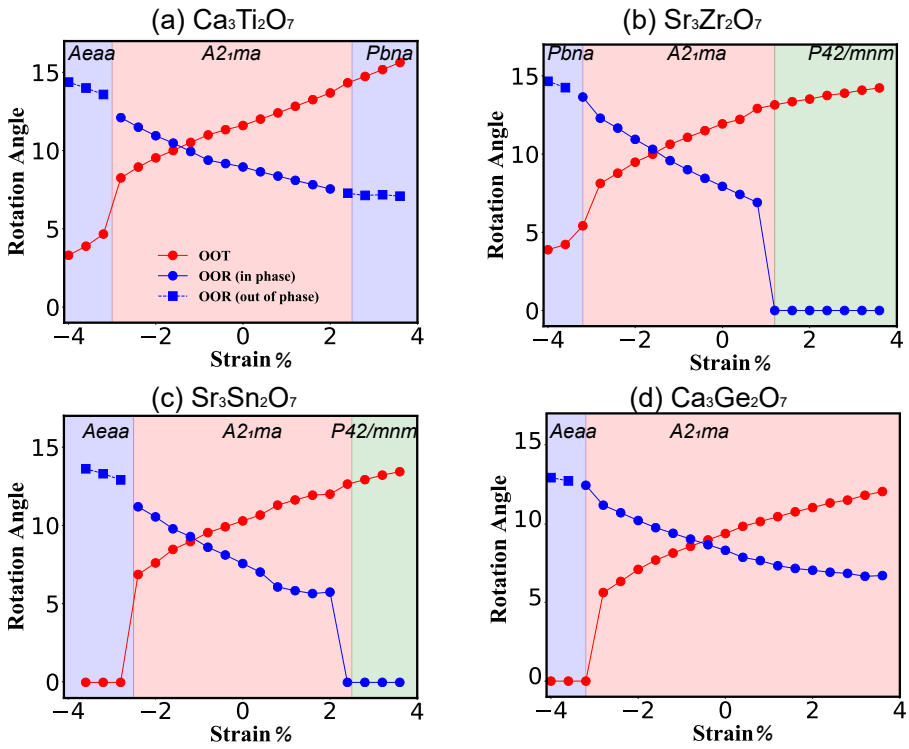


Figure 2.10: **Effect of Strain on Crystal Structure.** Rotation (OOR) and tilting (OOT) angles as a function of epitaxial strain in (a) $Ca_3Ti_2O_7$, (b) $Sr_3Zr_2O_7$, (c) $Sr_3Sn_2O_7$ and (d) $Ca_3Ge_2O_7$. Different colors represent different phases. Red regions are the ferroelectric phase.

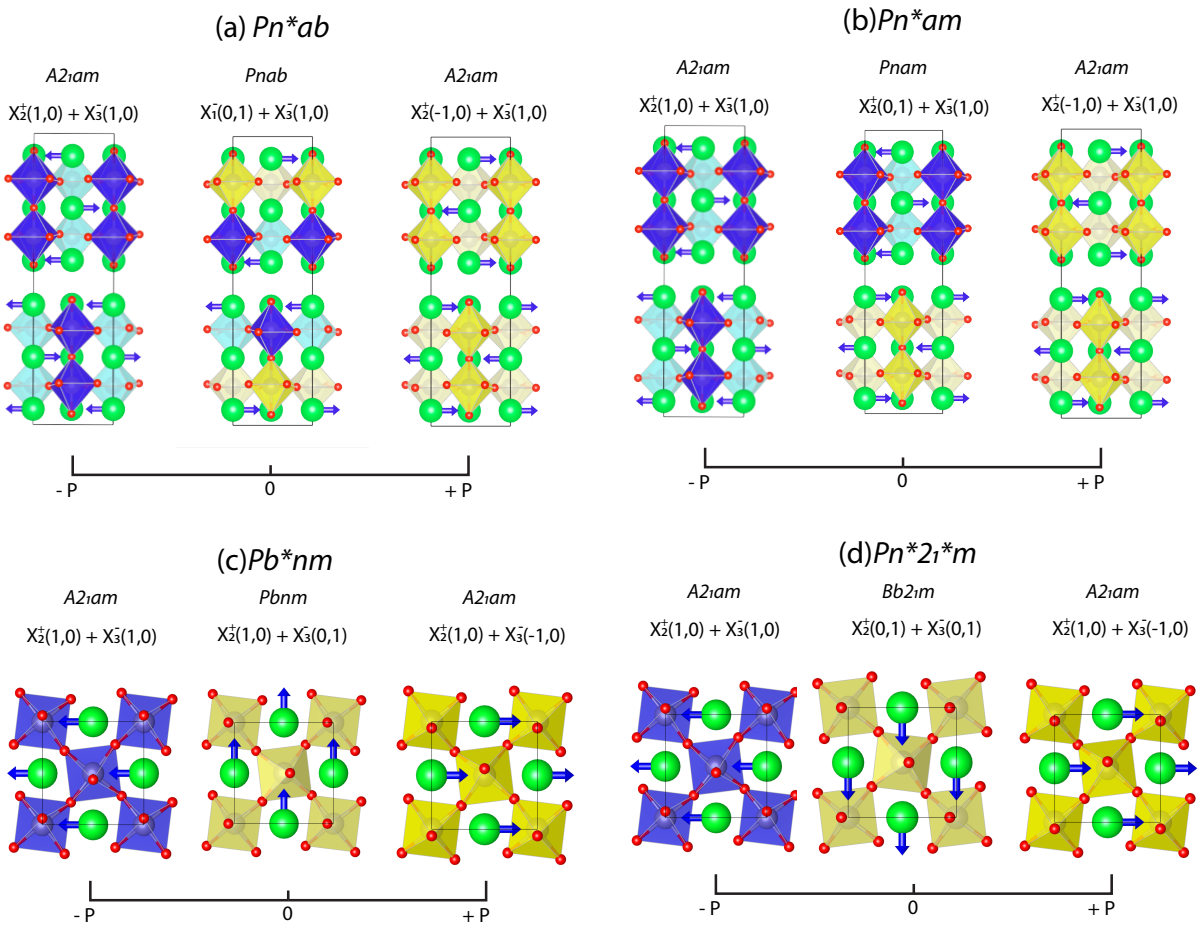


Figure 2.11: **Four possible polarization switching pathways.** (a)$Pn^*ab$, (b)$Pn^*am$ (c)$Pb^*nm$ (d)$Pn^*2_1^*m$. The octahedra that remain in their original rotation direction are shown in blue, whereas those that switch their rotation direction are shown in yellow.

sitions depend on strain very sensitively, and as a result, this approach is a promising means to enhance the response of materials via strain.

The question we focus on in this subsection is whether the ferroelectric polarization switching barrier is affected when strain is used to tune the materials to the vicinity of the polar-nonpolar phase transitions. In order to answer this question, we use the minimum energy barrier for coherent polarization switching as a proxy to the coercive electric field.

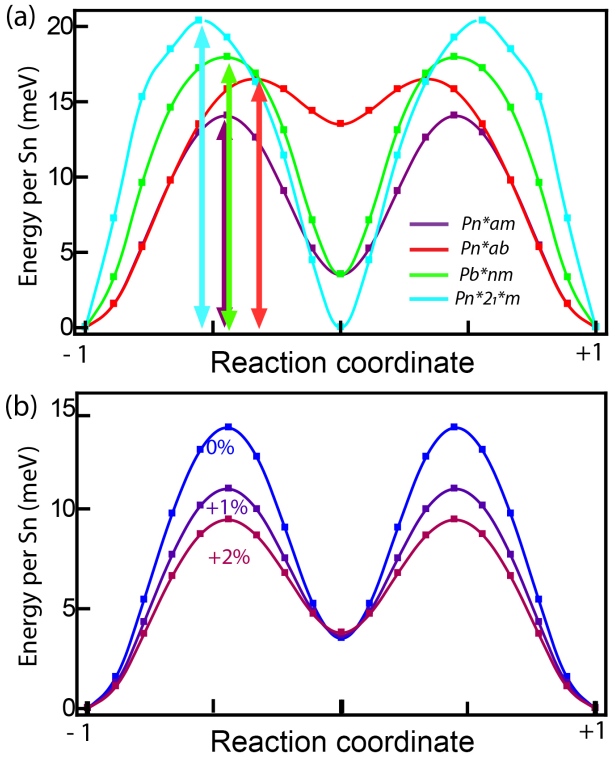


Figure 2.12: **Energy Barriers for Polarization Switching in $Sr_3Sn_2O_7$.** (a) The energy barriers of different pathways for unstrained $Sr_3Sn_2O_7$. The horizontal axis is the "reaction coordinate" that parametrizes the switching path. Arrows indicate the barrier heights. (b) The energy of the $Pn^*am$ pathway in $Sr_3Sn_2O_7$, as a function of tensile biaxial strain.

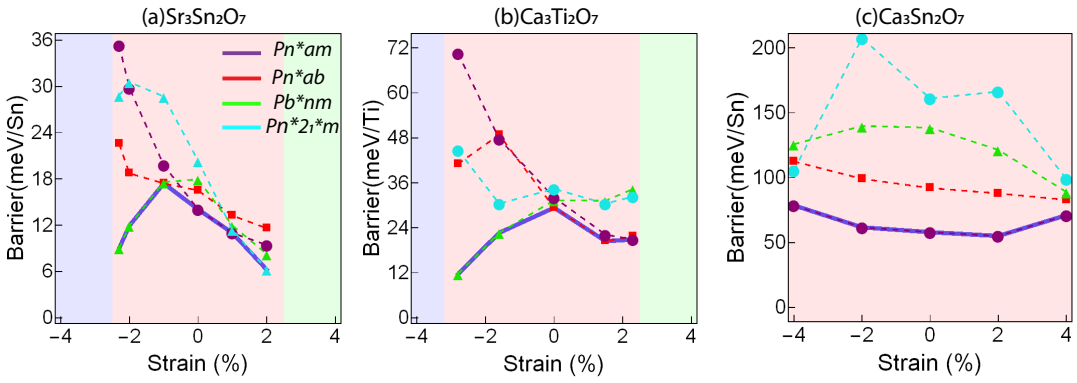


Figure 2.13: **The polarization switching barrier per B-site atom** for (a) $Sr_3Sn_2O_7$, (b) $Ca_3Ti_2O_7$ and (c) $Ca_3Sn_2O_7$. The barriers for three distinct pathways are shown here, whilst the thick blue line is the minimum among those three. Background colors indicate different ground states.

While in an actual experiment defects, domain structure, as well as size and shape effects significantly alter the coercive field, trends of coherent switching barrier can be used as a first principles proxy to the trends of the coercive field[92] as explicitly shown in $HfO_2$[54]. (Finite element methods which take into account the domain structure provide much lower switching barriers[93].) In practice, the coherent switching field calculated from the first principles energy barrier by assuming that the dipole moment in every unit cell of an infinite crystal switches at the same time is a gross overestimate. As a result, we don't report the electric field required for switching, but instead report only the energy barriers.

Since in the hybrid improper ferroelectric $A_3B_2O_7$ compounds the polarization emerges as an improper order parameter through a trilinear coupling with rotation and tilting modes, switching one of these two modes is necessary to switch the polarization. It was recognized as early on as in the first HIF paper that this makes different switching pathways possible, and that the corresponding energy barriers can be tuned by strain[37]. Later, the work of Nowadnick and Fennie[56] analyzed the possible roles of different switching mechanisms,

and Munro et al. used the idea of distortion symmetry groups to identify other switching pathways[57,68]. Since then, the energetics of switching in various HIF compounds have been studied, for example in Ref.[94]. However, to the best of our knowledge, a comparison of different compounds and their strain dependence have not been performed yet.

In Fig. 2.11(a-d), we show four possible polarization switching pathways. We follow the convention of the distortion symmetry groups to name these pathways[68]. This process involves identifying not only the symmetry operations shared by all images on the pathway, but also those operations that reverse the distortion, which is the polarization in this case. The latter are referred to as distortion reversal symmetries, and are denoted by a '*' superscript. For example, $Pn^*ab$ means that each image along the switching path has two glide planes with translations along a and b axes; and the glide plane $n^*$ reverses the distortion. Three of the switching paths we consider ($Pn^*ab$, $Pb^*nm$ and $Pn^*am$) have a similar name as their intermediate phase (up to the asterisks), because the spatial symmetry elements of the intermediate phase either remain unchanged or become reversal symmetry operation for other images. But this is not the case for $Pn^*2_1^*m$. All of the four are so-called 2-step switching pathways, where there exists a local minimum of energy on the switching path, as seen from Fig. 2.12(a), and they are the lowest ones among such paths for the 3 compounds we considered. They each have distinct intermediate states, but the same initial and final states. Since the Ruddlesden-Popper structure consists of weakly bound perovskite blocks separated by an interface between two rock-salt AO layers, it is possible to consider supercells extended along the [001] direction, and polarization being switched in one perovskite block at a time. This, in principle, gives rise to an infinite number of different switching pathways, the barrier energy per formula unit can be arbitrarily small (since only one block

out of arbitrarily many switches at each step.) This has been observed in Ref's[57,94], where typically the 4-step switching paths have lower (but comparable) barriers than the 2-step ones, which in turn have lower barriers than the single-step paths. (The path with a very large number of steps can be considered to be a simple model of domain wall in motion along the [001] direction.) However, this does not necessarily imply that the pathway with the highest number of steps determines the coercive field, because what is more important for the switching under an electric field is the slope of the energy vs. polarization curve[92]. For simplicity, as well as computational manageability, we focus only on 2 step switching pathways.

Each of the four pathways can be reproduced within the same doubled conventional cell as the polar structure. The $Pn^*ab$ and $Pn^*am$ pathways (Fig. 2.11(a-b)) involve changes in the direction of the OOR mode, and both of them have nonpolar intermediate structures, with space groups $Pnab$ and $Pnam$ respectively. The out-of-phase displacements of the A-site cations are along the polar axis in both of these intermediate structures. The $Pb^*nm$ pathway involves switching the direction of the OOT mode ($X_3^-$), whereas in the $Pn^*2_1^*m$ both OOR and OOT change directions, as shown in Fig. 2.11(c-d). Mode decompositions of these switching pathways are given in figure 2.14.

In Fig. 2.12(a), we plot the energy as a function of the reaction coordinate for these four switching pathways in unstrained $Sr_3Sn_2O_7$. The energy barriers are comparable and the lowest one is for the $Pn^*am$ pathway. Results presented in Fig. 2.12(b) show how the energetics of this path behaves under tensile strain: Tensile strain monotonically decreases the $Pn^*am$ switching barrier, thus lowering the expected coercive field required for switching. This is not a surprising result, since the OOR's weaken under tensile strain, as shown

in Fig. 2.10(c) and the $Pn^*am$ pathway involves a change in the OOR character. What is interesting, and important for applications, is that this reduction in the switching barrier is not accompanied with a lower polarization under tensile strain (Fig. 2.6). Thus, *strain can be used as a means to lower the coercive field of hybrid improper ferroelectrics.*

The strong strain dependence of the switching barrier is not specific only to $Sr_3Sn_2O_7$, or the $Pn^*am$ pathway. In Fig. 2.13(a-b), we show the barrier for different switching paths of $Sr_3Sn_2O_7$ and $Ca_3Ti_2O_7$ as a function of strain throughout the strain range that the HIF phase is stable. While the error bars in the energy barriers from the NEB calculations cause the curves to be rather rugged, two trends are evident: *(i)* under tensile strain, the barriers for pathways that involve changing the direction of the OOR mode ($Pn^*am$ and $Pn^*ab$) are lowered, and *(ii)* under compressive strain, the barrier for the pathway that only involve changing the direction of the OOT mode ($Pb^*nm$) is lowered. These are consistent with the tendencies towards OOR and OOT distortions becoming weaker under tensile and compressive strain as discussed earlier. Near 0% strain, the lowest barrier pathway switches from $Pb^*nm$ or $Pn^*2_1^*m$ to either $Pn^*ab$ or $Pn^*am$, and either strain direction leads to a lower coherent switching energy barrier. The lowest barriers are obtained near the phase boundaries between the polar and nonpolar phases, and the maximum suppression is about 50% in both compounds.

$Ca_3Sn_2O_7$ has a lower tolerance factor than $Sr_3Sn_2O_7$ and $Ca_3Ti_2O_7$, and it does not display a strain induced phase transition in the strain range we considered. It does not show a strain induced change in the switching pathway, or a significant decrease in the switching barrier either (Fig. 2.13(c)). This is likely because this compound is very far from the phase boundaries, and with its small tolerance factor, it has such large OOR and OOT that the

strain induced changes in the instabilities are inconsequential.

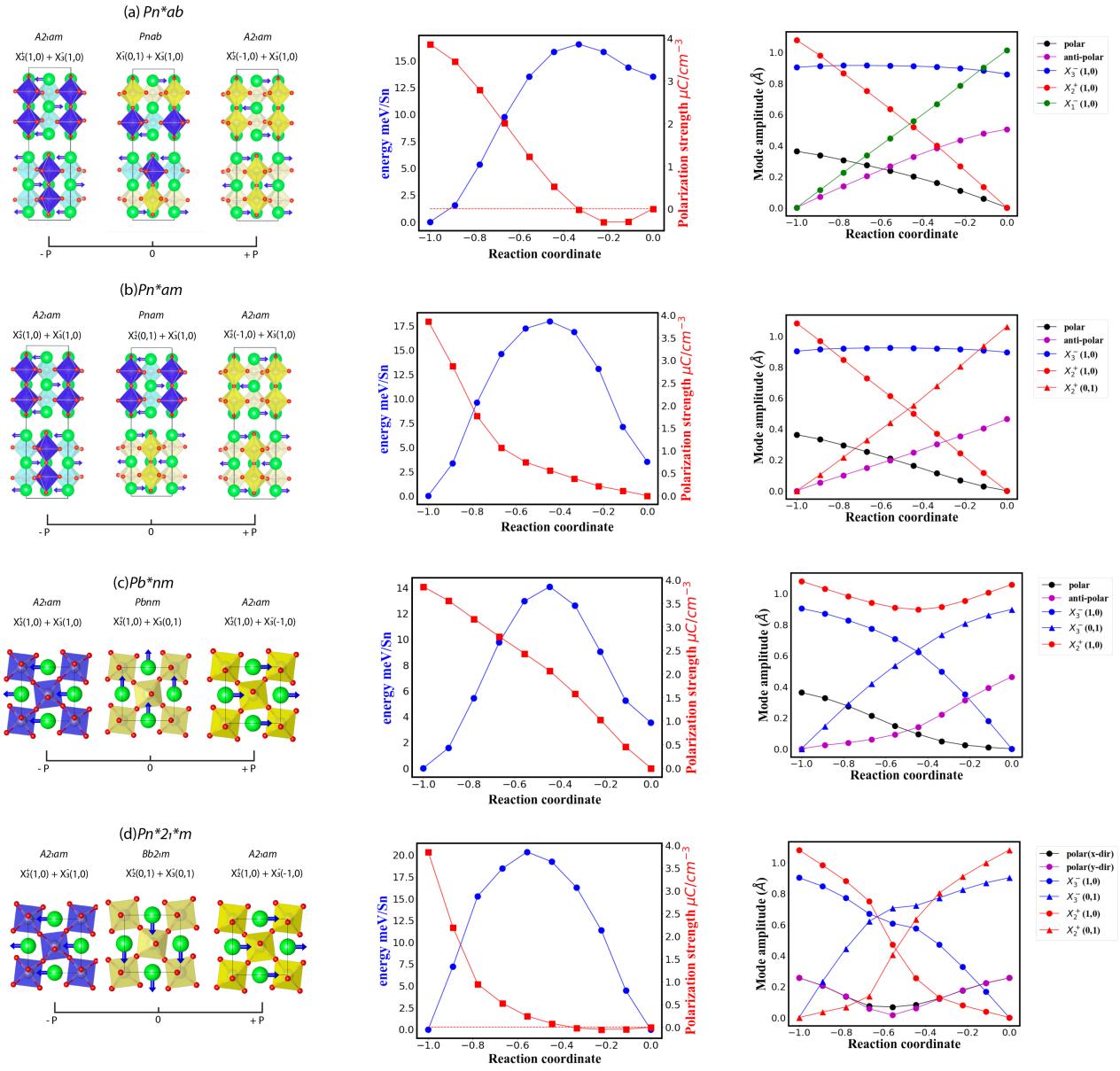


Figure 2.14: Four possible polarization switching pathways (a)$Pn^*ab$, (b)$Pn^*am$ (c)$Pb^*nm$ (d)$Pn^*2_1^*m$ of $Sr_3Sn_2O_7$. Blue octahedra indicates it stays in the initial position, yellow means it is no longer in the original position. The second column is the energy/polarization vs. Reaction coordinate. The third column is the Mode amplitude vs. Reaction coordinate.

## 2.4 Discussion

Since its discovery about a decade ago, hybrid improper ferroelectricity have provided fertile ground for first principles materials by design approaches. Experiments have also been been catching up rapidly, verifying theoretical predictions. Multiple hybrid improper ferroelectric Ruddlesden-Popper phases have already been synthesized using bulk methods (for example[39–41,46]). Although thin film growth of Ruddlesden-Popper phases, especially for thermodynamically unstable compositions and at large strain values, is usually challenging because of the required stoichiometry control, there has been successful demonstration of switchable HIF in PLD grown films[51], and both hybrid and conventional oxide molecular beam epitaxy have been used to synthesize phases that are not thermodynamically stable[2,95]. Current efforts focus on understanding more than the emergence of ferroelectricity, and to find ways to optimize properties such as the coercive field required for polarization switching.

In this chapter, we used first principles calculations to shed light on the strain–tolerance factor phase diagram of $n = 2$ Ruddlesden-Popper HIF's, and to come up with a design strategy for obtaining lower coherent switching energy barriers. This quantity, which we used as a proxy for the coercive field, decreases significantly when strain is used to tune the HIF's to the nonpolar phase boundaries, because of the weakening of one of the rotation or tilt modes. We further showed that this weakening, and the resulting decrease in the switching barrier, is not always accompanied with a decrease in the polarization magnitude, for example in $Sr_3Sn_2O_7$, verifying the point made early on in Ref.[44] that a lower barrier does not necessarily mean a lower polarization. Our results thus show that biaxial strain,

which has historically been used to induce ferroelectricity in many oxides, can also be used as a means to tune the coercive field of hybrid improper ferroelectrics.

# Chapter 3

# Free carrier induced ferroelectricity in layered perovskites

This chapter is adapted from my work *Free-Carrier-Induced Ferroelectricity in Layered Perovskites*[96].

Doping ferroelectrics with carriers is often detrimental to polarization[97]. This makes the design and discovery of metals that undergo a ferroelectric-like transition challenging. In this chapter, we show from first principles that the oxygen octahedral rotations in perovskites are often enhanced by electron doping, and this can be used as a means to strengthen the structural polarization in certain hybrid-improper ferroelectrics – compounds in which the polarization is not stabilized by the long range Coulomb interactions but is instead induced by a trilinear coupling to octahedral rotations. We use this design strategy to predict a cation ordered Ruddlesden-Popper compound that can be driven into a metallic ferroelectric-like phase via electrolyte gating.

## 3.1 Background

Ferroelectrics, insulators with a spontaneous and switchable electric polarization, are promising for a wide range of applications and pose a number of fundamental questions[47,98–100]. While ferroelectricity is observed in a wide range of material classes and can be driven by a variety of mechanisms, the most studied ferroelectrics are transition metal oxides, such as $BaTiO_3$, where the emergence of a polar order parameter is due to a crystal structural distortion driven by the interatomic hybridization and long range Coulomb interactions[13,86]. Because of the role of the long range interactions in driving the polar structural distortion, introduction of free charge carriers to ferroelectrics not only screens the ferroelectric polarization, but it also suppresses the structural distortion often[101].

While 'structurally polar metals' (metals with a polar point group) are rather common, 'ferroelectric metals' (metals that undergo a phase transition from a centrosymmetric to a polar crystal structure[102]) are rather rare. It took almost 50 years after the possibility of a ferroelectric-like transition in a metal was first raised[103] for the unambiguous experimental observation of such a transition in $LiOsO_3$[104]. The first observation of polarization switching in a ferroelectric (semi-)metal is even more recent[105,106]. The interest in polar and ferroelectric-like metals is continuing to increase in both bulk and heterostructures[107–118] and they continue to promise both a fertile playground for interesting emergent phenomena (including, but not limited to mixed singlet-triplet superconductivity[119] and novel optical effects[120]), and immediate relevance to applications as polar electrodes[121].

Emergence of polarization in $(Sr,Ca)Ru_2O_6$, $Ca_3Ru_2O_7$, and ultra-thin $NdNiO_3$ films have been studied in detail[122–124]; and it was shown that the polarization in these materials

is robust against metalicity because the polar displacements are driven by their coupling to zone-boundary phonon modes and are mainly decoupled with the electrons around Fermi level. 'Metallized ferroelectrics' (insulating ferroelectrics that are doped to introduce charge carriers) are also studied intensively, and the effects of free carriers on the polarization and polar instabilities are analyzed recently introducing ideas such as metascreening[97], and elucidating the trends in the second-order Jahn-Teller effect under carrier doping[125]. Barring a volume expansion, the most common effect of charge doping in proper ferroelectrics is the suppression of the ferroelectric polarization; for example, ∼0.11 electrons per formula unit is sufficient to completely suppress the polarization in $BaTiO_3$ and render it centrosymmetric[101,126,127].

In this subsection, we show that the $A_3Sn_2O_7$ hybrid-improper ferroelectrics (HIFs)[37,39,40,128,129] behave differently, and their structural polarization is strongly enhanced by the free electrons introduced by chemical doping or electrostatic gating. This is related to an increase in the oxygen octahedral rotation angles induced by the added electrons in the parent perovskite compounds, which in turn leads to a larger structural polarization in these layered perovskite Ruddlesden-Popper (RP) phases[77]. We also show that it is possible to exploit this mechanism to obtain free carrier *induced* polarization, in other words, design a material that develops a ferroelectric-like structural instability when free electrons are introduced via, for example, electrostatic or electrolyte gating.

### 3.1.1 Methods

The Density functional theory calculations are performed using the projector augmented wave approach[31] as implemented in the Vienna Ab-initio Simulation Package (VASP)[58,59],

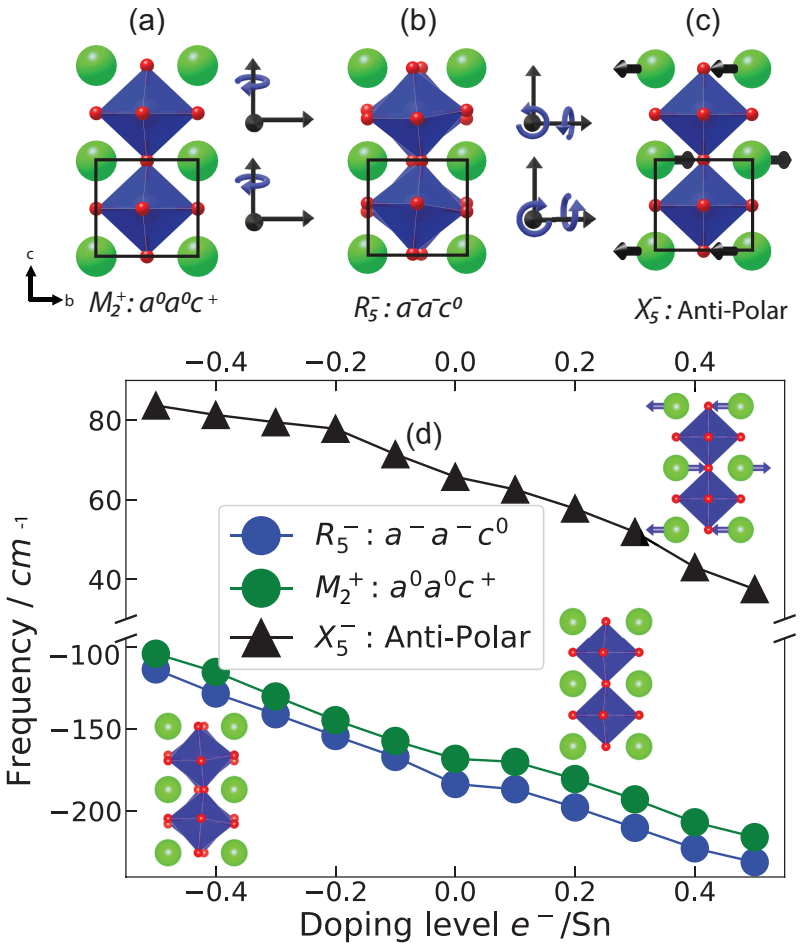


Figure 3.1: (a)-(c)The three normal modes in Eq. 3.2 that are relevant to the *Pnma* phase of perovskites and (d) (d) The phonon frequencies of cubic ($Pm\bar{3}m$) $SrSnO_3$ under doping and fixed volume. The green and red spheres represent the A-site and oxygen ions respectively, and the B-site atoms are in the center of the blue octahedra. (a) In-phase rotation around the c-axis ($a^0a^0c^+$ in Glazer notation). (b) Out-of phase rotation around the ab-axis $a^-a^-c^0$. (c) The anti-polar displacement in the ab-plane, where the irrep direction is $X_5^-(a, a; 0, 0; 0, 0)$. With increasing number of electrons, the unstable rotation modes get more unstable, and the anti-polar $X_5^-$ mode gets softened (but remains stable).

and using the PBEsol generalized gradient approximation[60] and a 500 eV plane wave cut-off. A $\sqrt{2} \times \sqrt{2} \times 2$ supercell, which can capture the $a^-a^-c^+$ octahedral rotation pattern (No.62, *Pnma*), was used for $ABO_3$ perovskites. For $A_3B_2O_7$ Ruddlesden-Popper structures, a $\sqrt{2} \times \sqrt{2} \times 2$ supercell was used. A $6 \times 6 \times 4$ k-grid was used for the perovskite supercells, and a $6 \times 6 \times 2$ k-grid for the Ruddlesden-Popper supercells was used for all calculations except the DOS calculations which required a finer grid. For structural relaxations, the residual force tolerance was set to 1 meV/Å. Different space groups are also considered during this process, detailed information can be found in the following sections. In all compounds considered, the octahedral rotation patterns and space groups consistent with previous reports were found to be the lowest energy ones.

The carrier doping without substituting or adding atoms is simulated by increasing the number of electrons in the DFT calculations. In this approach, in order to ensure the charge neutrality in presence of the free carriers, a uniform background with opposite charge is also added. Since the absolute energy between different doping levels are not compared and only the relative energy with same doping level is important, no energy corrections were made to compensate for this artifact. Most of the trends reported consider ionic relaxations at fixed unit cell volume and shape, and the trends are qualitatively similar when cell volume is relaxed as well.

The Landau free energy expansion was built using the irreducible representations (irreps) of the cubic $Pm\bar{3}m$ structure. Irreps that are relevant to the $Pm\bar{3}m$–Pnma phase transition were determined using the ISODISTORT tool of the Isotropy Software Suite[71]. The irreps being considered first are $M_3^+(0,0,a), R_5^-(a,a,0)$ and $X_5^-(a,a;0,0;0,0)$. The free energy upto 4th order was considered, and a mesh of finite displacements of these irreps with 10

steps on each direction was used for DFT calculations, which totals up to $10\times10\times10 = 1000$ data points for one fitting. The parameters of the free energy were fit to the DFT energies on this grid using the standard fitting algorithms as implemented in Numpy[130]. There are also other irreps including $M_2^+$ and $R_4^-$ present during the phase transition from $Pm\bar{3}m$ to $Pnma$, which are also considered in our calculations by fixing the ratio of $\frac{|M_2^+|}{|M_3^+|}$ and $\frac{|R_4^-|}{|R_5^-|}$.

Polarization is not a well defined quantity in metals. The amplitude of the polar structural mode is often used as an alternative to the polarization in metallic solids, but this approach does not provide any information on the ionic charges at all. An alternative is to calculate the polarization of the fully filled bands only, or if there are relatively flat bands, to use a generalized Berry phase formalism that takes into account different numbers of bands at each k-point[131]. We use a simplified approach where the polarization is calculated by the product of nominal charges and polar displacements:

$$\vec{P} = \sum_i \vec{u}_i^{\Gamma} Z_i \tag{3.1}$$

where the $\vec{u}_i^{\Gamma}$ represents the displacement vectors of atom $i$ and $Z_i$ is the nominal ionic charge of atom $i$. Using the Born effective charges of the undoped compounds instead of the nominal ionic charges would not lead to a qualitative difference. The nominal, as well as the in-plane Born effective charges in undoped $Sr_3Sn_2O_7$ are shown in Table. 3.1. An advantage of this approach, as opposed to just using the polar mode amplitudes without multiplying with charges, is that the acoustic mode (which can be considered as nothing but an origin shift) is taken off by default since the sums of the charges is zero.

In order to determine the ground state of the Ruddlesden-Popper structures, several

| Atom | Wyckoff position | Nominal charge | Born effective charge (xx-direction) |
|---|---|---|---|
| Sr | b | +2 | +2.3 |
| Sr | e | +2 | +2.1 |
| Sn | e | +4 | +4.0 |
| O | a | -2 | -1.5 |
| O | e | -2 | -3.0 |
| O | g | -2 | -1.6 |

Table 3.1: The nominal and Born effective charges in $Sr_3Sn_2O_7$.

candidate structures with different octahedral rotation patterns are considered. (See Table 2.1 in chapter 2.) The only structure with a polar point group is $A2_1am$, and hence we only refer a material as hybrid improper ferroelectric only when the $A2_1am$ phase has lowest energy.

## 3.2 Electrostatic gating in $ABO_3$ Perovskites

Before we move into the layered perovskites, the electrostatic gating effect over $ABO_3$ perovskites is a better start point. As stated in chapter 2, most $ABO_3$ perovskite oxides have the orthorhombic space group of $Pnma$ at low temperature[66]. The atomic displacements that lead to the $Pnma$ symmetry can be expanded in terms of the irreducible representations (irreps) of the reference space group $Pm\bar{3}m$[132,133]. The $Pnma$ structure has multiple nonzero strains ($\Gamma_1^+$, $\Gamma_3^+$, $\Gamma_5^+$) and atomic displacements ($R_4^-$, $R_5^-$, $X_5^-$, $M_2^+$, and $M_3^+$). Most of these distortions are 'secondary': they are nonzero only because of couplings with other, 'primary' distortions. The $Pnma$ structure can be obtained by a combination of only two primary irreps ($R_5^-$ and $M_2^+$) which correspond to the out-of-phase and in-phase oxygen octahedral rotations shown in Fig. 3.1a-b[134]. The $Pnma$ structure ($a^-a^-c^+$ in the Glazer notation) has out-of-phase rotations around [110] and in-phase rotations around [001], which

is equivalent to order parameter directions $R_5^-(a,a,0)$ and $M_2^+(0,0,a)$. These two modes, which we henceforth refer to as $R$ and $M$ for brevity, couple with the $X_5^-(a,a;0,0;0,0)$ mode (referred to as $X$ for brevity) at the trilinear order. Hence, the Landau free energy up to third order is

$$\mathcal{F} = \alpha_R R^2 + \alpha_M M^2 + \alpha_X X^2 + \gamma R \cdot M \cdot X \tag{3.2}$$

The X mode corresponds to an out-of-phase displacement of the A-site cations as showed in Fig. 3.1c, and is typically stable, but it has a nonzero amplitude $X = \gamma RM/2\alpha$ in the low temperature structure. $X$ can be referred to as a 'hybrid-improper' order parameter, because it is induced in the ground state by a combination of two primary order parameters. In heterostructures where translational symmetry is broken by layered cation ordering, or in layered perovskites (RPs), modes that give rise to transverse out-of-phase displacements of the A site (related to the $X_5^-$ in perovskites) attain a polar character, and are responsible of the hybrid-improper ferroelectricity[37,44,135]. For this reason, understanding the behavior of this mode in bulk perovskites is essential for understanding the polarization trends in HIFs.

As an example $Pnma$ perovskite system, we consider $SrSnO_3$ first. While $SrSnO_3$ is orthorhombic at room temperature, its Goldschmidt tolerance factor $t = \frac{R_{Sr}+R_O}{\sqrt{2}(R_{Sn}+R_O)} = 0.96$ is close enough to 1 so that it undergoes a series of phase transitions to the cubic phase above 1295 Kelvin and its structural ground state can be modified by biaxial strain[52,136]. In Fig. 3.1(d), we show the phonon frequencies for the $R$, $M$, and the $X$ modes as a function of doping from first principles DFT calculations. The phonon frequencies are proportional

to the square root of the $\alpha$ coefficients in Eq. 3.2, and can be used to study the instabilities. Unstable modes have imaginary frequencies, which are plotted as negative numbers. We simulate the effect of free carriers in this nominally insulating compound by changing the total number of electrons in the calculation, while keeping the system neutral by adding a homogeneous background charge. Unlike chemical substitution, this approach does not introduce any steric differences or disorder into the system. In this respect, it is a better representation of electrostatic or electrolyte gated systems rather than chemical doping. We consider a wide range of carrier doping up to 0.5 electrons per Sn atom, which is larger than the typical concentrations experimentally achievable[137]. We keep the unit cell volume fixed in order to separate out the volume expansion effects. The volume expansion does not modify the trends we report significantly, which we will discuss in the following section.

The results in Fig. 3.1d show that both the rotation modes $R_5^-$ and $M_2^+$, which have imaginary frequencies in the undoped compound, become more unstable with the introduction of free electrons, in other words, $\alpha_R$ and $\alpha_M$ become more negative with added electrons. Similarly, the frequency of the stable $X_5^-$ mode decreases with increasing electron concentration, and so $\alpha_X$ becomes smaller. The trilinear coupling $\gamma$ doesn't change significantly under doping, and the changes in the higher order coefficients are qualitatively insignificant, which we will show by Landau energy analysis in the next section. As a result, the softening of $X_5^-$ and the strengthening of the $R_5^-$ and $M_2^+$ instabilities under electron doping lead to larger rotation angles and antipolar amplitudes as shown in Fig. 3.7. This trend is observed not only in *Pnma* perovskites $SrSnO_3$ and $CaSnO_3$, but also in cubic perovskites like $BaZrO_3$, which develops a $R_5^-$ instability when electron doped, as shown in figure 3.2. A similar enhancement of octahedral rotations was predicted by DFT in

$SmNiO_3$ [138]; and both DFT and X-ray diffraction points to enhanced octahedral rotations in photodoped $EuTiO_3$ [139].

In Fig.3.2, the oxygen octahedral rotation angle and anti-polar $X_5^-$ mode amplitudes of Zr- and Ti- based perovskites are shown as a function of carrier doping. Compared with Sn-based perovskites, the distortion modes in these transition metal based perovskites are generally less sensitive to doping. This is likely because the transition metal Zr and Ti ions have unfilled d-orbitals, which form the bottom of the conduction band, and get filled first when electrons are introduced to the system. The lower lying $d$ orbitals are of $t_{2g}$ character, and hence have nodes in the directions of the oxygen ions. In the Sn based perovskites, the bottom of the conduction band is formed by the Sn 5s orbitals, which are larger than the d orbitals, and do not have an nodes.

This effect of carriers on octahedral rotations can be explained by considering the densities of states, which is plotted in the figure 3.3. The valence bands in stannates consist of oxygen-p bands, whereas the the conduction band is formed by Sn-s [140]. The added electrons fill states with Sn-s character, and the valence of $Sn^{4+}$ becomes $Sn^{+4-\delta}$. This decreases the Sn-O electrostatic attraction, decreases the Sn-O hybridization, and increases the ionic radius of Sn. This reduces the tolerance factor $t$. Added holes, on the other hand, occupy the $O^{2-}$ anions and make them $O^{-2+\delta}$. This reduces the attraction between the A site cation (Ba, Sr, or Ca) and oxygens, which is the driving force of rotational instabilities. Hence, rotation modes become less unstable.

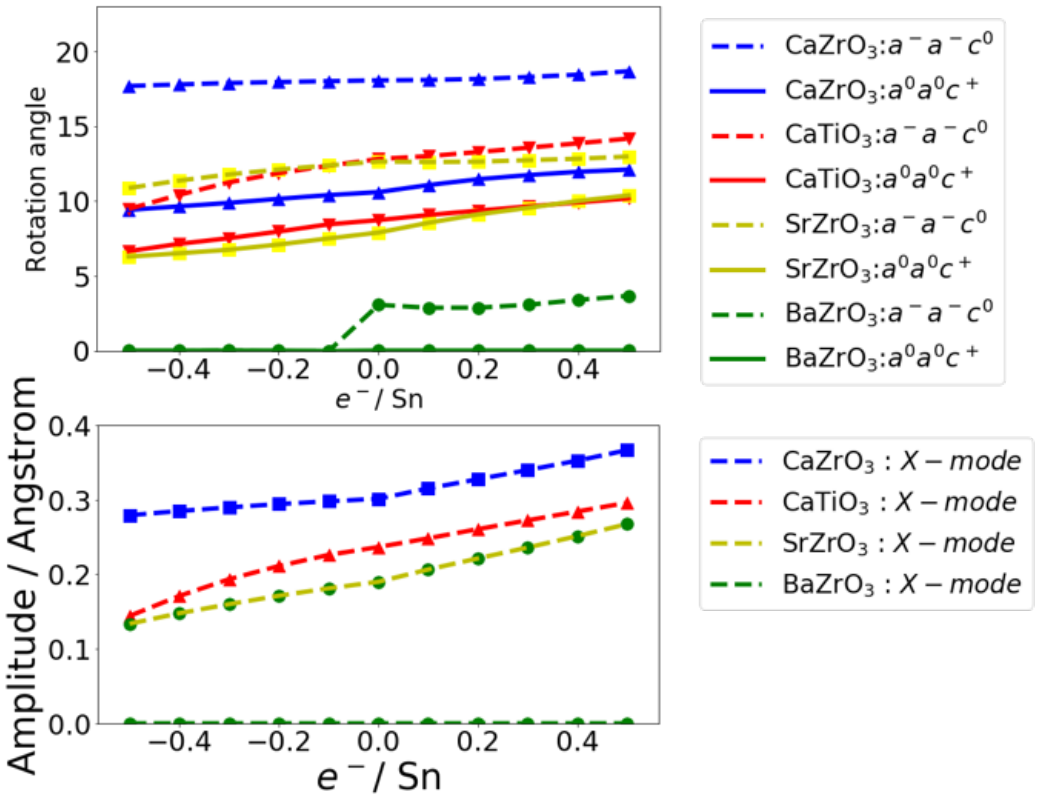


Figure 3.2: (a) The rotation angles of octahedral rotation modes and (b) the anti-polar mode amplitude increase with increasing electron doping in Zr- and Ti- based perovskites.

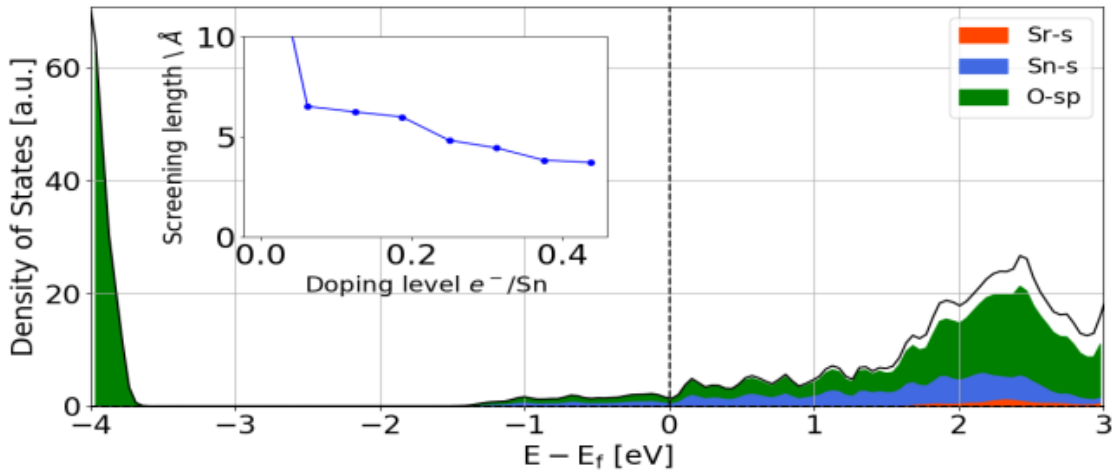


Figure 3.3: The projected density of states of $SrSnO_3$ when $0.3e^-$ per Sn atom doped. The inset is the screening length as a function of the doping level. The screening length is calculated using Thomas-Fermi model: $\lambda = \sqrt{\varepsilon/e^2 D(E_f)}$, here the $\varepsilon$ is the dielectric constant of undoped $SrSnO_3$.

## 3.3 Landau energy analysis

As we discussed in the last section, the major geometric effects of free electrons can be attributed to the increment of incompatibility (tolerance factor). However, the volume effect caused by free electrons cannot be ignored here. For the prior effect, we can have a more quantitative discussion here. When free electrons are introduced to the system, the structure expands naturally, and the majority of electrons move into the oxygen and Sn-5s orbitals and increase their ionic radii. (See the DOS in Fig. 3.3.) This increase can be seen in the derivatives of the tolerance factor with respect to the ionic radii:

$$t = \frac{R_A + R_O}{\sqrt{2}\,(R_B + R_O)} \tag{3.3}$$

$$\frac{dt}{dR_B} = -\frac{R_A + R_O}{\sqrt{2}\,(R_B + R_O)^2} \tag{3.4}$$

$$\frac{dt}{dR_O} = \frac{R_B - R_A}{\sqrt{2}\,(R_B + R_O)^2} \tag{3.5}$$

An increase in the ionic radius of the B cation necessarily reduces the tolerance factor, and the same applies to the ionic radius of Oxygen as long as $R_B - R_A < 0$, which is the case in practically all perovskites. This result implies that in all oxide perovskties where the density of states near the fermi level does not have any contribution from the A-site cation, the effect of electron doping is an effective reduction in the tolerance factor.

The evidence for increment of incompatibility is clear here, but it is unknown how the volume effect plays a role here. The phonon calculations show that, overall the anti-polar modes get strengthened along with the rotation modes in the Sn based compounds (shown in the figure 3.1). In order to disentangle the volume expansion effect, we performed DFT

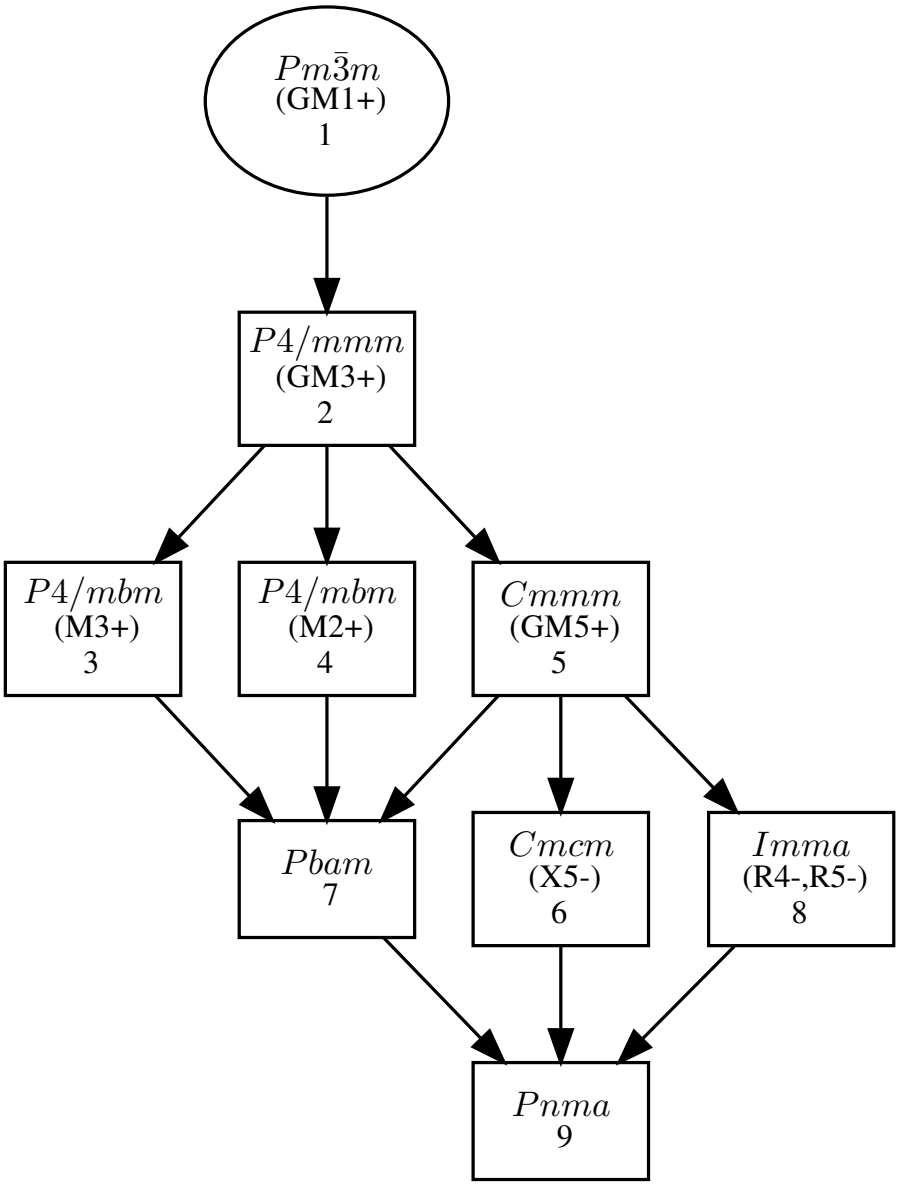


Figure 3.4: The space groups and distortion modes associated with the phase transition from $Pm\bar{3}m$ to $Pnma$ . This graph is made through Subgroups from Bilbao Crystallographic Server[3].

calculations in three different configurations: 1) In the first set of calculations, we kept the volume fixed to that of the undoped cubic reference structure. 2) We then repeated the calculations where we relaxed the volume of the cubic cell at each different doping level. 3) For control, we also performed calculations where we used the volumes from step 2, but did not consider any electron doping. (This last step shows the effect of volume expansion only. A phenomenological model is built from Landau theory and energies from DFT calculations. A more complete Landau energy expression (including up to 4-th order terms) that describes the transition from $Pm\bar{3}m$ to $Pnma$ phase is:

$$\mathcal{F} = \alpha_R R^2 + \beta_R R^4 + \alpha_M M^2 + \beta_M M^4 + \alpha_X X^2 + \beta_X X^4 + \gamma R \cdot M \cdot X \tag{3.6}$$

Here the $R$ represents the amplitude of distortion mode $R_5^-(a, a, 0)$, $M$ represents the amplitude of mode $M_2^+(0, 0, a)$, and $X$ represents that of $X_5^-$. These three distortion modes have the greatest amplitudes in the $Pnma$ phase, and the $R$ and $M$ modes are the primary order parameters, but multiple other modes are also present in the $Pnma$ structure as secondary order parameters, as shown in fig. 3.4.

We calculate the coefficients in the equation. 3.6 by fitting the energy when the structures manually distorted by different amplitudes of normal modes. 10 different amplitudes for distortion modes $R_5^-(a, a, 0), M_2^+(0, 0, a), X_5^-$ are applied in this process, thus $10 \times 10 \times 10 = 1000$ energies were used to fit each set of coefficients. Fig. 3.5 shows the change of coefficients as a function of doping level, each data point represents a fitting result from 1000 different structures. $3 \times 5 \times 1000 = 15000$ different structures were used and calculated to get fig. 3.5.

The volume expansion caused by the introduction of free electrons influences the rotation

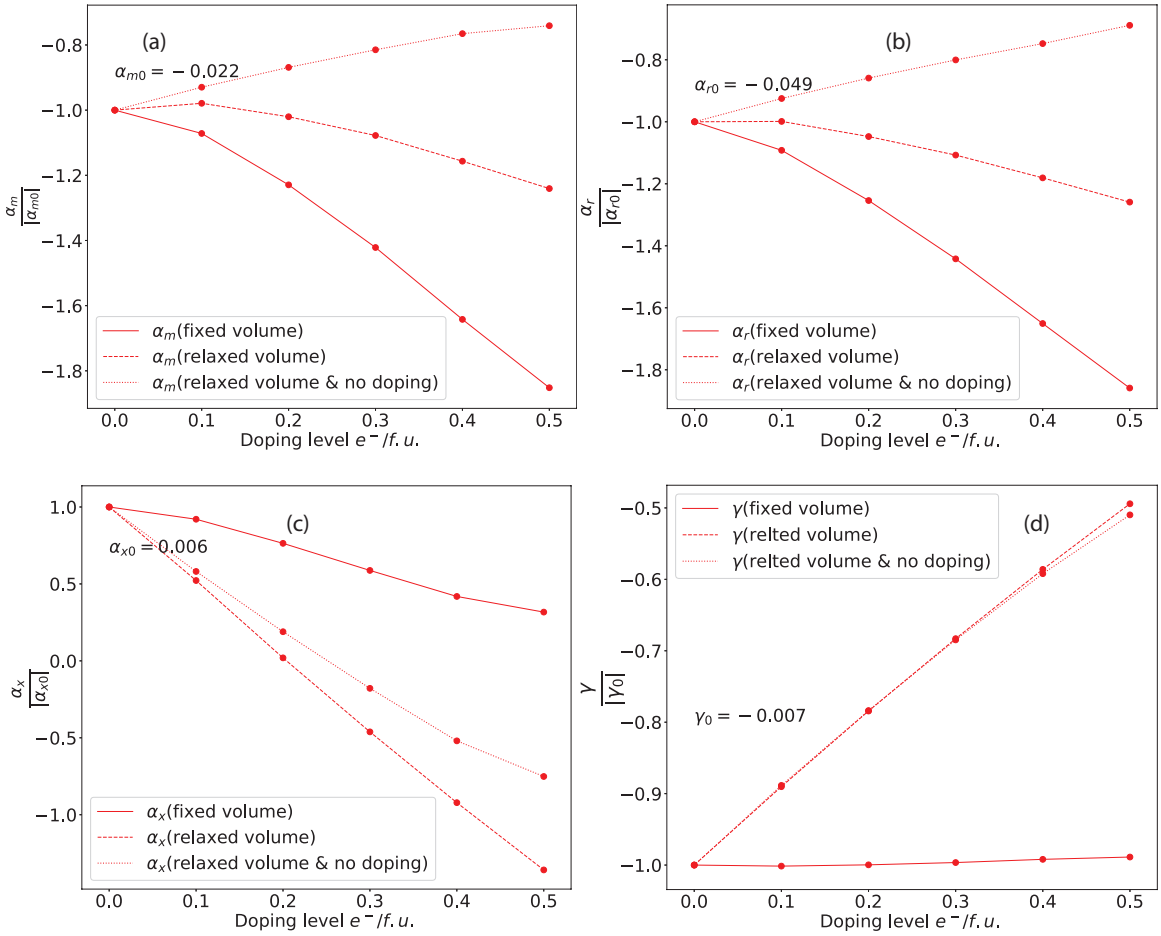


Figure 3.5: The coefficients of the Landau free energy expansion of $SrSnO_3$ (Eq. 3.2). When extra electrons are introduced, all rotation modes get softened while the trilinear coupling term remains a positive constant. Three different configurations are shown here, solid: relaxed the atomic position with fixed lattice constant when not doping, coarse dashed: relaxed both atomic positions and lattice constant when doping, fine dashed: relax the atomic positions using the lattice constant when doping, but no free charge carriers are present. Unit of $\alpha$ is $eV/\text{Å}^2$, unit of $\gamma$ is $eV/\text{Å}^3$.

amplitude, but it is not the dominant factor. It is the change in the tolerance factor that dominates the trends. This can be seen from the trends of the (fixed volume) and dashed (relaxed volume) lines in Fig.3.5a-c. The coefficients of quadratic energetic terms both increase with or without volume changed. The volume change by itself (dotted lines) leads to an opposite trend for $\alpha_M$ and $\alpha_R$. The only exception where relaxing the volume makes a qualitative difference is in the trilinear coupling $\gamma$: This coefficient is almost independent of the free carrier concentration, but reduces rapidly when volume expansion is taken into account.

Compared with the rotational modes, the anti-polar mode is more sensitive to the volume effect but less sensitive to charge doping. The anti-polar mode have a positive phonon frequency and quadratic energy contribution at the undoped state. The sign of phonon frequency and quadratic energy term changes when the volume expands - this will hugely increase the amplitue of anti-polar mode. The trilinear coupling is also very sensitive to the volume effect despite the sign remaining unchanged. Interestingly, once the volume is fixed, it is almost independent of the doping level.

In order to estimate the effect of secondary order parameters $M_2^+$ and $R_5^-$ modes, we also performed a separate set of calculations where we considered nonzero amplitudes of these modes as well. Since considering all different values of these modes' amplitudes would make the calculations prohibitive, we fixed the $\frac{|M_2^+|}{|M_3^+|} = 0.5$ and $\frac{|R_4^-|}{|R_5^-|} = 0.5$, and then re-fitted the coefficients of the Landau model. These ratios are determined by their value in the undoped-ground state structure. Trends that are qualitatively very similar to those in Fig. 3.5 were found.

In Fig. 3.6, we show the change of the $4^{th}$ order terms' coefficients in the free energy

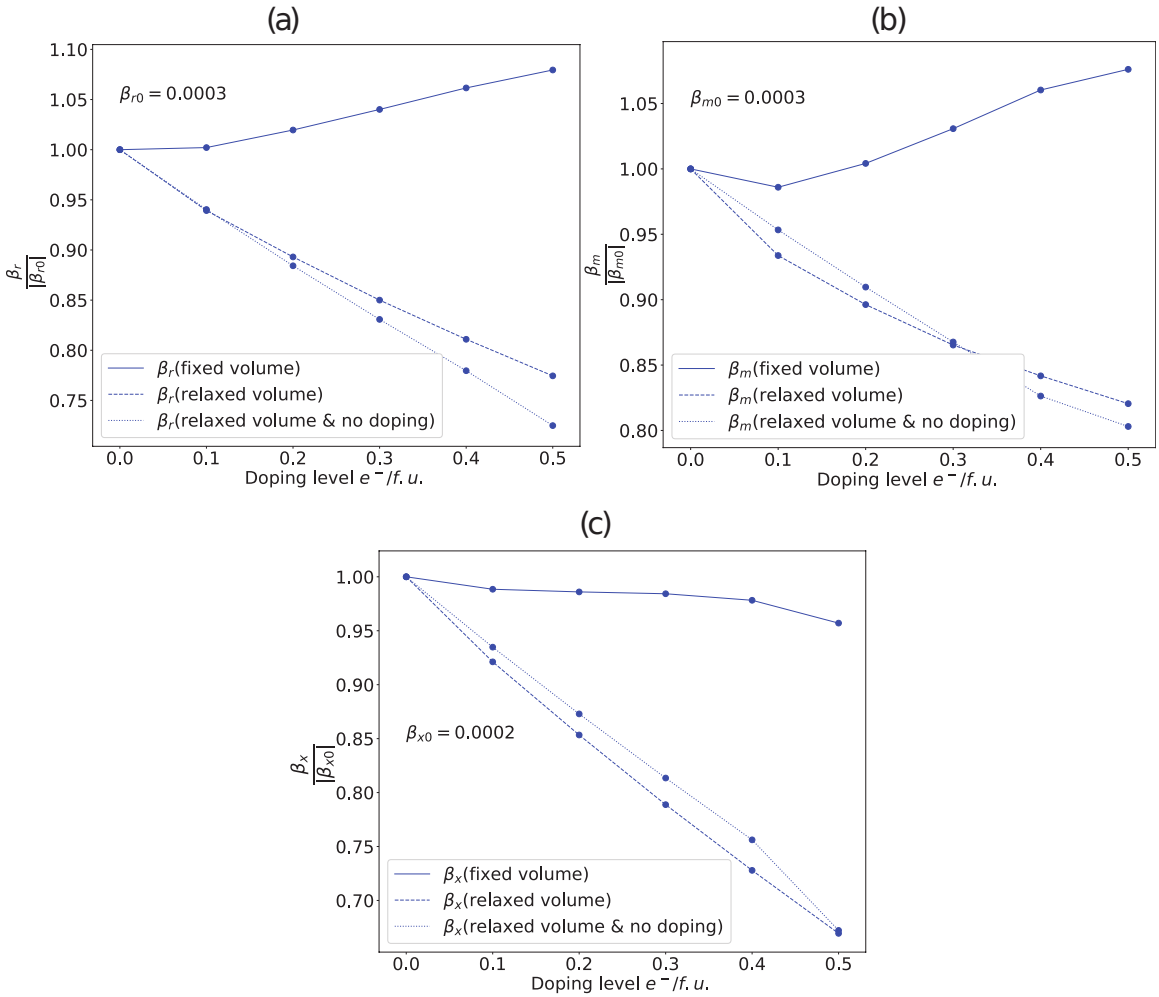


Figure 3.6: The 4th-order terms' coefficients in landau free energy expansion of $SrSnO_3$. Unit of $\beta$ is $eV/\text{Å}^4$.

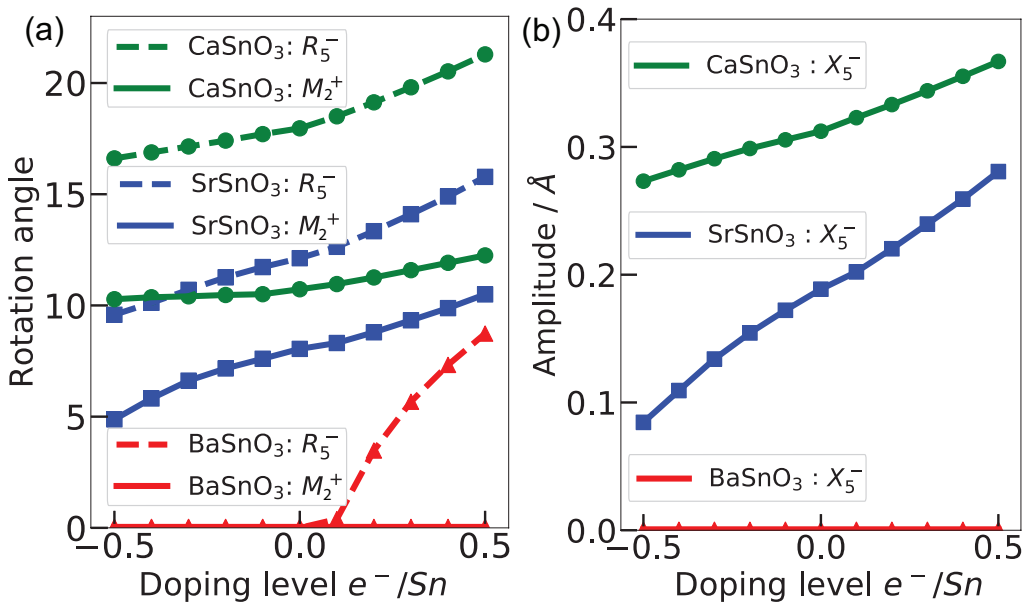


Figure 3.7: Results of DFT structure optimizations under fixed volume. Both (a) the octahedral rotation angles (b) the anti-polar mode amplitudes increase with increasing number of electrons, as expected from the phonon frequencies in Fig. 3.1(d).

expansion. These coefficients barely change (less than 10%) when the volume is fixed. Even when the volume is relaxed, the changes in 4th-order terms are less significant compared to the lower order coefficients' effects.

## 3.4 Electrostatic gating in Hybrid-Improper Ferroelectrics

We now move on to $A_3B_2O_7$ HIFs, and consider $Sr_3Sn_2O_7$ as an example. $Sr_3Sn_2O_7$ is an $n = 2$ RP compound, which can be considered as a layered perovskite with an extra SrO layer after every pair of $SrSnO_3$ bilayers. It is experimentally verified to be a ferroelectric[39,40], and its polarization is induced through the hybrid-improper mechanism which involves the trilinear coupling between the polar mode ($\Gamma_5^-$, which we denote as $P$) and two octahedral rotation modes ($X_3^-$ and $X_2^+$, which we denote as $Q_1$ and $Q_2$) shown in Fig. 3.8a.

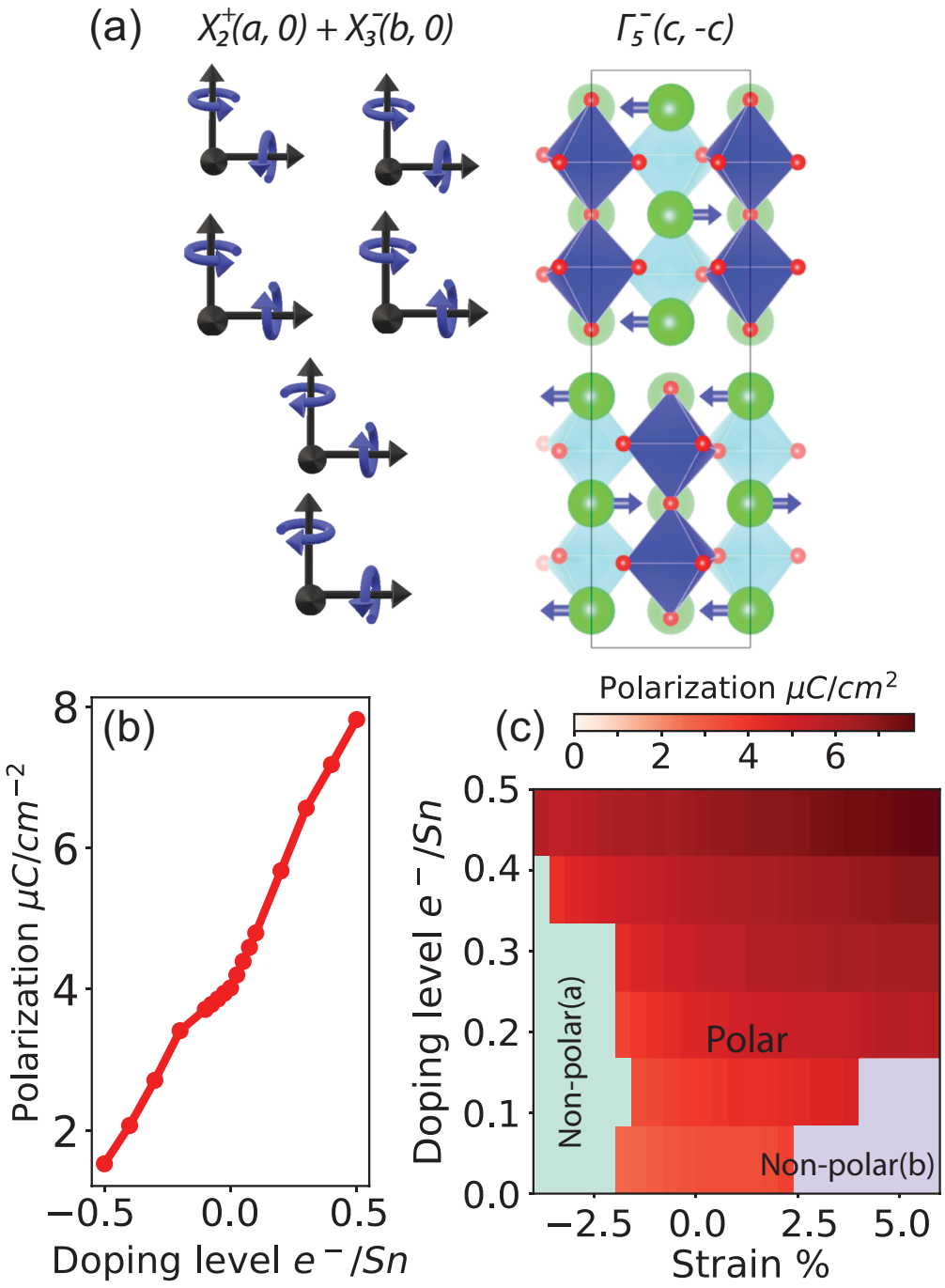


Figure 3.8: (a) The structure of $Sr_3Sn_2O_7$ includes three structural distortion modes with respect reference $I4/mmm$ structure: Two oxygen octahedral rotation modes ($X_2^+$ and $X_3^-$) and a polar mode ($\Gamma_5^-$). (b) The structural polarization strength of $Sr_3Sn_2O_7$ as a function of doping level. The structural polarization is as the sum of the products of the nominal charge and polar displacements of ions. (c) The doping – strain phase diagram of $Sr_3Sn_2O_7$. The non-polar(a) and non-polar(b) phases have $Aeaa$ and $P4_2/mnm$ space groups respectively (details of these phases can be found in Table. 2.1).

These modes are the counterparts of the antipolar A-site displacement $X_5^-$ mode, and the octahedral rotation modes $R_5^-$ and $M_2^+$ in bulk perovskites. Two crucial differences between the $A_3B_2O_7$ RP and the $ABO_3$ perovskite structures are (i) in the smaller Brillouin zone of the RP structure, both the octahedral rotation modes $Q_1$ and $Q_2$ have the same wavevector, and hence can couple to zone center modes at the trilinear order, and (ii) the out-of-phase A-site displacement is now a polar $\Gamma$ mode because the dipole moments induced by the symmetry inequivalent A-sites don't cancel. The shortest free energy that explains the polarization up to third order is

$$\mathcal{F} = \alpha_1 Q_1^2 + \alpha_2 Q_2^2 + \alpha_P P^2 + \gamma Q_1 Q_2 P \tag{3.7}$$

The trilinear coupling $\gamma$ between the unstable $Q_1$ and $Q_2$ rotations with $\alpha_{1,2} < 0$ and the stable polar mode $P$ with $\alpha_P > 0$ gives rise to a nonzero polarization $P = \gamma Q_1 Q_2 / 2\alpha_P$ in the groundstate.

In order to elucidate the change in the structural polarization in $Sr_3Sn_2O_7$ when free carriers are introduced, we optimize the crystal structure again with different numbers of added electrons or holes. The results in Fig. 3.8b show that added electrons increase the polarization, similar to the increased antipolar $X$ mode amplitude in $SrSnO_3$. This can be explained by the fact that the mechanism that leads to enhancement of octahedral rotations in the electron doped $SrSnO_3$ is essentially a local mechanism that also applies to $Sr_3Sn_2O_7$, which also has a similar DOS with Sn-s bands on the conduction band. Filling the conduction band increases the effective ionic radius of the Sn ions, which in turn increases the amplitude of $Q_1$ and $Q_2$ octahedral rotations, and hence enhance the polarization $P$.

In the HIF $Ca_3Ru_2O_7$ or the proper geometric ferroelectric-like $LiOsO_3$, the polarization is persistent against free carriers because of the absence of significant coupling between the electronic states near the Fermi level and the unstable phonons[122,141]. In $Sr_3Sn_2O_7$, there is a strong effect of the conduction band occupation on the lattice instabilities, which is not reported in these other metallic ferroelectric-like compounds.

The enhanced rotations also expand the biaxial strain range where $Sr_3Sn_2O_7$ is structurally polar. In Fig. 3.8c, we show the strain – doping phase diagram of $Sr_3Sn_2O_7$, calculated by fixing the in-plane lattice parameters and relaxing the out-of-plane one to simulate the boundary conditions on a thin film lattice matched to a substrate. Insulating, undoped $Sr_3Sn_2O_7$ is known to undergo a transition to a non-polar phase above $\sim \mp 2\%$ biaxial strain[34] like many other compounds[55]. Fig. 3.8c shows that not only doping enhances polarization at fixed volume, but it also stabilizes the polar phase at wider strain ranges. The polar/non-polar transition induced by epitaxial strain is driven by the disappearance of one of two rotation modes in the polar phase[142]. The free electrons increase the stability of both rotation modes which make this phase transition occur at a higher strain value.

The volume effect is also investigated in the RP-phase perovskites as shown in the figure 3.9. Though the polarization strength is less enhanced when the volume is fixed, the overall trend is similar. The enhancement of polarization caused by volume expansion is far less significant than the enhancement caused by increment of octahedral rotation.

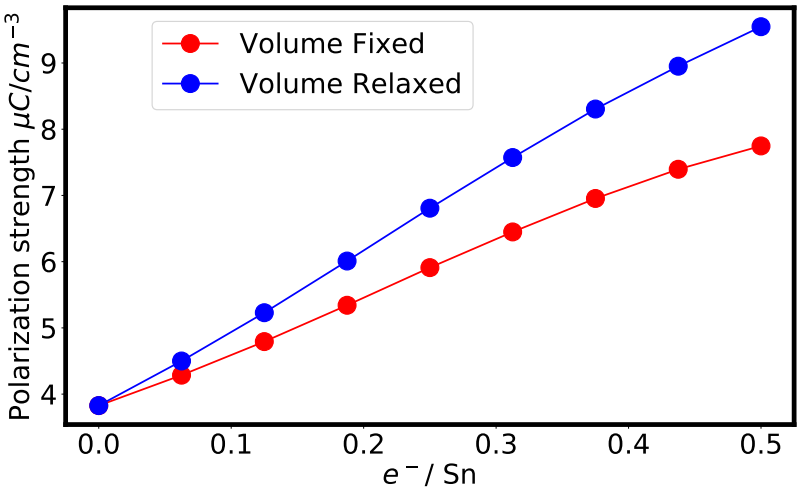


Figure 3.9: The polarization of $Sr_3Sn_2O_7$ compounds as a function of doping level, with and without the volume fixed. It can be seen that the polarization even increase faster when the volume is relaxed.

## 3.5 Ferroelectric-like transition induced by free electrons

The strong effect of free electrons on stabilizing a metallic ferroelectric-like phase in $Sr_3Sn_2O_7$ leads to the question *whether it is possible to drive a centrosymmetric compound to a polar phase by doping it with free electrons* without the help of biaxial strain. We scanned a number of $A_3B_2O_7$ oxides, but could not find an example that undergoes a polar phase transition for dopings up to 0.5 $e^-$ per B site cation, which is already beyond what is experimentally achievable via methods such as electrostatic gating. In order to *design* a material which is closer to a structural phase transition than $Sr_3Sn_2O_7$, we turn to *targeted chemical pressure*, which involves selectively substituting part of Sr ions with larger Ba cations[143]. While it is not always possible to order same charge cations in bulk, molecular beam epitaxy has been successfully used to obtain targeted chemical pressure in other RP phases $(SrTiO_3)_n(BaTiO_3)_mSrO$[143]. In $Sr_3Sn_2O_7$ ceramics, up to 10% of Ba ions are reported to preferentially substitute inequivalent Sr sites, however, the ordering tendencies depend

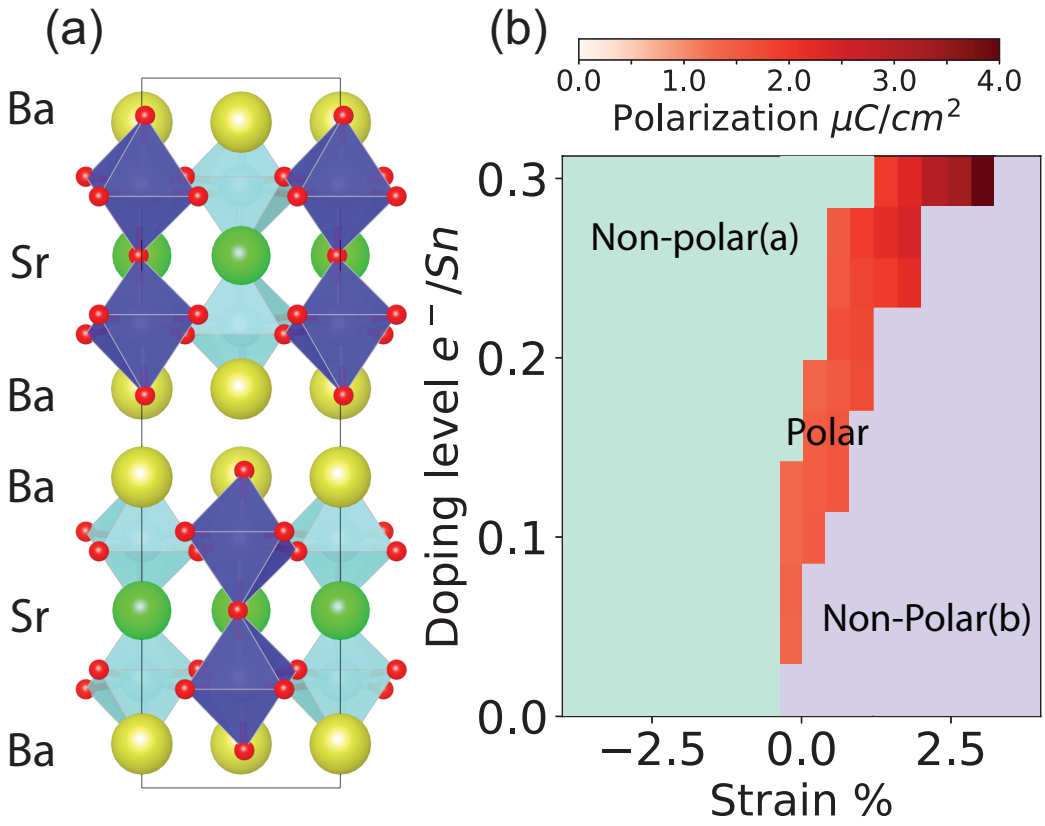


Figure 3.10: (a) The structure and (b) a doping-strain phase diagram of $Ba_2SrSn_2O_7$. Yellow spheres represent Ba atoms. The non-polar(a) and non-polar(b) phases have *Aeaa* and $P4_2/mnm$ symmetries respectively.

sensitively on changes in the substitution amount[129]. We consider a structure where the 2/3 of Sr cations are substituted with Ba to form $Ba_2SrSn_2O_7$, where the Ba cations are on the double-rocksalt layers of the RP structure, as shown in Fig. 3.10a. While this structure may not be energetically the most stable one, it may in principle be synthesized via layer-by-layer growth. The lowest energy structure of $Ba_2SrSn_2O_7$ is centrosymmetric when undoped and strain-relaxed, but introducing electrons to the conduction band leads to a transition to a polar structure with space group $Cmc2_1$ (Fig. 3.10b). Thus, $Ba_2SrSn_2O_7$ is a free carrier induced 'metallic ferroelectric'. Like in undoped $A_3B_2O_7$ compounds, biaxial strain also modifies the stability range of the polar phase of $Ba_2SrSn_2O_7$.

Experimental verification of this prediction is possible. $Ba_3Sn_2O_7$ is stable in bulk[144], and thin films of both Sr and Ba stannate perovskites were grown by multiple groups[52,145,146]. If the free charge is constrained in the top ∼10 Å of a $Ba_2SrSn_2O_7$ film, the charge density needed to stabilize the polar phase is $\sim 5 \cdot 10^{13}$ cm$^{-2}$. Dielectric based gating allow densities of $\sim 10^{13}$ cm$^{-2}$[147], and it is possible to obtain densities exceeding $\sim 10^{14}$ cm$^{-2}$ via ionic liquid gating[137,148,149]. Thus, it is possible to induce in-plane structural polarization electrolyte gating. The polarization can be observed by second harmonic generation as was done in $LiOsO_3$[150].

## 3.6 Other $A_3B_2O_7$ compounds

This mechanism is very general, and it could be expected to be applicable to many other HIF oxides. However, our calculations on $Ca_3Ti_2O_7$ and $Sr_3Zr_2O_7$ (plotted in the figure 3.11) indicate that this is not the case. Even though the parent $CaTiO_3$ and $SrZrO_3$ compounds behave very similarly to $SrSnO_3$ under doping, the structural polarization of both $Ca_3Ti_2O_7$ and $Sr_3Zr_2O_7$ decrease upon electron doping. The reason is a subtle difference in the nature of polarization in these compounds: While both $Ca_3Ti_2O_7$ and $Sr_3Zr_2O_7$ have HIF groundstates, in their $I4/mmm$ reference structure they also display weak polar Γ point instabilities[41,151]. As a result of this instability, $Ca_3Ti_2O_7$ has a significant Ti contribution to polarization. This contribution is reduced as electrons are introduced to the system, because free carriers suppress the Ti–O hybridization and harden this soft mode in $Ca_3Ti_2O_7$ as they do in titanate perovskites $CaTiO_3$ or $BaTiO_3$[101,102]. $Sr_3Sn_2O_7$, on the other hand, has no Γ instabilities, and has only a negligible $SnO_2$ layer polarization. This suggests the

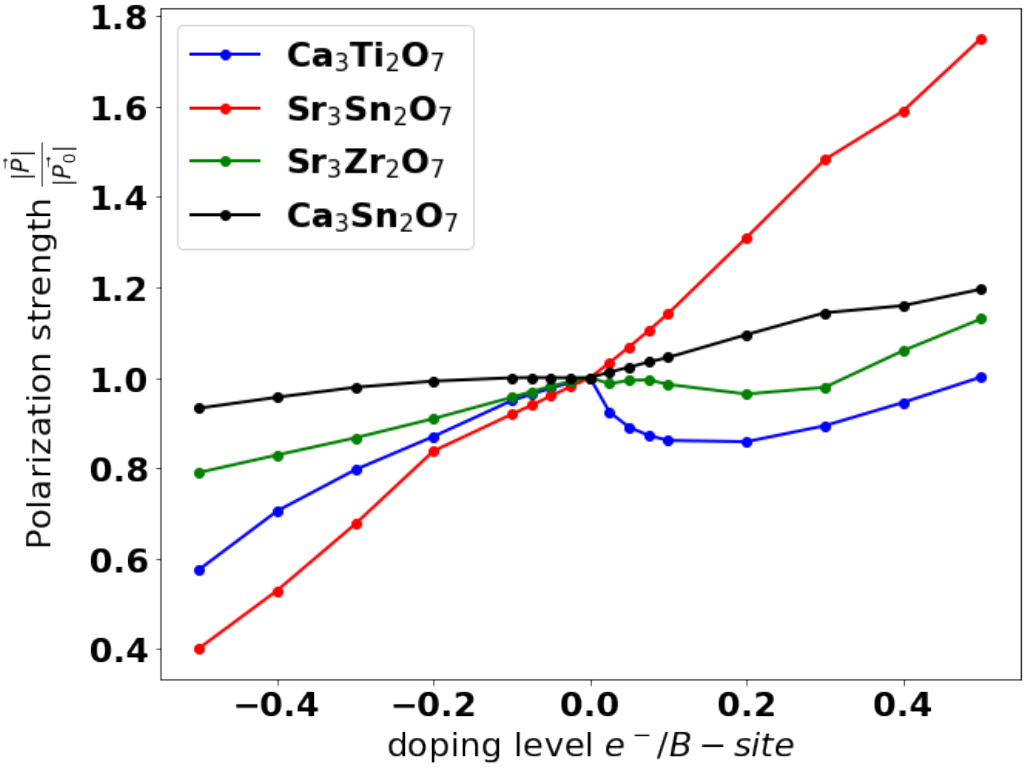


Figure 3.11: Charge carrier doping will change the structural properties. The net polarization of four different RP-phase perovskites under doping.

stannate perovskites as a unique group of compounds that can display free carrier enhanced (or induced) hybrid improper ferroelectricity.

Our phonon calculations at Γ-point over $Ca_3Ti_2O_7$ and $Sr_3Sn_2O_7$ also help verify this explanation: The character of the unstable mode in undoped $Ca_3Ti_2O_7$, which we refer to

| | $Sr_3Sn_2O_7$ | $Ca_3Ti_2O_7$ |
|---|---|---|
| $\Gamma_5^-$ mode-A | 93.91 $cm^{-1}$ | **-61.71** $cm^{-1}$ |
| $\Gamma_5^-$ mode-B | 69.87 $cm^{-1}$ | 75.05 $cm^{-1}$ |

Table 3.2: The phonon frequencies of polar displacement modes shown in Fig. 3.12 in undoped $Sr_3Sn_2O_7$ and $Ca_3Ti_2O_7$.

as 'mode-A', is not surprising, and it is similar to the polar mode in $CaTiO_3$: It consists of significant and parallel Ca displacements, that are accompanied with Ti displacements (Fig. 3.12). The next lowest frequency polar mode in $Ca_3Ti_2O_7$, which we refer to as 'mode-B' has a different character: It has significant anti-parallel Ca displacements, with minimal Ti displacement.

As a result of these anti-parallel A-site displacements, mode-B is expected to couple more strongly with the octahedral rotations at the trilinear order. As a result, the polar ground state structure of $Ca_3Ti_2O_7$ has significant contributions from both of these polar modes, which can be seen from the large contribution from both $TiO_2$ and CaO layers to the total polarization (Fig. 3.13). In $Sr_3Sn_2O_7$, on the other hand, mode-B is softer than mode-A, and as a result, there is almost no contribution from the SnO layers to the polarization as shown in Fig. 3.13. This difference is responsible of the different trends in polarization of these compounds under doping: While the AO layers' contributions to the polarization in both compounds increase under electron doping, the $TiO_2$ contribution from Mode A is suppressed by the introduced electrons. This is expected, since added electrons

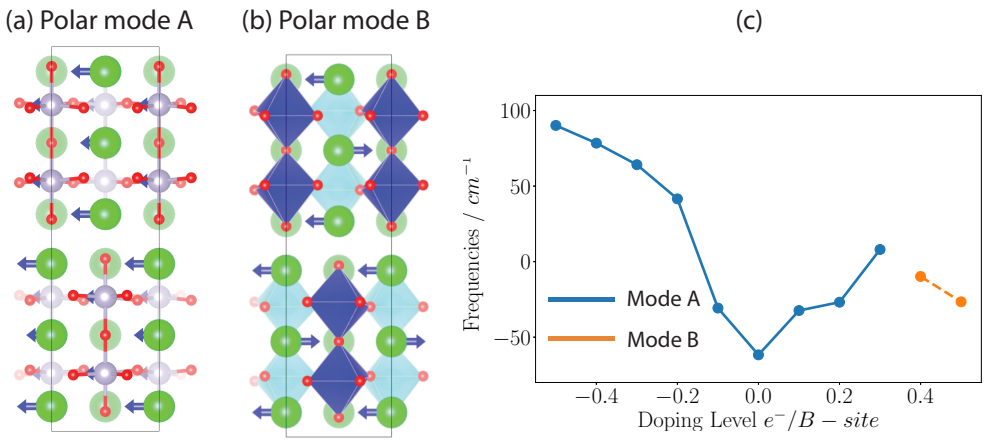


Figure 3.12: In the undoped $Ca_3Ti_2O_7$, there are two origins of the polarization: (a) The proper ferroelectric mode and (b) hybrid improper ferroelectric mode that coupled with rotation modes. (c) The frequency of the polar mode (schematic on the left) in $Ca_3Ti_2O_7$ change rapidly under charge carriers doping. Note that especially for large electron doping the characters of these modes mix, and we classified them as mode-A or mode-B according to the direction of the inner vs. vacuum AO layers' displacements being parallel or antiparallel.

to the Ti d orbitals are well known to suppress Ti–O hybridization and harden polar soft modes[102]. The frequency of the unstable phonon mode in tetragonal $Ca_3Ti_2O_7$ supports this picture: It is hardened under both electron and hole doping. Under large ($\gtrsim 0.3$) electron concentration the polar mode softens with increasing concentration again. This is due to mode-B softening and mixing with mode-A to make the instability domininantly like mode-B at larger dopings, which explains the upturn in polarization in this doping range.

## 3.7 Discussion

Using first principles calculations and studying the oxygen octahedral rotations in *Pnma* perovskites under doping, we showed that the structural polarization in stannate HIFs is not only robust against free carriers, but it is also enhanced. We furthermore predicted a yet-to-be-synthesized compound $Ba_2SrSn_2O_7$ that undergoes a centrosymmetric to polar transition

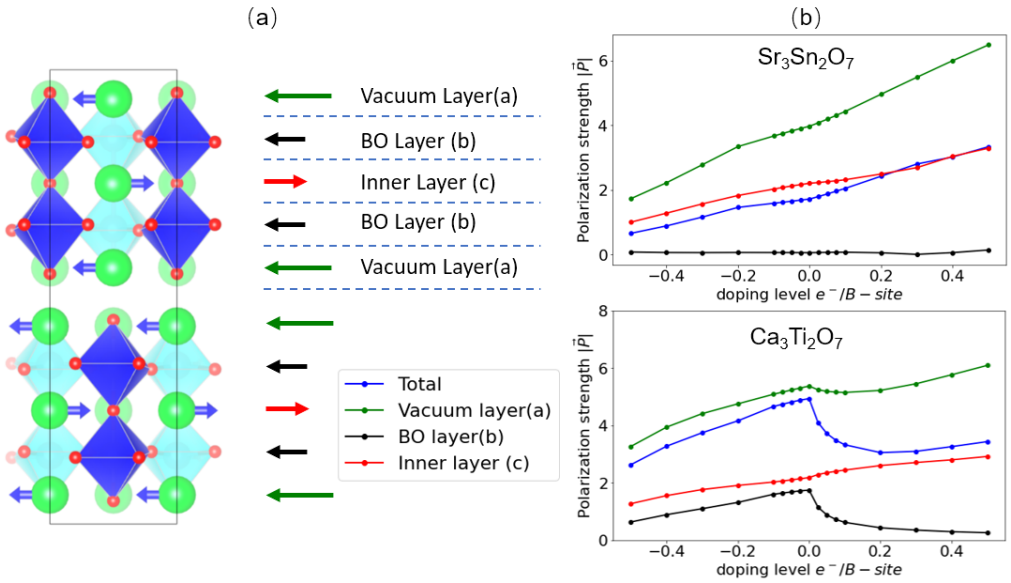


Figure 3.13: (a) The polarization direction of each layer alternates in HIF $A_3B_2O_7$ perovskites. The AO rock-salt like layer is noted as vacuum layer, while the other AO layer in the middle of perovskite layer is called inner layer. (b) The polarization strength by layer for $Sr_3Sn_2O_7$ (top) and $Ca_3Ti_2O_7$ decomposed by layers.

under electron concentrations that are experimentally achievable by ionic liquid/gel gating. While our calculations are strictly at zero temperature and finding temperature dependence of lattice distortions requires molecular dynamics or effective Hamiltonian studies, the large energy gains we find suggest the possibility of observing this effect even at room temperature. Our results show that the improper ferroelectricity driven by steric lattice instabilities can serve as a means to obtain carrier induced ferroelectricity in compounds where those instabilities are strengthened by the free carriers.

# Chapter 4

# Chemical bonding and Born charge in 1T-$HfS_2$

This chapter is adapted from my collaborated work *Chemical bonding and Born charge in 1T-$HfS_2$* [152]. In this work, the Raman and infrared spectrum part is performed by Sabine N. Neal and Janice L. Musfeldt. The theoretical analysis and first-principles calculation is performed by myself.

The first-principles calculation indicates the Born effective charge in 1T-$HfS_2$ is much larger than that in other transition metal dichalcogenides(TMD). Experimentally, results from the infrared absorption and Raman scattering spectroscopies also confirm our finding: The LO-TO splitting of the $E_u$ vibrational mode is measured and it shows that $Z^*_{\mathrm{B}} = 5.3e$. As a comparison, the first-principles method gives a result of $Z^*_{\mathrm{B}} = 6.4e$. Polar displacement-induced charge transfer from sulfur $p$ to hafnium $d$ is responsible for the enhanced Born charge compared to the nominal 4+ in hafnium. As a comparison, the Born effective charge

of Mo in 2H-$MoS_2$ is only 1.1 - 1.2$e$ in the in-plane direction[153]. In order to understand how $Z^*_B$ relates to the nominal 4+ charge of the Hf center, we decompose the theoretical Born effective charge into band-by-band contributions and find that polar displacement-induced charge transfer from sulfur $p$ to hafnium $d$ orbitals is responsible for the enhanced Born charge. 1T-$HfS_2$ is thus an ionic crystal with strong and dynamic covalent effects.

## 4.1 Background

While 3$d$ transition metal oxides and chalcogenides display strong electronic correlations, narrow band widths, and robust magnetism, 4 and 5$d$ systems are recognized for strong spin–orbit coupling, increased hybridization, and more diffuse orbitals. As a result, materials that contain 4- and 5$d$ centers often have enhanced or emergent properties[154–162]. Transition metal dichalcogenides such as $MoTe_2$, $IrTe_2$, $HfSe_2$, and $PtSe_2$ are of great interest for their unconventional chemical bonding and hybridization, topology, multiferroicity, and tendency toward complex dimerization patterns[163–170]. Within this class of materials, 1T-$HfS_2$ has attracted particular attention as an analog of $HfO_2$ - a highly polarizable gate dielectric[171,172].

1T-$HfS_2$ is a layered material with a $P\bar{3}m1$ (#164) space group at 300 K[173]. Each $Hf^{4+}$ ion has $D_{3d}$ site symmetry and is located at the center of a $S^{2-}$ octahedron. The van der Waals gap is 3.69 Å, and the sheet thickness is 2.89 Å. Photoemission studies reveal an indirect band gap of 2.85 $eV$ between Γ and M/L, which varies slightly from the ≈ 2 $eV$ optical gap[174]. 1T-$HfS_2$ forms a high performance transistor with excellent current saturation[175]. The carrier mobility is on the order of 1800 $cm^2V^{-1}s^{-1}$ - much higher than

$MoS_2$ and thickness dependent as well[176,177]. Group theory predicts that at the Γ point 1T-$HfS_2$ has vibrational modes with symmetries of $A_{1g} + E_g + A_{2u} + E_u$. The $A_{1g} + E_g$ modes are Raman-active, and the $A_{2u} + E_u$ modes are infrared-active[173,178]. Despite many years of work, there are a surprising number of unresolved questions about 1T-$HfS_2$ - even in single crystal form. In the field of vibrational spectroscopy, there is controversy about mode assignments, the role of resonance in creating hybrid modes, the presence or absence of surface phonons, and the use of this data to reveal the Born effective charge ($Z^*_B$). As an example, Born effective charges between $3.46e$ and $5.5e$ have been reported by various experimental[179,180] and theoretical[181] groups. Evidence for the degree of ionicity (or covalency) is both interesting and important because $5d$ orbitals tend to be more diffuse than those of their $3d$ counterparts. Within this picture, 1T-$HfS_2$ has the potential to sport significant covalency. High pressure Raman scattering spectroscopy reveals a first-order phase transition near 11 GPa and different $\partial\omega/\partial P$'s (and thus mode Gruneisen parameters) for the hybrid $E_u$ and fundamental $A_{1g}$ modes[182]. At the same time, variable temperature Raman scattering spectroscopy shows a systematic blueshift of the spectral features down to 100 K, except for the large $A_{1g}$ mode near 330 $cm^{-1}$ which redshifts[177,182]. In few- and single-layer form, 1T-$HfS_2$ is suitable for high-performance transistors[175,183,184], displays a direct gap (rather than indirect as in the bulk)[185], exhibits photocatalytic behavior appropriate for water splitting[186], reveals applications in photodetection[187], is susceptible to strain effects[188], and is useful in N, C, and P surface adsorption[189]. This system can be integrated into van der Waals heterostructures and grown vertically as well[184,190,191].

## 4.2 Methods

First principles calculations were performed using the projector augmented wave approach as implemented in the Vienna Ab-initio Simulation Package (VASP)[58,192,193]. Both the Born effective charges and the high frequency dielectric constant are determined from the response to finite electric fields. The high-frequency dielectric constant $\epsilon(\infty)$, which only contains the electronic contribution, is obtained by differentiating the polarization with respect to the external electric field with clamped ions:

$$\epsilon_{ij}^{\infty} = \delta_{ij} + \frac{4\pi}{\epsilon_0}\frac{\partial P_i}{\partial \mathcal{E}_j}, \tag{4.1}$$

where the polarization is calculated using the implementation of the the Perturbation Expression After Discretization (PEAD) approach in the VASP package[194,195]. Electric fields of 2 meV/Å, 2 meV/Å, and 10 meV/Å are applied separately along $a$, $b$, and $c$ axes to calculate the derivatives. Similarly, the Born effective charge is calculated through the derivatives of the polarization with respect to the ionic displacements. At this step, using the Hellman-Feynman forces enables the use of the more computationally efficient formula

$$Z_{ij}^{*} = \frac{\Omega}{e}\frac{\partial P_i}{\partial u_j} = \frac{1}{e}\frac{\partial^2 \mathcal{F}}{\partial u_j \partial \mathcal{E}_i} = \frac{1}{e}\frac{\partial F_j}{\partial \mathcal{E}_i}. \tag{4.2}$$

Here $\mathcal{F}$ is the electric enthalpy which is the sum of the Kohn-Sham energy and the energy gain due to the interaction between the polarization and the external electric field: $\mathcal{F} = E_{KS} - \Omega \mathbf{P} \cdot \mathcal{E}$. The Hellman-Feynman force $F$ is given by $F_i = \frac{\partial \mathcal{F}}{\partial u_i}$. $F$ solely depends on the ground state wavefunction, and hence is easier to calculate than the polarization.

As a reliability check, density functional perturbation theory (DFPT)[196] combined with multiple functionals (including PBEsol[60] and revised-TPSS meta-GGA[197]) with spin-coupling is also performed to get the Born effective charge. Both approaches provide similar results for the dielectric constant and Born effective charge. We chose the latter method for its compatibility with Hatree-Fock method, and as a result, the hybrid functionals.

All the first-principles calculations are performed in the primitive 3 atom unit cell with a $12 \times 12 \times 6$ k-point grid and cut-off energy of 500 eV. The lattice constants and vectors are taken from the experimental literature, but the internal coordinates of the S ions are obtained through structural optimization of forces. The energy tolerance for self-consistency is set to $10^{-8}$ to get a well-converged wavefunction. To reproduce the experimental bandgap more closely, HSE hybrid functional is employed[198]. In the case of 1T-$HfS_2$, a energy band gap of 2.05 eV can be achieved by using the screening parameter of 0.2, which is the so-called HSE06 approximation. Reports of the band gap of $HfS_2$ span values from 1.96 eV (from optical absorption)[199] to 2.85 eV (from combined angle-resolved and inverse photoemission)[174]. Note that band structures calculated using PBEsol or meta-GGA functionals both underestimate the band gap by at least a factor of two, which influences the prediction accuracy of electric field response. Since Hf is a heavy element with strong spin-orbital coupling (SOC)[200], DFT calculations that take SOC into account were also performed, but no significant change of Born effective charges and phonon frequencies are observed.

To further explain the origin of Born effective charge, we employed the maximum localized Wannier function (MLWF)[201,202] to predict the band-by-band contribution. The Wannier90 software package is used for this analysis[203].

## 4.3 Lattice dynamics in 1T-$HfS_2$

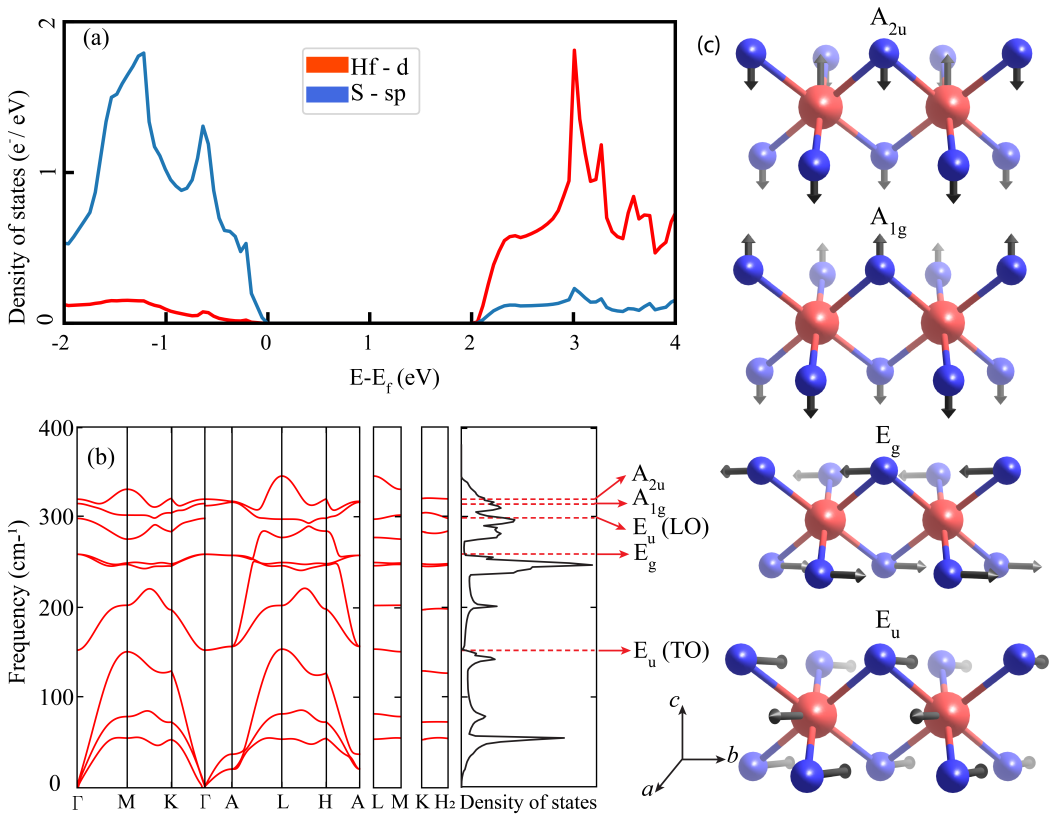


Figure 4.1: (a) The electronic density of states of 1T-$HfS_2$. Different colors indicate different orbitals of the two types of atoms. (b) The phonon spectrum of 1T-$HfS_2$ and its density of states. The Γ-point phonon mode frequencies are marked with dashed lines. (c) Displacement patterns of several Γ-point phonon modes. Blue atoms are S and the red atoms are Hf. The arrows are not scaled to real displacement amplitudes.

Figure 4.1 displays the projected density of states of 1T-$HfS_2$ computed using density functional theory and atom centered local projectors[58]. The bands can be assigned Hf and S character easily, and the degree of hybridization between the atoms is not dominant (albeit nonzero). This reveals the strong ionic nature of this system: The valence band is composed mainly of S-$p$ orbitals whereas the conduction band is predominantly Hf-$d$ in character. We find a band gap of 2.05 $eV$ using the HSE06 functional. This is consistent

with the small electronegativity of the Hf (1.3 on the Pauling scale) compared to that of S (2.6 on the Pauling scale).

Despite the apparent ionicity of the density of states, the dynamical Born effective charges in 1T-$HfS_2$ are anomalous. We find an in-plane value for the Hf ions as $Z^*_{\mathrm{B},xx} = +6.4e$. By contrast, the out-of-plane value for Hf $Z^*_{\mathrm{B},zz}$ is only $2.0e$. This reveals that either (i) the Hf ions are strongly polarizable, or (ii) the small degree of covalency is strongly dependent on ionic displacements[204].

Figure 4.1(b) displays the phonon dispersions of 1T-$HfS_2$. While the spectrum is highly dispersive within the plane (for instance, in the Γ-M direction) it is much less so in the out-of-plane direction (for instance, along Γ-A). This difference is a natural consequence of the layered crystal structure and is the origin of the spikes in the phonon density of states [right panel, Fig. 1(b)]. One aspect of these predictions that will be important for later discussion is the mode order around the $A_{1g}$ fundamental. Notice that the $E_u$ feature is predicted to be below the $A_{1g}$ mode, whereas the $A_{2u}$ mode is predicted to be above the $A_{1g}$ fundamental. These features are labeled in Figure 4.1(b). Theoretical phonon frequencies are in excellent agreement with our measured results Table 4.1.

Lattice dynamics can be used to gain information about the chemical bonding in crystals. In 1T-$HfS_2$, the $E_u$ optical mode is due to the in-plane vibrations of the Hf cations against the S anions [Figure 4.1(c)]. The frequency difference between the longitudinal and transverse optical modes (the LO-TO splitting) depends on the permittivity, as well as the dynamical charges of the ions. Formally, the LO-TO splitting stems from a non-analytic

| Theoretical | Symmetry | Infrared | Raman | Mode Displacement |
|---|---|---|---|---|
| 152 | $E_u$ $(TO)$ | 155 | 132 | in-plane, out-of-phase motion of sulfurs against hafnium<br>of sulfur against against hafnium |
| 259 | $E_g$ | - | 259 | in-plane, out-of-phase sulfur layer shearing<br>sulfur layer shearing |
| 300 | $E_u$ $(LO)$ | 310 | 325 | in-plane, out-of-phase motion of sulfurs against hafnium<br>of sulfur against hafnium |
| 316 | $A_{1g}$ | - | 336 | out-of-plane, out-of-phase sulfur layer breathing<br>sulfur layer breathing |
| 321 | $A_{2u}$ | 336 | - | out-of-plane, in-phase stretch of sulfur layer<br>stretch of sulfur layer |
| | $E_u + A_{2u}$ | 475 | | combination mode |
| | $2(A_{1g})$ | | 650 | overtone mode |

Table 4.1: Vibrational mode assignments of 1T-$HfS_2$. All values are in $cm^{-1}$. The Raman and Infrared values are collected by S. N. Neal and J. L. Musfeldt.

term added to the dynamical matrices of ionic insulators at the zone center[32]:

$$D^{nan}_{st,\alpha\beta} = \lim_{\mathbf{q}\to 0} \frac{1}{\sqrt{m_s m_t}} \frac{4\pi}{\Omega} e^2 \frac{(\mathbf{q}\cdot\mathbf{Z^*_{B,s}})_\alpha (\mathbf{q}\cdot\mathbf{Z^*_{B,t}})_\beta}{\mathbf{q}\cdot\boldsymbol{\varepsilon}(\infty)\cdot\mathbf{q}} \tag{4.3}$$

Here the $s, t$ are atomic indices and $\alpha, \beta$ are cartesian directions. $Z^*_B$ is the Born effective charge and $\mathbf{q}$ is the wavevector. With this extra term present in the dynamical matrix, the two-fold degeneracy of the $E_u$ optical modes is lifted:

$$\omega^2_{Eu,TO} - \omega^2_{Eu,LO} = D^{nan}_{Eu} = \frac{4\pi}{\Omega\boldsymbol{\varepsilon}_{xx}(\infty)} e^2 \left( \sum_i \frac{\mathbf{u_s}\cdot\mathbf{Z^*_{B,i}}}{\sqrt{m_i}} \right)^2, \tag{4.4}$$

where $u_i$ is the displacement vector of $E_u(TO)$ mode. By considering the fact that $Z^*_{\mathrm{Hf},xx}$ is always equal to $2\cdot Z^*_{\mathrm{S},xx}$ because of charge neutrality, and the symmetry imposed form

of the $E_u$ displacement pattern, we can write this equation for $\mathbf{q} \parallel \hat{x}$ as (the proof is in the next session):

$$\omega_{TO}^2 - \omega_{LO}^2 = \frac{4\pi}{\Omega \varepsilon_{xx}(\infty)} e^2 \frac{[Z^*_{\mathrm{Hf},x}]^2}{m^*} \tag{4.5}$$

where the $m^*$ is the effective mass, determined by:

$$\frac{1}{m^*} = \frac{1}{m_{\mathrm{Hf}}} + \frac{1}{2m_{\mathrm{S}}}. \tag{4.6}$$

In this case, the effective mass is 47.02 $m_u$. We use this result along with Equation (4.5) to analyze the experimental Born effective charge below. Gaussian units are employed.

## 4.4 LO-TO splitting of the $E_u$ mode in 1T-$HfS_2$

The proper derivation of the equation(4.5) needs to introduce the atomic displacements of the $E_u$ modes into the equation(4.4). The atomic displacement pattern of the $E_u$ modes can be determined using group theory analysis: The experimentally determined space group of $HfS_2$ is $P\bar{3}m1$ (#164), which is in the trigonal crystal system. There are 2 $E_u$ phonon modes in total, of which one is optical and the other one is acoustic. The optical mode is split into two due to the LO-TO splitting. The form of the dynamical matrix eigenvectors

for both the acoustic and the optical $E_u$ mode is set by symmetry to be:

$$\mathbf{Eu_{A1}} = \begin{bmatrix} \sqrt{m_{\mathrm{Hf}}} \\ 0 \\ 0 \\ \sqrt{m_{\mathrm{S}}} \\ 0 \\ 0 \\ \sqrt{m_{\mathrm{S}}} \\ 0 \\ 0 \end{bmatrix} \mathbf{Eu_{A2}} = \begin{bmatrix} 0 \\ \sqrt{m_{\mathrm{Hf}}} \\ 0 \\ 0 \\ \sqrt{m_{\mathrm{S}}} \\ 0 \\ 0 \\ \sqrt{m_{\mathrm{S}}} \\ 0 \end{bmatrix} \mathbf{Eu_{O1}} = \begin{bmatrix} \sqrt{m_{\mathrm{S}}} \\ 0 \\ 0 \\ -\frac{\sqrt{m_{\mathrm{Hf}}}}{2} \\ 0 \\ 0 \\ -\frac{\sqrt{m_{\mathrm{Hf}}}}{2} \\ 0 \\ 0 \end{bmatrix} \mathbf{Eu_{O2}} = \begin{bmatrix} 0 \\ \sqrt{m_{\mathrm{S}}} \\ 0 \\ 0 \\ -\frac{\sqrt{m_{\mathrm{Hf}}}}{2} \\ 0 \\ 0 \\ -\frac{\sqrt{m_{\mathrm{Hf}}}}{2} \\ 0 \end{bmatrix} \begin{matrix} (\mathrm{Hf}_x) \\ (\mathrm{Hf}_y) \\ (\mathrm{Hf}_z) \\ (\mathrm{S}_{1x}) \\ (\mathrm{S}_{1y}) \\ (\mathrm{S}_{1z}) \\ (\mathrm{S}_{2x}) \\ (\mathrm{S}_{2y}) \\ (\mathrm{S}_{2z}) \end{matrix} \tag{4.7}$$

such that $Eu_A$ and $Eu_O$ denote acoustic and optical $E_u$ modes, respectively. The physical meaning of each vector component is listed at the end, where $\mathrm{Hf}_x$ means the displacement of Hf-atom in the x-direction. The last panel in figure 4.1(c) shows a schematic of this optical

mode. Normalizing the eigenvectors gives:

$$\mathbf{Eu_{O1}} = \begin{bmatrix} \sqrt{\frac{2m_S}{2m_S+m_{Hf}}} \\ 0 \\ 0 \\ -\sqrt{\frac{m_{Hf}}{2(2m_S+m_{Hf})}} \\ 0 \\ 0 \\ -\sqrt{\frac{m_{Hf}}{2(2m_S+m_{Hf})}} \\ 0 \\ 0 \end{bmatrix} \mathbf{Eu_{O2}} = \begin{bmatrix} 0 \\ \sqrt{\frac{2m_S}{2m_S+m_{Hf}}} \\ 0 \\ 0 \\ -\sqrt{\frac{m_{Hf}}{2(2m_S+m_{Hf})}} \\ 0 \\ 0 \\ -\sqrt{\frac{m_{Hf}}{2(2m_S+m_{Hf})}} \\ 0 \end{bmatrix} \begin{matrix} (\mathrm{Hf}_x) \\ (\mathrm{Hf}_y) \\ (\mathrm{Hf}_z) \\ (\mathrm{S}_{1x}) \\ (\mathrm{S}_{1y}) \\ (\mathrm{S}_{1z}) \\ (\mathrm{S}_{2x}) \\ (\mathrm{S}_{2y}) \\ (\mathrm{S}_{2z}) \end{matrix} \tag{4.8}$$

Writing the dynamical matrix on the basis of the two components of the $E_u$ mode results in a diagonal $2 \times 2$ matrix with the dynamical matrix eigenvalues $D^{an}_{Eu}$ on the diagonals. This is the analytical contribution to the dynamical matrix, which gives the TO frequencies. In order to obtain the LO frequencies one needs to add the so-called nonanalytical contribution to the dynamical matrix as well[32]:

$$D^{nan}_{st,\alpha\beta}(q \to 0) = \frac{4\pi}{\Omega} e^2 \frac{(\mathbf{q} \cdot \mathbf{Z_S})_\alpha (\mathbf{q} \cdot \mathbf{Z_t})_\beta}{\mathbf{q} \cdot \boldsymbol{\varepsilon}(\infty) \cdot \mathbf{q}}, \tag{4.9}$$

where the $s, t$ are atomic indices and $\alpha, \beta$ are directional indices. Here, Gaussian units are used. The limit is taken as the wavevector $\mathbf{q}$ approaches zero from the direction of the polarization induced by the LO mode. The splitting between the transverse and longitudinal modes along a crystal axis, for example the [100] direction, can be evaluated in terms of

the normalized $E_u$ dynamical matrix eigenvectors as

$$\omega_{TO}^2 - \omega_{LO}^2 = D_{Eu1}^{nan} = \frac{4\pi}{\Omega\varepsilon_{xx}(\infty)} e^2 \gamma_m^2. \tag{4.10}$$

Here $\gamma_m$ is the polarization induced by a unit displacement by the dynamical matrix eigenvalue $|\vec{u}| = 1$. In this sense it is like a mode effective charge, however due to normalization of the dynamical matrix eigenvector (not the displacement) it has different units than $Z$:

$$\gamma_m = \sum_i \frac{\mathbf{u_i} \cdot \mathbf{Z_i}}{\sqrt{m_i}}, \tag{4.11}$$

where $u_i$ is the $i^{th}$ component of the dynamical matrix eigenvector. In this case, the eigenvector is the normalized one for the $E_u$ mode, which is shown in the first row of Equation **??**.

In the specific (diatomic) case of $HfS_2$, we have $Z_{\mathrm{Hf},xx} = -2Z_{\mathrm{S},xx}$, thus the effective mode would be:

$$\begin{aligned}
\gamma_m &= \sqrt{\frac{2m_{\mathrm{S}}}{2m_{\mathrm{S}} + m_{\mathrm{Hf}}}} \frac{Z_{\mathrm{Hf},xx}}{\sqrt{m_{\mathrm{Hf}}}} - 2\sqrt{\frac{m_{\mathrm{Hf}}}{2(2m_{\mathrm{S}} + m_{\mathrm{Hf}})}} \frac{Z_{\mathrm{S},xx}}{\sqrt{m_{\mathrm{S}}}} \\
&= \left( \sqrt{\frac{2m_{\mathrm{S}}}{2m_{\mathrm{S}} + m_{\mathrm{Hf}}}} \frac{1}{\sqrt{m_{\mathrm{Hf}}}} + \sqrt{\frac{m_{\mathrm{Hf}}}{2(2m_{\mathrm{S}} + m_{\mathrm{Hf}})}} \frac{1}{\sqrt{m_{\mathrm{S}}}} \right) Z_{\mathrm{Hf},xx} \\
&= \frac{1}{\sqrt{m^*}} Z_{\mathrm{Hf},xx}
\end{aligned} \tag{4.12}$$

Here the $m^*$ is the effective mass, which has the relationship:

$$\frac{1}{m^*} = \left( \sqrt{\frac{2m_{\mathrm{S}}}{2m_{\mathrm{S}} + m_{\mathrm{Hf}}}} \frac{1}{\sqrt{m_{\mathrm{Hf}}}} + \sqrt{\frac{m_{\mathrm{Hf}}}{2(2m_{\mathrm{S}} + m_{\mathrm{Hf}})}} \frac{1}{\sqrt{m_{\mathrm{S}}}} \right)^2 = \frac{1}{m_{\mathrm{Hf}}} + \frac{1}{2m_{\mathrm{S}}} \tag{4.13}$$

which gives 47.02 $u$ for 1T-$HfS_2$.

In the end, the Born effective charge can be simplified using this effective mass from Equation 4.10:

$$\omega_{TO}^2 - \omega_{LO}^2 = \frac{4\pi}{\Omega\varepsilon_{xx}(\infty)} e^2 \frac{Z_{\mathrm{Hf},xx}^2}{m^*} \tag{4.14}$$

## 4.5 Results from DFT and experiments

The Born effective charge of transition metal dichalcogenides has been of sustained interest[173,179,180,205,206]. Born effective charge can be calculated from first principles as summarized in the method section and revealed directly from spectroscopic data by taking into account the relationship between the longitudinal and transverse optic phonon frequencies as indicated in Eqn. 4.5. The Born effective charge can be given by the equation(4.2) from our DFPT calculation, which is $Z_B^* = 6.38$ for Hf atoms in the in-plane direction.

The Raman and infrared spectrum is collected by our experimental collaborators in order to determine the value of LO-TO splitting which is further used to calculate the Born effective charge. The original data is shown in the figure 4.2. The Born effective charge calculated by the LO-TO splitting in Raman and Infrared spectrum is $Z_B^* = 5.33$ for Hf atoms in the in-plane direction, which shows great agreement with our DFT result.

| $\omega(LO)$ ($\mathrm{cm}^{-1}$) | $\omega(TO)$ ($\mathrm{cm}^{-1}$) | $\varepsilon(\infty)$ | $m_k$ (u) | $Z_B^*$ ($e$) | Reference |
|---|---|---|---|---|---|
| 300 | 152 | 6.33 | - | 3.46 | Chen *et. al.*[181] |
| 318 | 166 | 6.20 | 23.59 | 3.90 | Lucovsky *et. al.*[180] |
| 321 | 166 | 6.20 | - | 5.50 | Uchida *et. al.*[179] |
| 310 | 155 | 6.20 | 47.02 | 5.33 | This work (experiment) |
| 300 | 152 | 8.09 | 47.02 | 6.38 | This work (theory) |

Table 4.2: Comparison of parameters and Born effective charge for the $E_u$ mode of 1T-$HfS_2$. Literature results and our own work - both experimental and theoretical - are included.

Interestingly, prior studies have led to a variety of Born effective charges for $HfS_2$ with

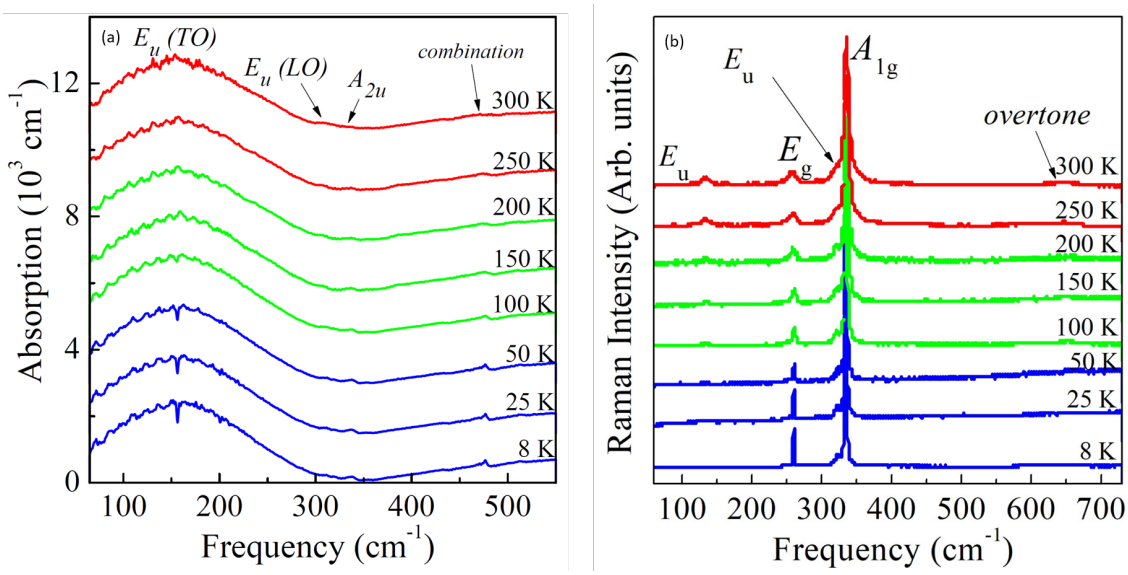


Figure 4.2: (a) Infrared absorption spectra of 1T-$HfS_2$ as a function of temperature. The color scheme emphasizes the different phases, and the curves are offset for clarity. (b)Raman scattering response of 1T-$HfS_2$ as a function of temperature. The mode symmetries are labeled, and the spectra are offset for clarity. The data is collected by S. N. Neal and J. L. Musfeldt.

values from $3.46e$ to $5.5e$[179–181]. These findings are summarized in Table 4.2. The variations in $Z_B^*$ are possibly due to differences in $m_k$, cell volume, and (to a lesser extent) $\epsilon(\infty)$ as well as variability $\omega_{LO}$ and $\omega_{TO}$. Our experimental and theoretical value is consistent with the large *LO-TO* splitting which signals robust ionicity. By comparison, transition metal dichalcogenides like 2H-$MoS_2$ have much smaller LO-TO splitting and $Z_B^* = 1.11e$ in the *ab*-plane[206,207].

## 4.6 Origin of anomalous large Born effective charge

In a completely ionic crystal where electrons are attached to ions and displaced along with them by the same exact amount, the dynamical Born effective charge is equal to the formal ionic charge - which would have given $Z_B^* = 4$ for Hf. 1T-$HfS_2$ is closer to this limit due to

Table 4.3: A band-by-band decomposition of Born effective charge of Hf in $HfS_2$ using integration of Wannier function. All units are in $e$. The core charges correspond to the charge of the ionic Hf core of the PAW potential used in the DFT calculation, which has all valence orbitals empty. (Only the $5p$, $5d$ and $6s$ electrons of Hf atoms and $3s$, $3p$ electrons of S atoms are considered explicitly in the DFT calculation.) Hf-$5d$ orbitals are not shown because they are formally not occupied.

| | Core charge | Hf:$5p$ | S:$3s$ | S:$3p$ | total |
|---|---|---|---|---|---|
| $Z_{B,xx}$ | +10 | -6.08 | +0.30 | +2.34 | 6.56 |
| $Z_{B,zz}$ | +10 | -6.20 | 0.01 | -1.86 | 1.93 |

the low electronegativity of the cation (1.3 in the Pauling scale). This is lower than any $3d$ transition metal, including Mo which has an electronegativity of 2.2. The electronegativity of S is 2.6, so the Mo-S bonds in $MoS_2$ are highly covalent. Nevertheless, we note that the Born effective charge of Hf in the in-plane direction is more than 50% larger than the nominal charge of +4. This anomalous Born charge signals either (i) covalency between the cations and anions or (ii) cation polarizability[204]. Uchida explored the issue in terms of static and dynamic charge[179]. We can address the question more robustly with contemporary tools.

Maximally localized Wannier functions can be utilized to explain the origin of anomalous Born effective charges[208]. The macroscopic electronic polarization can be expressed in terms of the center of localized Wannier functions as

$$P_{\beta}^{el} = \frac{1}{\Omega_0} \sum_{n}^{occ} \int r_{\beta} |W_n(r)|^2 d^3r, \tag{4.15}$$

where $W_n(r)$ is the Wannier function and the sum is over the filled Wannier orbitals. By displacing the Hf atoms in the in-plane and out-of-plane directions, it is possible to calculate the shift of the center of each Wannier function, and hence get a orbital-by-orbital or band-by-band decomposition of the Born effective charges.

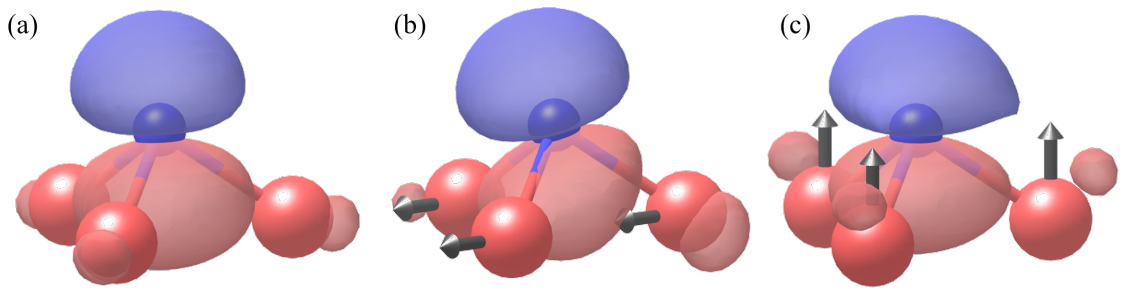


Figure 4.3: Visualization of a sulfur $p_z$ maximally localized Wannier orbital. The blue atom is a sulfur center whereas red atoms are bonded hafnium centers. The red and blue lobes of the orbital indicates the opposite signs of the wavefunction. No structural distortion is present in (a). Hf atoms are displaced in-plane and out-of-plane in (b) and (c) respectively.

Table 4.3 shows the band-by-band contributions to the Born effective charges of Hf. It turns out the despite the large electronegativity difference between Hf and S, covalency of Hf-S bonds is the dominant reason behind the anomalous Born effective charge in this compound: the Wannier centers of the electrons in the S-3$p$ bands displace significantly when the Hf ion is displaced. On the other hand, the Hf-5$p$ electrons are displaced almost exactly as much as the Hf ion core itself. Thus, S-3$p$ orbitals contribute most to the difference between Born effective and nominal charge.

Taking a closer look at the electrons in the S-3$p$ orbitals, Fig. 4.3 shows one of the Wannier functions with and without the Hf ion displacement. In line with the strongly ionic density of states, the S-$p$ electrons are mostly localized on S, with small lobes on Hf indicating hybridization. When Hf atoms are displaced in an in-plane direction, one of the three Hf-S bonds is shortened while the other two are elongated. The shortened bond causes the Wannier function to be tilted, and its center shifted towards the Hf atom, shown in Fig. 4.3(b). This explains why S-3$p$ orbitals will contribute a positive polarization value when Hf atoms are moving in-plane. On the other hand, when Hf atoms move in

the out-of-plane direction, the shape of the hybridized electron density on the Hf atom changes, showing a significant qualitative change in the hybridization, as well as a shift in the S-3$p$ Wannier centers parallel to the Hf displacement. This leads to a negative dynamic contribution of S-3$p$ to the out-of-plane Hf effective charge. Though only one S-3$p$ orbital is shown here, the others are similar.

As a comparison, the Born effective charge of Mo in 2H-$MoS_2$ is 1.1 - 1.2$e$ in the in-plane direction[206], and theoretical results suggest a sign reversal of the cation Born charge[209]. This is likely because of a much stronger covalency in $MoS_2$ than in $HfS_2$, which results in more electrons transferred from S anions onto Mo cations when Mo ions are displaced. Note that there is a $4d_{z^2} - p_z$ antibonding orbital in Mo-S bonds near the Fermi level because Mo's 4$d$ band is partially filled, and this orbital can result in large electron transfer in a way similar to $\pi$-backbonding in organic chemistry[209].

# Chapter 5

# Conclusions

In this thesis, the lattice dynamics of layered perovskites and transition metal dichalcogenides is studied using first-principle method, specifically density functional theory. Our goal is to advance the understanding of hybrid improper ferroelectricity and atomic interactions. In Chapter 2, we explained the strain-induced phase transition in layered perovskites from the view of free energy and explored the possibility of tuning polarization switching barrier using strain. In Chapter 3, we proposed an idea of free charge induced ferroelectricity, which was thought to be impossible for a very long time. In Chapter 4, our study of the bonding nature in transition metal dichalcogenides showed a great agreement with our experimental collaborators, and we also explained the results from a microscopic point of view. Although our studies were only focused on limited amount of compounds and certain properties, the approaches can be generalized and applied to many other systems for a lot more applications.

With all the efforts, the main idea of my research is to show that the first-principles method are powerful tools for lattice dynamics studies and capable of predicting and ex-

plaining previously unobserved physical phenomenon. In fact, we are witnessing more and more examples of 'materials by design from first-principles method' in the last decade, like hybrid improper ferroelectricity[37] and topological insulator[210]. The rapid growth of computational power and data makes the idea of materials design into reality.

In the last section of my thesis, I would like to conclude my thesis by looking forward and discuss what else can be done in this field: one of them is anharmonic lattice dynamics. All the lattice dynamics we discussed in this thesis is limited to harmonic approximation, which only considers up to second-order free energy expansion of phonons. But the higher-order expansions can be critical in terms of phonon-phonon interactions. Phonon-phonon interactions is the dominant effect of phonon scattering in a pure crystalline system, which makes it important in terms of calculating the shifting and broadening of Raman peaks, or the thermal conductivity.

Effort has been made to predict the thermal conductivity in perovskites[211], but there is a lack of discussion of how to tune the thermal conductivity. A thorough discussion of the strain and gating effect on the phonons in perovskites were presented in Chapter 2 and Chapter 3 of this thesis, which reveals the possibility of tuning phonon. It is possible that the anharmonic term will also be affected by these external parameters, which can further lower or increase the thermal conductivity.

The other trend we are seeing right now is the machine-learned interatomic interactions. Though the rapid growth of computational power has made certain large-scale simulation more accessible than ever, it is still undeniable that many systems are still far beyond the capability of traditional density functional theory. For example, the study of twisted-bilayer graphene requires enormous supercells. However, with the help of neural network,

it is possible to perform large-scale atomistic simulation of the thermal and mechanical properties in multilayer graphene[212]. Several different neural network architectures have already been developed[213,214] and the cost of computation only scales linearly with the system size.

With all this benefits of machine-learned interatomic potentials, it is possible to study finite-size systems without introducing approximations. The line defects in $BaSnO_3$ thin films is something very hard to be captured using DFT without decent amounts of approximation[215] because of its localized disorder. While the machine-learned interactomic potential could easily reproduce the real-world atomistic configuration. That being said, the DFT calculation is the foundation of any machine learning algorithm and remains unsubstitutable for electronic structure study.

In summary, the study of lattice dynamic using first-principles method has greatly advanced our understanding of many novel physics phenomenon and technology applications. However, there are still great amounts of technical challenges unsolved that requires further first-principles study or even new methods. I hope this thesis could bring you some inspirations and the idea of a possible 'paradigm shift' of material-by-design.

# Bibliography


[1] Turan Birol, Nicole A. Benedek, and Craig J. Fennie. Interface Control of Emergent Ferroic Order in Ruddlesden-Popper Srn+1TinO3n+1. *Physical Review Letters*, 107 (25):257602, 2011.

[2] Che-Hui Lee, Nathan D Orloff, Turan Birol, Ye Zhu, Veronica Goian, Eduard Rocas, Ryan Haislmaier, Eftihia Vlahos, Julia A Mundy, Lena F Kourkoutis, et al. Exploiting dimensionality and defect mitigation to create tunable microwave dielectrics. *Nature*, 502(7472):532, 2013.

[3] S. Ivantchev, E. Kroumova, G. Madariaga, J. M. Pérez-Mato, and M. I. Aroyo. *SUBGROUPGRAPH*: a computer program for analysis of group–subgroup relations between space groups. *Journal of Applied Crystallography*, 33(4):1190–1191, 2000.

[4] Dorian M. Hatch and Harold T. Stokes. INVARIANTS : program for obtaining a list of invariant polynomials of the order-parameter components associated with irreducible representations of a space group . *Journal of Applied Crystallography*, 36(3):951–952, 2003.

[5] Philip W Anderson. More is different: broken symmetry and the nature of the hierarchical structure of science. *Science*, 177(4047):393–396, 1972.

[6] M.T. Dove. Introduction to the theory of lattice dynamics. *École thématique de la Société Française de la Neutronique*, 12:123–159, 2011.

[7] Werner Heisenberg. Multi-body problem and resonance in the quantum mechanics. *Physik*, 38:411–426, 1926.

[8] P Hohenberg and WJPR Kohn. Density functional theory (dft). *Phys. Rev*, 136:B864, 1964.

[9] Kurt Lejaeghere, Gustav Bihlmayer, Torbjörn Björkman, Peter Blaha, Stefan Blügel, Volker Blum, Damien Caliste, Ivano E Castelli, Stewart J Clark, Andrea Dal Corso, et al. Reproducibility in density functional theory calculations of solids. *Science*, 351 (6280):aad3000, 2016.

[10] Giuseppe Grosso and Giuseppe Pastori Parravicini. *Solid state physics*. Academic press, 2013.

[11] JR AS BARKER and R Loudon. Response functions in the theory of raman scattering by vibrational and polariton modes in dielectric crystals. *Reviews of Modern Physics*, 44(1):18, 1972.

[12] GJ Ackland, MC Warren, and SJ Clark. Practical methods in ab initio lattice dynamics. *Journal of Physics: Condensed Matter*, 9(37):7861, 1997.

[13] Ronald E. Cohen. Origin of ferroelectricity in perovskite oxides. *Nature*, 358(6382): 136–138, 1992.

[14] A. Ward, D. A. Broido, Derek A. Stewart, and G. Deinzer. Ab initio theory of the lattice thermal conductivity in diamond. *Physical Review B - Condensed Matter and Materials Physics*, 80(12):1–8, 2009.

[15] Feliciano Giustino. Electron-phonon interactions from first principles. *Reviews of Modern Physics*, 89(1):015003, 2017.

[16] Eugen Merzbacher. *Quantum mechanics*. Jones & Bartlett Publishers, 1961.

[17] Douglas R Hartree. The wave mechanics of an atom with a non-coulomb central field. part i. theory and methods. In *Mathematical Proceedings of the Cambridge Philosophical Society*, volume 24, pages 89–110. Cambridge university press, 1928.

[18] Vladimir Fock. Näherungsmethode zur lösung des quantenmechanischen mehrkörperproblems. *Zeitschrift für Physik*, 61(1):126–148, 1930.

[19] John C Slater. Note on hartree's method. *Physical Review*, 35(2):210, 1930.

[20] C. C. J. Roothaan. New developments in molecular orbital theory. *Rev. Mod. Phys.*, 23:69–89, 1951.

[21] Chaim L Pekeris. Ground state of two-electron atoms. *Physical Review*, 112(5):1649, 1958.

[22] Walter Kohn and Lu Jeu Sham. Self-consistent equations including exchange and correlation effects. *Physical review*, 140(4A):A1133, 1965.

[23] Pierre Hohenberg and Walter Kohn. Inhomogeneous electron gas. *Physical review*, 136(3B):B864, 1964.

[24] Roberto Car. Fixing jacob's ladder. *Nature chemistry*, 8(9):820–821, 2016.

[25] D. M. Ceperley and B. J. Alder. Ground state of the electron gas by a stochastic method. *Phys. Rev. Lett.*, 45:566–569, 1980.

[26] Carlos Fiolhais, Fernando Nogueira, and Miguel AL Marques. *A primer in density functional theory*, volume 620. Springer Science & Business Media, 2003.

[27] Philipp Haas, Fabien Tran, and Peter Blaha. Calculation of the lattice constant of solids with semilocal functionals. *Physical Review B*, 79(8):085104, 2009.

[28] Arpita Paul and Turan Birol. Applications of dft+ dmft in materials science. *Annual Review of Materials Research*, 49:31–52, 2019.

[29] Christoph Freysoldt, Blazej Grabowski, Tilmann Hickel, Jörg Neugebauer, Georg Kresse, Anderson Janotti, and Chris G Van de Walle. First-principles calculations for point defects in solids. *Reviews of modern physics*, 86(1):253, 2014.

[30] Charles Kittel. *Introduction to Solid State Physics*. $8^{th}$ edition, Wiley, 2004.

[31] Peter E Blöchl. Projector augmented-wave method. *Physical review B*, 50(24):17953, 1994.

[32] Stefano Baroni, Stefano De Gironcoli, Andrea Dal Corso, and Paolo Giannozzi. Phonons and related crystal properties from density-functional perturbation theory. *Rev. Mod. Phys.*, 73(2):515–562, 2001.

[33] M. Gajdoš, K. Hummer, G. Kresse, J. Furthmüller, and F. Bechstedt. Linear optical properties in the projector-augmented wave methodology. *Phys. Rev. B*, 73:045112, 2006.

[34] Shutong Li. Suppressing the ferroelectric switching barrier in hybrid improper ferroelectrics. *npj Computational Materials*, 6(168), 2020.

[35] CA Randall, RE Newnham, and LE Cross. History of the first ferroelectric oxide, batio3. *Materials Research Institute, The Pennsylvania State University, University Park, Pa, USA*, 1, 2004.

[36] Nicole A. Benedek and Craig J. Fennie. Why are there so few perovskite ferroelectrics? *Journal of Physical Chemistry C*, 117(26):13339–13349, 2013.

[37] Nicole A. Benedek and Craig J. Fennie. Hybrid improper ferroelectricity: A mechanism for controllable polarization-magnetization coupling. *Phys. Rev. Lett.*, 106(10): 107204, 2011.

[38] Yoon Seok Oh, Xuan Luo, Fei-Ting Huang, Yazhong Wang, and Sang-Wook Cheong. Experimental demonstration of hybrid improper ferroelectricity and the presence of abundant charged walls in (Ca,Sr)3Ti2O7 crystals . *Nature materials*, 14(4):407–413, 2015.

[39] Yazhong Wang, Fei Ting Huang, Xuan Luo, Bin Gao, and Sang Wook Cheong. The First Room-Temperature Ferroelectric Sn Insulator and Its Polarization Switching Kinetics. *Advanced Materials*, 29(2), 2017.

[40] Suguru Yoshida, Hirofumi Akamatsu, Ryosuke Tsuji, Olivier Hernandez, Haricharan Padmanabhan, Arnab Sen Gupta, Alexandra S. Gibbs, Ko Mibu, Shunsuke Murai, James M. Rondinelli, Venkatraman Gopalan, Katsuhisa Tanaka, and Koji Fujita. Hybrid Improper Ferroelectricity in (Sr,Ca)3Sn2O7 and Beyond: Universal Relationship between Ferroelectric Transition Temperature and Tolerance Factor in n=2 Ruddlesden–Popper Phases. *Journal of the American Chemical Society*, 140(46): 15690–15700, 2018.

[41] Suguru Yoshida, Koji Fujita, Hirofumi Akamatsu, Olivier Hernandez, Arnab Sen Gupta, Forrest G. Brown, Haricharan Padmanabhan, Alexandra S. Gibbs, Toshihiro Kuge, Ryosuke Tsuji, Shunsuke Murai, James M. Rondinelli, Venkatraman Gopalan, and Katsuhisa Tanaka. Ferroelectric Sr3Zr2O7: Competition between Hybrid Improper Ferroelectric and Antiferroelectric Mechanisms. *Adv. Funct. Mater.*, 28(30): 1801856, 2018.

[42] Michael J Pitcher, Pranab Mandal, Matthew S Dyer, Jonathan Alaria, Pavel Borisov, Hongjun Niu, John B Claridge, and Matthew J Rosseinsky. Tilt engineering of spontaneous polarization and magnetization above 300K in a bulk layered perovskite. *Science*, 347(6220):420–424, 2015.

[43] M. M. Elcombe, E. H. Kisi, K. D. Hawkins, T. J. White, P. Goodman, and S. Matheson. Structure determinations for Ca3Ti2O7, Ca4Ti3O10, Ca3.6Sr0.4Ti3O10 and a refinement of Sr3Ti2O7. *Acta Crystallogr. B*, 47(3):305–314, 1991.

[44] Andrew T. Mulder, Nicole A. Benedek, James M. Rondinelli, and Craig J. Fennie. Turning ABO3 antiferroelectrics into ferroelectrics: Design rules for practical rotation-driven ferroelectricity in double perovskites and A3B2O7 Ruddlesden-popper compounds. *Adv. Funct. Mater.*, 23(38):4810–4820, 2013.

[45] M.E. Lines and A.M. Glass. *Principles and Applications of Ferroelectrics and Related Materials*. International series of monographs on physics. OUP Oxford, 2001. ISBN 9780198507789.

[46] Xianghan Xu, Yazhong Wang, Fei Ting Huang, Kai Du, Elizabeth A. Nowadnick, and Sang Wook Cheong. Highly Tunable Ferroelectricity in Hybrid Improper Ferroelectric Sr3Sn2O7. *Adv. Funct. Mater.*, 2003623:1–9, 2020.

[47] J. F. Scott. Applications of modern ferroelectrics. *Science*, 315(5814):954–959, 2007.

[48] J. Cole, S. J. Ahmed, L. Curiel, S. Pichardo, and O. Rubel. Marble game with optimal ferroelectric switching. *J. Phys. Condens. Matter*, 26(13):135901, 2014.

[49] Ruijuan Xu, Ran Gao, Sebastian E. Reyes-Lillo, Sahar Saremi, Yongqi Dong, Hongling Lu, Zuhuang Chen, Xiaoyan Lu, Yajun Qi, Shang Lin Hsu, Anoop R. Damodaran, Hua Zhou, Jeffrey B. Neaton, and Lane W. Martin. Reducing Coercive-Field Scaling in Ferroelectric Thin Films via Orientation Control. *ACS Nano*, 12(5):4736–4743, 2018.

[50] Z. Q. Liu, J. H. Liu, M. D. Biegalski, J. M. Hu, S. L. Shang, Y. Ji, J. M. Wang, S. L. Hsu, A. T. Wong, M. J. Cordill, B. Gludovatz, C. Marker, H. Yan, Z. X. Feng, L. You, M. W. Lin, T. Z. Ward, Z. K. Liu, C. B. Jiang, L. Q. Chen, R. O. Ritchie, H. M. Christen, and R. Ramesh. Electrically reversible cracks in an intermetallic film controlled by an electric field. *Nature Communications*, 9(1):1–7, 2018.

[51] X. Li, L. Yang, C. F. Li, M. F. Liu, Z. Fan, Y. L. Xie, C. L. Lu, L. Lin, Z. B. Yan, Z. Zhang, J. Y. Dai, J. M. Liu, and S. W. Cheong. Ultra-low coercive field of improper ferroelectric Ca3Ti2O7 epitaxial thin films. *Appl. Phys. Lett.*, 110(4):42901, 2017.

[52] Tianqi Wang, Abhinav Prakash, Yongqi Dong, Tristan Truttmann, Ashley Bucsek, Richard James, Dillon D Fong, Jong-Woo Kim, Philip J Ryan, Hua Zhou, Turan Birol, and Bharat Jalan. Engineering SrSnO 3 Phases and Electron Mobility at Room Temperature Using Epitaxial Strain. *ACS Applied Materials & Interfaces*, 10 (50):43802–43808, 2018.

[53] Vipul Chaturvedi, Jeff Walter, Arpita Paul, Alexander Grutter, Brian Kirby, Jong Seok Jeong, Hua Zhou, Zhan Zhang, Biqiong Yu, Martin Greven, K. Andre Mkhoyan, Turan Birol, and Chris Leighton. Strain-induced majority carrier inversion in ferromagnetic epitaxial $LaCoo_{3-\delta}$ thin films. *Phys. Rev. Materials*, 4:034403, 2020.

[54] S. Clima, D. J. Wouters, C. Adelmann, T. Schenk, U. Schroeder, M. Jurczak, and G. Pourtois. Identification of the ferroelectric switching process and dopant-dependent switching properties in orthorhombic HfO2: A first principles insight. *Appl. Phys. Lett.*, 104(9), 2014.

[55] Xue Zeng Lu and James M. Rondinelli. Epitaxial-strain-induced polar-to-nonpolar transitions in layered oxides. *Nat. Mater.*, 15(9):951–955, 2016.

[56] Elizabeth A. Nowadnick and Craig J. Fennie. Domains and ferroelectric switching pathways in Ca3Ti2O7 from first principles. *Phys. Rev. B*, 94(10):104105, 2016.

[57] Jason M. Munro, Hirofumi Akamatsu, Haricharan Padmanabhan, Vincent S. Liu, Yin Shi, Long Qing Chen, Brian K. Vanleeuwen, Ismaila Dabo, and Venkatraman Gopalan. Discovering minimum energy pathways via distortion symmetry groups. *Phys. Rev. B*, 98(8):85107, 2018.

[58] G. Kresse and D. Joubert. From ultrasoft pseudopotentials to the projector augmented-wave method. *Phys. Rev. B*, 59:1758–1775, 1999.

[59] G. Kresse and J. Hafner. Ab initio molecular dynamics for liquid metals. *Phys. Rev. B*, 47:558–561, 1993.

[60] John P. Perdew, Adrienn Ruzsinszky, Gábor I. Csonka, Oleg A. Vydrov, Gustavo E. Scuseria, Lucian A. Constantin, Xiaolan Zhou, and Kieron Burke. Restoring the density-gradient expansion for exchange in solids and surfaces. *Phys. Rev. Lett.*, 100: 136406, 2008.

[61] C. F. Li, S. H. Zheng, H. W. Wang, J. J. Gong, X. Li, Y. Zhang, K. L. Yang, L. Lin, Z. B. Yan, Shuai Dong, and J. M. Liu. Structural transitions in hybrid improper ferroelectric Ca3Ti2O7 tuned by site-selective isovalent substitutions: A first-principles study. *Phys. Rev. B*, 97(18), 2018.

[62] Brendan J. Kennedy, Qingdi Zhou, and Maxim Avdeev. The ferroelectric phase of CdTiO3: A powder neutron diffraction study. *Journal of Solid State Chemistry*, 184 (11):2987–2993, 2011.

[63] JM Henriques, EWS Caetano, VN Freire, JAP da Costa, and EL Albuquerque. Ab initio structural, electronic and optical properties of orthorhombic CaGeO3. *Journal of Solid State Chemistry*, 180(3):974–980, 2007.

[64] Hiroki Moriwake, Akihide Kuwabara, Craig AJ Fisher, Hiroki Taniguchi, Mitsuru Itoh, and Isao Tanaka. First-principles calculations of lattice dynamics in CdTiO 3 and CaTiO 3: Phase stability and ferroelectricity. *Phys. Rev. B*, 84(10):104114, 2011.

[65] Victor Moritz Goldschmidt. Die gesetze der krystallochemie. *Naturwissenschaften*, 14(21):477–485, 1926.

[66] Michael W. Lufaso and Patrick M. Woodward. Prediction of the crystal structures of perovskites using the software program SPuDS. *Acta Crystallogr. B*, 57(6):725–738, 2001.

[67] Graeme Henkelman and Hannes Jónsson. Improved tangent estimate in the nudged elastic band method for finding minimum energy paths and saddle points. *The Journal of chemical physics*, 113(22):9978–9985, 2000.

[68] Brian K. Vanleeuwen and Venkatraman Gopalan. The antisymmetry of distortions. *Nature Communications*, 6:8818, 2015.

[69] Hari Padmanabhan, Jason M Munro, Ismaila Dabo, and Venkatraman Gopalan. Antisymmetry: Fundamentals and Applications. *Annual Review of Materials Research*, 50(1):annurev–matsci–100219–101404, 2020.

[70] Jason M. Munro, Vincent S. Liu, Venkatraman Gopalan, and Ismaila Dabo. Implementation of distortion symmetry for the nudged elastic band method with DiSPy. *npj Computational Materials*, 5(1):52, 2019.

[71] H.T. Stokes, D.M Hatch, and B.J. Campbell. Isotropy, 2007.

[72] Mois I. Aroyo, Asen Kirov, Cesar Capillas, J. M. Perez-Mato, and Hans Wondratschek. Bilbao crystallographic server. ii. representations of crystallographic point groups and space groups. *Acta Crystallogr. A*, 62(2):115–128, 2006.

[73] MI Aroyo, JM Perez-Mato, C Capillas, E Kroumova, S Ivantchev, G Madariaga, A Kirov, and H Wondratschek. Bilbao crystallographic server: I. databases and crystallographic computing programs. *Zeitschrift fur Kristallographie*, 221(1):15–27, 2006.

[74] M. I. Aroyo, J. M. Perez-Mato, D. Orobengoa, E. Tasci, G. de la Flor, and A. Kirov. Crystallography online: Bilbao crystallographic server. *Bulgarian Chemical Communications*, 43(2):183–197, 2011.

[75] Koichi Momma and Fujio Izumi. *Journal of Applied Crystallography*, 41:653–658, 2008.

[76] S. N. Ruddlesden and P. Popper. New compounds of the K2NiF4 type. *Acta Crystallogr.*, 10(8):538–539, 1957.

[77] S. N. Ruddlesden and P. Popper. The compound Sr3Ti2O7 and its structure. *Acta Crystallogr.*, 11(1):54–55, 1958.

[78] Hongbin Zhang, Kristjan Haule, and David Vanderbilt. Effective J=1/2 Insulating State in Ruddlesden-Popper Iridates: An LDA+DMFT Study. *Phys. Rev. Lett.*, 111 (24):246402, 2013.

[79] Q. Wang, Y. Cao, J. A. Waugh, S. R. Park, T. F. Qi, O. B. Korneta, G. Cao, and D. S. Dessau. Dimensionality-controlled mott transition and correlation effects in single-layer and bilayer perovskite iridates. *Phys. Rev. B*, 87:245109, 2013.

[80] Wei Li, Shanyuan Niu, Boyang Zhao, Ralf Haiges, Zhiqiang Zhang, Jayakanth Ravichandran, and Anderson Janotti. Band gap evolution in Ruddlesden-Popper phases. *Phys. Rev. Mater.*, 3(10):101601, 2019.

[81] Stanley C Miller and William F Love. *Tables of irreducible representations of space groups and co-representations of magnetic space groups*. Pruett Press, 1967.

[82] Patrick M. Woodward. Octahedral Tilting in Perovskites. II. Structure Stabilizing Forces. *Acta Crystallographica Section B: Structural Science*, 53(1):44–66, 1997.

[83] C. Bradley and A. Cracknell. *The Mathematical Theory of Symmetry in Solids: Representation Theory for Point Groups and Space Groups*. EBSCO ebook academic collection. OUP Oxford, 2010. ISBN 9780199582587.

[84] Xue Zeng Lu and James M. Rondinelli. Room Temperature Electric-Field Control of Magnetism in Layered Oxides with Cation Order. *Adv. Funct. Mater.*, 27(4):1604312, 2017.

[85] A. Salinas-Sanchez, J. L. Garcia-Muñoz, J. Rodriguez-Carvajal, R. Saez-Puche, and J. L. Martinez. Structural characterization of R2BaCuO5 (R = Y, Lu, Yb, Tm, Er, Ho, Dy, Gd, Eu and Sm) oxides by X-ray and neutron diffraction. *Journal of Solid State Chemistry*, 100(2):201–211, 1992.

[86] Ph Ghosez, X. Gonze, and J. P. Michenaud. Coulomb interaction and ferroelectric instability of BaTiO3. *Europhysics Letters*, 33(9):713–718, 1996.

[87] Yurong Yang, Wei Ren, Dawei Wang, and L. Bellaiche. Understanding and Revisiting Properties of EuTiO3 Bulk Material and Films from First Principles. *Phys. Rev. Lett.*, 109(26):267602, 2012.

[88] A. T. Zayak, X. Huang, J. B. Neaton, and Karin M. Rabe. Structural, electronic, and magnetic properties of SrRuO3 under epitaxial strain. *Phys. Rev. B*, 74(9):094104, 2006.

[89] R. J. Zeches, M. D. Rossell, J. X. Zhang, A. J. Hatt, Q. He, C. H. Yang, A. Kumar, C. H. Wang, A. Melville, C. Adamo, G. Sheng, Y. H. Chu, J. F. Ihlefeld, R. Erni, C. Ederer, V. Gopalan, L. Q. Chen, D. G. Schldin, N. A. Spaldin, L. W. Martin, and R. Ramesh. A strain-driven morphotropic phase boundary in BiFeO3. *Science*, 326 (5955):977–980, 2009.

[90] Robert E. Newnham. Phase Transformations in Smart Materials. *Acta Crystallogr. A*, 54(6):729–737, 1998.

[91] Turan Birol, Nicole A. Benedek, Hena Das, Aleksander L. Wysocki, Andrew T. Mulder, Brian M. Abbett, Eva H. Smith, Saurabh Ghosh, and Craig J. Fennie. The magnetoelectric effect in transition metal oxides: Insights and the rational design of new materials from first principles. *Curr. Opin. Solid State Mater. Sci.*, 16(5): 227–242, 2012.

[92] S. P. Beckman, Xinjie Wang, Karin M. Rabe, and David Vanderbilt. Ideal barriers to polarization reversal and domain-wall motion in strained ferroelectric thin films. *Phys. Rev. B*, 79(14), 2009.

[93] R. Dittrich, T. Schrefl, D. Suess, W. Scholz, H. Forster, and J. Fidler. A path method for finding energy barriers and minimum energy paths in complex micromagnetic systems. *Journal of Magnetism and Magnetic Materials*, 250:12–19, 2002.

[94] X. Q. Liu, J. J. Lu, B. H. Chen, B. H. Zhang, and X. M. Chen. Hybrid improper ferroelectricity and possible ferroelectric switching paths in Sr3Hf2O7. *Journal of Applied Physics*, 125(11):114105, 2019.

[95] Ryan C Haislmaier, Greg Stone, Nasim Alem, and Roman Engel-Herbert. Creating ruddlesden-popper phases by hybrid molecular beam epitaxy. *Appl. Phys. Lett.*, 109 (4):043102, 2016.

[96] Shutong Li and Turan Birol. Free-carrier-induced ferroelectricity in layered perovskites. *Physical review letters*, 127(8):087601, 2021.

[97] Hong Jian Zhao, Alessio Filippetti, Carlos Escorihuela-Sayalero, Pietro Delugas, Enric Canadell, L. Bellaiche, Vincenzo Fiorentini, and Jorge Íñiguez. Meta-screening and permanence of polar distortion in metallized ferroelectrics. *Physical Review B*, 97(5): 1–11, 2018.

[98] Jiyan Dai. Introduction to Ferroelectrics. In *Ferroic Materials for Smart Systems*, pages 15–46. Wiley, 2020.

[99] Karin M. Rabe and Philippe Ghosez. First-principles studies of ferroelectric oxides. *Topics in Applied Physics*, 105:117–174, 2007.

[100] Lane W. Martin and Andrew M. Rappe. Thin-film ferroelectric materials and their applications. *Nature Reviews Materials*, 2(2):16087, 2017.

[101] Yong Wang, Xiaohui Liu, J. D. Burton, Sitaram S. Jaswal, and Evgeny Y. Tsymbal. Ferroelectric instability under screened coulomb interactions. *Physical Review Letters*, 109(24):1–5, 2012.

[102] Nicole A. Benedek and Turan Birol. 'Ferroelectric' metals reexamined: Fundamental mechanisms and design considerations for new materials. *Journal of Materials Chemistry C*, 4(18):4000–4015, 2016.

[103] P. W. Anderson and E. I. Blount. Symmetry considerations on Martensitic transformations: "Ferroelectric" metals? *Physical Review Letters*, 14(7):217–219, 1965.

[104] Youguo Shi, Yanfeng Guo, Xia Wang, Andrew J. Princep, Dmitry Khalyavin, Pascal Manuel, Yuichi Michiue, Akira Sato, Kenji Tsuda, Shan Yu, Masao Arai, Yuichi Shirako, Masaki Akaogi, Nanlin Wang, Kazunari Yamaura, and Andrew T. Boothroyd. A ferroelectric-like structural transition in a metal. *Nature Materials*, 12(11):1024–1027, 2013.

[105] Zaiyao Fei, Wenjin Zhao, Tauno A. Palomaki, Bosong Sun, Moira K. Miller, Zhiying Zhao, Jiaqiang Yan, Xiaodong Xu, and David H. Cobden. Ferroelectric switching of a two-dimensional metal. *Nature*, 560(7718):336–339, 2018.

[106] Pankaj Sharma, Fei-Xiang Xiang, Ding-Fu Shao, Dawei Zhang, Evgeny Y Tsymbal, Alex R Hamilton, and Jan Seidel. A room-temperature ferroelectric semimetal. *Science advances*, 5(7):eaax5080, 2019.

[107] Meng Meng, Zhen Wang, Aafreen Fathima, Saurabh Ghosh, Mohammad Saghayezhian, Joel Taylor, Rongying Jin, Yimei Zhu, Sokrates T. Pantelides, Jiandi Zhang, E. W. Plummer, and Hangwen Guo. Interface-induced magnetic polar metal phase in complex oxides. *Nature Communications*, 10(1):1–7, 2019.

[108] H. J. Xiang. Origin of polar distortion in LiNbO3-type "ferroelectric" metals: Role of A-site instability and short-range interactions. *Physical Review B*, 90(9):094108, 2014.

[109] I Lo Vecchio, G Giovannetti, M Autore, P Di Pietro, A Perucchi, Jianfeng He, K Yamaura, M Capone, and S Lupi. Electronic correlations in the ferroelectric metallic state of LiOsO3. *Physical Review B*, 93(16):161113, 2016.

[110] H. M. Liu, Y. P. Du, Y. L. Xie, J. M. Liu, Chun Gang Duan, and Xiangang Wan. Metallic ferroelectricity induced by anisotropic unscreened Coulomb interaction in LiOsO3. *Physical Review B - Condensed Matter and Materials Physics*, 91(6):2–7, 2015.

[111] Awadhesh Narayan. Effect of strain and doping on the polar metal phase in LiOsO 3. *Journal of Physics: Condensed Matter*, 32(12):125501, 2020.

[112] Y. R. Wang, S. Wang, H. L. Tao, Y. Cui, S. M. Liu, M. He, B. Song, and Z. H. Zhang. Electronic structure of LiOsO3: Electron energy-loss spectroscopy and first-principles study. *Solid State Communications*, 323(June 2020), 2021.

[113] Feng Jin, Le Wang, Anmin Zhang, Jianting Ji, Youguo Shi, Xiaoqun Wang, Rong Yu, Jiandi Zhang, E. W. Plummer, and Qingming Zhang. Raman interrogation of the ferroelectric phase transition in polar metal LiOsO 3. *Proceedings of the National Academy of Sciences*, 116(41):20322–20327, 2019.

[114] Jun-Yi Shan, A. de la Torre, N. J. Laurita, L. Zhao, C. D. Dashwood, D. Puggioni, C. X. Wang, K. Yamaura, Y. Shi, J. M. Rondinelli, and David Hsieh. Evidence for an extended critical fluctuation region above the polar ordering transition in LiOsO3. *Physical Review Research*, 2(3):033174, 2020.

[115] Zegnet Yimer and Huaxiang Fu. Origin of the persistence of soft modes in metallic ferroelectrics. *Physical Review B*, 101(17):174105, 2020.

[116] Saurabh Ghosh, Albina Y. Borisevich, and Sokrates T. Pantelides. Engineering an Insulating Ferroelectric Superlattice with a Tunable Band Gap from Metallic Components. *Physical Review Letters*, 119(17):177603, 2017.

[117] Asier Zabalo and Massimiliano Stengel. Switching a Polar Metal via Strain Gradients. *Physical Review Letters*, 126(12):127601, 2021.

[118] Rui Chun Xiao, Ding Fu Shao, Wenjuan Huang, and Hua Jiang. Electrical detection of ferroelectriclike metals through the nonlinear Hall effect. *Physical Review B*, 102 (2):1–7, 2020.

[119] Salva Salmani-Rezaie, Kaveh Ahadi, and Susanne Stemmer. Polar Nanodomains in a Ferroelectric Superconductor. *Nano Letters*, 20(9):6542–6547, 2020.

[120] V. P. Mineev and Yu. Yoshioka. Optical activity of noncentrosymmetric metals. *Phys. Rev. B*, 81:094525, 2010.

[121] Danilo Puggioni, Gianluca Giovannetti, and James M. Rondinelli. Polar metals as electrodes to suppress the critical-thickness limit in ferroelectric nanocapacitors. *Journal of Applied Physics*, 124(17), 2018.

[122] Danilo Puggioni and James M. Rondinelli. Designing a robustly metallic noncenstrosymmetric ruthenate oxide with large thermopower anisotropy. *Nature Communications*, 5:1–9, 2014.

[123] T. H. Kim, D. Puggioni, Y. Yuan, L. Xie, H. Zhou, N. Campbell, P. J. Ryan, Y. Choi, J. W. Kim, J. R. Patzner, S. Ryu, J. P. Podkaminer, J. Irwin, Y. Ma, C. J. Fennie, M. S. Rzchowski, X. Q. Pan, V. Gopalan, J. M. Rondinelli, and C. B. Eom. Polar metals by geometric design. *Nature*, 533(7601):68–72, 2016.

[124] Shiming Lei, Mingqiang Gu, Danilo Puggioni, Greg Stone, Jin Peng, Jianjian Ge, Yu Wang, Baoming Wang, Yakun Yuan, Ke Wang, Zhiqiang Mao, James M. Rondinelli, and Venkatraman Gopalan. Observation of Quasi-Two-Dimensional Polar Domains and Ferroelastic Switching in a Metal, Ca 3 Ru 2 O 7. *Nano Letters*, 18(5): 3088–3095, 2018.

[125] Daniel Hickox-Young, Danilo Puggioni, and James M. Rondinelli. Persistent polar distortions from covalent interactions in doped BaTiO3. *Physical Review B*, 102(1): 1–11, 2020.

[126] T Kolodiazhnyi, M Tachibana, H Kawaji, J Hwang, and E Takayama-Muromachi. Persistence of ferroelectricity in BaTiO3 through the insulator-metal transition. *Physical review letters*, 104(14):147602, 2010.

[127] Chengliang Xia, Yue Chen, and Hanghui Chen. Coexistence of polar displacements and conduction in doped ferroelectrics: An ab initio comparative study. *Physical Review Materials*, 3(5):54405, 2019.

[128] J. J. Lu, X. Q. Liu, X. Ma, M. S. Fu, A. Yuan, Y. J. Wu, and X. M. Chen. Crystal structures, dielectric properties, and phase transition in hybrid improper ferroelectric Sr 3 Sn 2 O 7 -based ceramics. *Journal of Applied Physics*, 125(4):044101, 2019.

[129] Bu Hang Chen, Tu Lai Sun, Xiao Qiang Liu, Xiao Li Zhu, He Tian, and Xiang Ming Chen. Enhanced hybrid improper ferroelectricity in Sr3-xBaxSn2O7 ceramics with a Ruddlesden-Popper (R-P) structure. *Applied Physics Letters*, 116(4), 2020.

[130] Pauli Virtanen, Ralf Gommers, Travis E. Oliphant, Matt Haberland, Tyler Reddy, David Cournapeau, Evgeni Burovski, Pearu Peterson, Warren Weckesser, Jonathan Bright, Stéfan J. van der Walt, Matthew Brett, Joshua Wilson, K. Jarrod Millman, Nikolay Mayorov, Andrew R. J. Nelson, Eric Jones, Robert Kern, Eric Larson, CJ Carey, İlhan Polat, Yu Feng, Eric W. Moore, Jake Vand erPlas, Denis Laxalde, Josef Perktold, Robert Cimrman, Ian Henriksen, E. A. Quintero, Charles R Harris, Anne M. Archibald, Antônio H. Ribeiro, Fabian Pedregosa, Paul van Mulbregt, and SciPy 1. 0 Contributors. SciPy 1.0: Fundamental Algorithms for Scientific Computing in Python. *Nature Methods*, 17:261–272, 2020.

[131] Alessio Filippetti, Vincenzo Fiorentini, Francesco Ricci, Pietro Delugas, and Jorge Íñiguez. Prediction of a native ferroelectric metal. *Nature Communications*, 7(1): 11211, 2016.

[132] M. I. Aroyo and J. M. Perez-Mato. Symmetry-Mode Analysis of Displacive Phase Transitions using International Tables for Crystallography. *Acta Crystallographica Section A Foundations of Crystallography*, 54(1):19–30, 1998.

[133] Branton J. Campbell, Harold T. Stokes, David E. Tanner, and Dorian M. Hatch. ISODISPLACE : a web-based tool for exploring structural distortions. *Journal of Applied Crystallography*, 39(4):607–614, 2006.

[134] P. M. Woodward. Octahedral Tilting in Perovskites. I. Geometrical Considerations. *Acta Crystallographica Section B Structural Science*, 53(1):32–43, 1997.

[135] Nicole A Benedek, James M Rondinelli, Hania Djani, Philippe Ghosez, and Philip Lightfoot. Understanding ferroelectricity in layered perovskites: new ideas and insights from theory and experiments. *Dalton Transactions*, 44(23):10543–10558, 2015.

[136] Marianne Glerup, Kevin S. Knight, and Finn Willy Poulsen. High temperature structural phase transitions in srsno3 perovskite. *Materials Research Bulletin*, 40(3):507 – 520, 2005.

[137] Hongtao Yuan, Hidekazu Shimotani, Atsushi Tsukazaki, Akira Ohtomo, Masashi Kawasaki, and Yoshihiro Iwasa. High-density carrier accumulation in ZnO field-effect transistors gated by electric double layers of ionic liquids. *Advanced Functional Materials*, 19(7):1046–1053, 2009.

[138] Michele Kotiuga and Karin M. Rabe. High-density electron doping of SmNiO3 from first principles. *Physical Review Materials*, 3(11):115002, 2019.

[139] M. Porer, M. Fechner, M. Kubli, M. J. Neugebauer, S. Parchenko, V. Esposito, A. Narayan, N. A. Spaldin, R. Huber, M. Radovic, E. M. Bothschafter, J. M. Glownia, T. Sato, S. Song, S. L. Johnson, and U. Staub. Ultrafast transient increase of oxygen octahedral rotations in a perovskite. *arXiv*, 012005:1–5, 2019.

[140] Hiroshi Mizoguchi, Hank W. Eng, and Patrick M. Woodward. Probing the Electronic Structures of Ternary Perovskite and Pyrochlore Oxides Containing Sn4+ or Sb5+. *Inorganic Chemistry*, 43(5):1667–1680, 2004.

[141] N. J. Laurita, A. Ron, Jun-Yi Shan, D. Puggioni, N. Z. Koocher, K. Yamaura, Y. Shi, J. M. Rondinelli, and D. Hsieh. Evidence for the weakly coupled electron mechanism in an Anderson-Blount polar metal. *Nature Communications*, 10(1):3217, 2019.

[142] Siwen Li, Zhipeng Ye, Xiangpeng Luo, Gaihua Ye, Hyun Ho Kim, Bowen Yang, Shangjie Tian, Chenghe Li, Hechang Lei, Adam W. Tsen, Kai Sun, Rui He, and Liuyan Zhao. Magnetic field-induced quantum phase transitions in a van der Waals magnet. *Physical Review X*, 10:011075, 2020.

[143] Natalie M. Dawley, Eric J. Marksz, Aaron M. Hagerstrom, Gerhard H. Olsen, Megan E. Holtz, Veronica Goian, Christelle Kadlec, Jingshu Zhang, Xifeng Lu, Jasper A. Drisko, Reinhard Uecker, Steffen Ganschow, Christian J. Long, James C. Booth, Stanislav Kamba, Craig J. Fennie, David A. Muller, Nathan D. Orloff, and Darrell G. Schlom. Targeted chemical pressure yields tuneable millimetre-wave dielectric. *Nature Materials*, 19(2):176–181, 2020.

[144] Yukio Hinatsu and Keitaro Tezuka. Electron Paramagnetic Resonance Study of Pr4+Ions Doped in BaSnO3, Ba2SnO4, and Ba3Sn2O7. *Journal of Solid State Chemistry*, 138(2):329–333, 1998.

[145] Abhinav Prakash, John Dewey, Hwanhui Yun, Jong Seok Jeong, K. Andre Mkhoyan, and Bharat Jalan. Hybrid molecular beam epitaxy for the growth of stoichiometric BaSnO3. *Journal of Vacuum Science & Technology A: Vacuum, Surfaces, and Films*, 33(6):060608, 2015.

[146] Hanjong Paik, Zhen Chen, Edward Lochocki, Ariel Seidner H., Amit Verma, Nicholas Tanen, Jisung Park, Masaki Uchida, Shunli Shang, Bi-Cheng Zhou, Mario Brützam, Reinhard Uecker, Zi-Kui Liu, Debdeep Jena, Kyle M. Shen, David A. Muller, and Darrell G. Schlom. Adsorption-controlled growth of La-doped BaSnO3 by molecular-beam epitaxy. *APL Materials*, 5(11):116107, 2017.

[147] A.M. Goldman. Electrostatic Gating of Ultrathin Films. *Annual Review of Materials Research*, 44(1):45–63, 2014.

[148] Satria Zulkarnaen Bisri, Sunao Shimizu, Masaki Nakano, and Yoshihiro Iwasa. Endeavor of Iontronics: From Fundamentals to Applications of Ion-Controlled Electronics. *Advanced Materials*, 29(25):1607054, 2017.

[149] Chris Leighton. Electrolyte-based ionic control of functional oxides. *Nature Materials*, 18(1):13–18, 2019.

[150] Haricharan Padmanabhan, Yoonsang Park, Danilo Puggioni, Yakun Yuan, Yanwei Cao, Lev Gasparov, Youguo Shi, Jak Chakhalian, James M. Rondinelli, and Venkatraman Gopalan. Linear and nonlinear optical probe of the ferroelectric-like phase transition in a polar metal, LiOsO 3. *Applied Physics Letters*, 113(12):122906, 2018.

[151] Andrew Mulder. *Ferroelectricity Coupled To Octahedral Rotations In Perovskite Oxides From First Principles*. PhD thesis, Cornell University, 2016.

[152] Sabine N Neal, Shutong Li, Turan Birol, and Janice L Musfeldt. Chemical bonding and born charge in 1t-hfs2. *npj 2D Materials and Applications*, 5(1):1–8, 2021.

[153] Qi-C Sun, Xiaoshan Xu, Sheila N Baker, Andrew D Christianson, and Janice L Musfeldt. Experimental determination of ionicity in mno nanoparticles. *Chemistry of Materials*, 23(11):2956–2960, 2011.

[154] BJ Kim, Hosub Jin, SJ Moon, J-Y Kim, B-G Park, CS Leem, Jaejun Yu, TW Noh, C Kim, S-J Oh, et al. Novel $J_{eff}$=1/2 mott state induced by relativistic spin-orbit coupling in $Sr_2IrO_4$. *Phys. Rev. Lett.*, 101(7):076402, 2008.

[155] Turan Birol and Kristjan Haule. $J_{eff}$=1 /2 Mott-insulating state in Rh and Ir fluorides. *Phys. Rev. Lett.*, 114(9):096403, 2015.

[156] Berend Zwartsenberg, Ryan P Day, Elia Razzoli, Matteo Michiardi, Nan Xu, Ming Shi, Jonathan D Denlinger, Guixin Cao, Stuart Calder, Kentaro Ueda, et al. Spin-orbit-controlled metal–insulator transition in $Sr_2IrO_4$. *Nat. Phys.*, 16(3):290–294, 2020.

[157] Gang Cao, Jasminka Terzic, HD Zhao, H Zheng, Lance E De Long, and Peter S Riseborough. Electrical control of structural and physical properties via strong spin-orbit interactions in $Sr_2IrO_4$. *Phys. Rev. Lett.*, 120(1):017201, 2018.

[158] G Cao, JE Crow, RP Guertin, PF Henning, CC Homes, M Strongin, DN Basov, and E Lochner. Charge density wave formation accompanying ferromagnetic ordering in quasi-one-dimensional $BaIrO_3$. *J. Phys. C*, 113(11):657–662, 2000.

[159] Q Chen, A Verrier, D Ziat, AJ Clune, R Rouane, X Bazier-Matte, G Wang, Stuart Calder, Keith M Taddei, CR dela Cruz, et al. Realization of the orbital-selective Mott state at the molecular level in $Ba_3LaRu_2O_9$. *Phys. Rev. Mater.*, 4:064409, 2020.

[160] John Singleton, Jae Wook Kim, Craig V. Topping, Anders Hansen, Eun-Deok Mun, S. Chikara, I. Lakis, Saman Ghannadzadeh, Paul Goddard, Xuan Luo, Yoon Seok Oh, Sang-Wook Cheong, and Vivien S. Zapf. Magnetic properties of sr 3 niiro 6 and sr 3 coiro 6: Magnetic hysteresis with coercive fields of up to 55 t. *Physical Review B*, 94(22):224408, 2016.

[161] Kenneth R. O'Neal, Arpita Paul, Amal Al-Wahish, Kendall D. Hughey, Avery L. Blockmon, Xuan Luo, Sang-Wook Cheong, Vivien S. Zapf, Craig V. Topping, John Singleton, Mykhalo Ozerov, Turan Birol, and Janice L. Musfeldt. Spin–lattice and electron–phonon coupling in 3d/5d hybrid Sr3NiIrO6. *npj Quantum Materials*, 4(1): 48, 2019.

[162] Yandong Ma, Liangzhi Kou, Baibiao Huang, Ying Dai, and Thomas Heine. Two-dimensional ferroelastic topological insulators in single-layer Janus transition metal dichalcogenides MSSe (M=Mo, W). *Phys. Rev. B*, 98(8):085420, 2018.

[163] Qirong Yao, Lijie Zhang, Pantelis Bampoulis, and Harold J.W. Zandvliet. Nanoscale investigation of defects and oxidation of $HfSe_2$. *J. Phys. Chem. C*, 122(44):25498–25505, 2018.

[164] Hui ZZhu, Qingxiao Wang, Lanxia Cheng, Rafik Addou, Jiyoung Kim, Moon J Kim, and Robert M Wallace. Defects and surface structural stability of $MoTe_2$ under vacuum annealing. *ACS Nano*, 11(11):11005–11014, 2017.

[165] Chen Chen, Jisun Kim, Yifan Yang, Guixin Cao, Rongying Jin, and EW Plummer. Surface phases of the transition-metal dichalcogenide $IrTe_2$. *Phys. Rev. B*, 95(9): 094118, 2017.

[166] Shin-ichiro Ideta, Dongfang Zhang, Arend G Dijkstra, Sergey Artyukhin, Sercan Keskin, Roberto Cingolani, Takahiro Shimojima, Kyoko Ishizaka, Hiroyuki Ishii, Kazutaka Kudo, et al. Ultrafast dissolution and creation of bonds in $IrTe_2$ induced by photodoping. *Sci. Adv.*, 4(7):aar3867, 2019.

[167] Gheorghe-Lucian Pascut, Kristjan Haule, Matthias J Gutmann, Sarah A Barnett, Alessandro Bombardi, Sergey Artyukhin, Turan Birol, David Vanderbilt, JJ Yang, and S-W Cheong. Dimerization-induced cross-layer quasi-two-dimensionality in metallic $IrTe_2$. *Phys. Rev. Lett.*, 112(8):086402, 2014.

[168] Kai Jiang, Anyang Cui, Sen Shao, Jiajia Feng, Hongliang Dong, Bin Chen, Yanchao Wang, Zhigao Hu, and Junhao Chu. New pressure stabilization structure in two-dimensional $PtSe_2$. *J. Phys. Chem. Lett.*, 11:73427349, 2020.

[169] Roman Kempt, Agnieszka Kuc, and Thomas Heine. Two-dimensional noble-metal chalcogenides and phosphochalcogenides. *Angew. Chem. Int. Ed.*, 59(24):9242–9254, 2020.

[170] Azimkhan Kozhakhmetov, Joseph R Nasr, Fu Zhang, Ke Xu, Natalie C Briggs, Rafik Addou, Robert Wallace, Susan K Fullerton-Shirey, Mauricio Terrones, Saptarshi Das, et al. Scalable BEOL compatible 2D tungsten diselenide. *2D Mater.*, 7(1):015029, 2020.

[171] Suraj S Cheema, Daewoong Kwon, Nirmaan Shanker, Roberto Dos Reis, Shang-Lin Hsu, Jun Xiao, Haigang Zhang, Ryan Wagner, Adhiraj Datar, Margaret R McCarter, et al. Enhanced ferroelectricity in ultrathin films grown directly on silicon. *Nature*, 580(7804):478–482, 2020.

[172] Hyun-Jae Lee, Minseong Lee, Kyoungjun Lee, Jinhyeong Jo, Hyemi Yang, Yungyeom Kim, Seung Chul Chae, Umesh Waghmare, and Jun Hee Lee. Scale-free ferroelectricity induced by flat phonon bands in $HfO_2$. *Science*, 67:1–10, 2020.

[173] Toshiki Iwasaki, Noritaka Kuroda, and Yuichiro Nishina. Anisotropy of lattice dynamical properties of $ZrS_2$ and $HfS_2$. *J. Phys. Soc. Japan*, 51(7):2233–22440, 1982.

[174] M Traving, T Seydel, L Kipp, M Skibowski, F Starrost, EE Krasovskii, A Perlov, and W Schattke. Combined photoemission and inverse photoemission study of $HfS_2$. *Phys. Rev. B*, 63(3):035107, 2001.

[175] Toru Kanazawa, Tomohiro Amemiya, Atsushi Ishikawa, Vikrant Upadhyaya, Kenji Tsuruta, Takuo Tanaka, and Yasuyuki Miyamoto. Few-layer $HfS_2$ transistors. *Sci. Rep.*, 6:22277, 2016.

[176] Liping Xu, Hao Xiong, Zhichao Fu, Menghan Deng, Shuiyuan Wang, Jinzhong Zhang, Liyan Shang, Kai Jiang, Yawei Li, Liangqing Zhu, et al. Ultrasensitive phototransistors based on few-layered $HfS_2$. *Adv. Mater.*, 27:7881–7887, 2015.

[177] Sina Najmaei, Mahesh R Neupane, Barbara M Nichols, Robert A Burke, Alexander L Mazzoni, Matthew L Chin, Daniel A Rhodes, Luis Balicas, Aaron D Franklin, and Madan Dubey. Cross-plane carrier transport in van der Waals layered materials. *Small*, 14(20):1–11, 2018.

[178] Larbi Roubi and Gosmo Garlone. Resonance Raman spectrum of $HfS_2$ and $ZrS_2$. *Phys. Rev. B*, 37(12):6808–6812, 1988.

[179] Shin-ichi Uchida and Shoji Tanaka. Optical phonon modes and localized effective charges of transition-metal dichalcogenides. *J. Phys. Soc. Japan*, 45(1):153–161, 1978.

[180] G. Lucovsky, R. M. White, J. A. Benda, and J. F. Revelli. Infrared-reflectance spectra of layered group-IV and group-VI transition-metal dichalcogenides. *Phys. Rev. B*, 7 (8):3859–3870, 1973.

[181] Jianyong Chen. Phonons in bulk and monolayer $HfS_2$ and possibility of phonon-mediated superconductivity: A first-principles study. *Solid State Commun.*, 237-238: 14–18, 2016.

[182] J Ibáñez, T Woźniak, F Dybala, R Oliva, S Hernández, and R Kudrawiec. High-pressure Raman scattering in bulk $HfS_2$: comparison of density functional theory methods in layered $MS_2$ compounds (M = Hf, Mo) under compression. *Sci. Rep.*, 8 (1):1–10, 2018.

[183] Lei Fu, Feng Wang, Bin Wu, Nian Wu, Wei Huang, Hanlin Wang, Chuanhong Jin, Lin Zhuang, Jun He, Lei Fu, et al. van der Waals epitaxial growth of atomic layered $HfS_2$ crystals for ultrasensitive near-infrared phototransistors. *Adv. Mater.*, 29(32): 1700439, 2017.

[184] Wenlun Zhang, Seiko Netsu, Toru Kanazawa, Tomohiro Amemiya, and Yasuyuki Miyamoto. Effect of increasing gate capacitance on the performance of a p-$MoS_2$/$HfS_2$ van der Waals heterostructure tunneling field-effect transistor. *Japn. J. Appl. Phys.*, 58:SBBH02, 2019.

[185] Jun Kang, Hasan Sahin, and Francois M. Peeters. Mechanical properties of monolayer sulphides: a comparative study between $MoS_2$, $HfS_2$, and $TiS_3$. *Phys. Chem. Chem. Phys.*, 17:27742–27749, 2015.

[186] Deobrat Singh, Sanjeev K. Gupta, Yogesh Sonvane, Ashok Kumar, and Rajeev Ahuja. 2D-$HfS_2$ as an efficient photocatalyst for water splitting. *Catal. Sci. and Technol.*, 6 (17):6605–6614, 2016.

[187] Denggui Wang, Junhua Meng, Xingwang Zhang, Gencai Guo, Zhigang Yin, Heng Liu, Likun Cheng, Menglei Gao, Jingbi You, and Ruzhi Wang. Selective direct growth of atomic layered $HfS_2$ on hexagonal boron nitride for high performance photodetectors. *Chem. Mater.*, 30(11):3819–3826, 2018.

[188] Ninghua Wu, Xu Zhao, Xu Ma, Qianqian Xin, Xiaomeng Liu, Tianxing Wang, and Shuyi Wei. Strain effect on the electronic properties of 1T-$HfS_2$ monolayer. *Physica E*, 93:1–5, 2017.

[189] Mailing Berwanger, Rajeev Ahuja, and Paulo Cesar Piquini. $HfS_2$ and $TiS_2$ monolayers with adsorbed C, N, P atoms: A first principles study. *Catalysts*, 10(94): catal10010094, 2020.

[190] Binjie Zheng, Yuanfu Chen, Zegao Wang, Fei Qi, Zhishuo Huang, Xin Hao, Pingjian Li, Wanli Zhang, and Yanrong Li. Vertically oriented few-layered $HfS_2$ nanosheets: Growth mechanism and optical properties. *2D Mater.*, 3(3):035024, 2016.

[191] Chengan Lei, Yandong Ma, Xilong Xu, Ting Zhang, Baibiao Huang, and Ying Dai. Broken-gap type-III band alignment in $WTe_2/HfS_2$ van der Waals heterostructure. *J. Phys. Chem. C*, 123(37):23089–23095, 2019.

[192] P. E. Blöchl. Projector augmented-wave method. *Phys. Rev. B*, 50(24):17953, 1994.

[193] G. Kresse and J. Furthmüller. Efficient iterative schemes for ab initio total-energy calculations using plane-wave basis set. *Phys. Rev. B*, 54(16):11169–11186, 1996.

[194] R. W. Nunes and Xavier Gonze. Berry-phase treatment of the homogeneous electric field perturbation in insulators. *Phys. Rev. B*, 63:155107, 2001.

[195] Ivo Souza, Jorge Íñiguez, and David Vanderbilt. First-principles approach to insulators in finite electric fields. *Phys. Rev. Lett.*, 89:117602, 2002.

[196] Stefano Baroni, Paolo Giannozzi, and Andrea Testa. Green's-function approach to linear response in solids. *Phys. Rev. Lett.*, 58(18):1861–1864, 1987.

[197] Jianwei Sun, Martijn Marsman, Gábor I Csonka, Adrienn Ruzsinszky, Pan Hao, Yoon-Suk Kim, Georg Kresse, and John P Perdew. Self-consistent meta-generalized gradient approximation within the projector-augmented-wave method. *Phys. Rev. B*, 84: 035117, 2011.

[198] Jochen Heyd, Gustavo E Scuseria, and Matthias Ernzerhof. Hybrid functionals based on a screened coulomb potential. *J. Chem. Phys.*, 118(18):8207–8215, 2003.

[199] David L Greenaway and Rudolf Nitsche. Preparation and optical properties of group IV–$VI_2$ chalcogenides having the $CdI_2$ structure. *J. Phys. Chem. Solids*, 26(9):1445–1458, 1965.

[200] M Yagmurcukardes, S Ozen, Fadıl Iyikanat, François M Peeters, and H Sahin. Raman fingerprint of stacking order in $HfS_2$- $Ca(OH)_2$ heterobilayer. *Phys. Rev. B*, 99(20): 205405, 2019.

[201] Nicola Marzari and David Vanderbilt. Maximally localized generalized Wannier functions for composite energy bands. *Phys. Rev. B*, 56(20):12847–12865, 1997.

[202] Nicola Marzari, Polytechnique Fe, Jonathan R Yates, and David Vanderbilt. Maximally localized Wannier functions : Theory and applications. *Rev. Mod. Phys.*, 84 (December):1419–1475, 2012.

[203] Arash A Mostofi, Jonathan R Yates, Giovanni Pizzi, Young-Su Lee, Ivo Souza, David Vanderbilt, and Nicola Marzari. An updated version of wannier90: A tool for obtaining maximally-localised wannier functions. *Comput. Phys. Commun.*, 185(8):2309 – 2310, 2014.

[204] Ph. Ghosez, J.-P. Michenaud, and X. Gonze. The physics of dynamical atomic charges: the case of $ABO_3$ compounds. *Phys. Rev. B*, 58(10):6224–6240, 1998.

[205] Qi-C Sun, Dipanjan Mazumdar, Lena Yadgarov, Rita Rosentsveig, Reshef Tenne, and Janice L Musfeldt. Spectroscopic determination of phonon lifetimes in rhenium-doped $MoS_2$ nanoparticles. *Nano Lett.*, 13(6):2803–2808, 2013.

[206] Qi C. Sun, Xiaoshan Xu, L. I. Vergara, Rita Rosentsveig, and Janice L. Musfeldt. Dynamical charge and structural starin in inorganic fullerenelike $MoS_2$ nanoparticles. *Phys. Rev. B*, 79:205405, 2009.

[207] T. J. Wieting and J. L. Verble. Infrared and Raman studies of long-wavelength optical phonons in hexagonal $MoS_2$. *Phys. Rev. B*, 3(12):4286–4292, 1971.

[208] Philippe Ghosez and Xavier Gonze. Band-by-band decompositions of the born effective charges. *J. Condens. Matter Phys.*, 12(43):9179–9188, 2000.

[209] Nicholas A Pike, Benoit Van Troeye, Antoine Dewandre, Guido Petretto, Xavier Gonze, Gian-Marco Rignanese, and Matthieu J Verstraete. Origin of the counterintuitive dynamic charge in the transition metal dichalcogenides. *Phys. Rev. B*, 95: 201106, 2017.

[210] Haijun Zhang, Chao-Xing Liu, Xiao-Liang Qi, Xi Dai, Zhong Fang, and Shou-Cheng Zhang. Topological insulators in bi2se3, bi2te3 and sb2te3 with a single dirac cone on the surface. *Nature physics*, 5(6):438–442, 2009.

[211] Liang Chen, Yingying Zhang, Xiaojia Wang, Bharat Jalan, Shuangtao Chen, and Yu Hou. Roles of Point Defects in Thermal Transport in Perovskite Barium Stannate. *Journal of Physical Chemistry C*, 122(21):11482–11490, 2018.

[212] Mingjian Wen and Ellad B Tadmor. Hybrid neural network potential for multilayer graphene. *Physical Review B*, 100(19):195419, 2019.

[213] Zhantao Chen, Nina Andrejevic, Tess Smidt, Zhiwei Ding, Qian Xu, Yen-Ting Chi, Quynh T Nguyen, Ahmet Alatas, Jing Kong, and Mingda Li. Direct prediction of phonon density of states with euclidean neural networks. *Advanced Science*, 8(12): 2004214, 2021.

[214] Linfeng Zhang, Jiequn Han, Han Wang, Roberto Car, and EJPRL Weinan. Deep potential molecular dynamics: a scalable model with the accuracy of quantum mechanics. *Physical review letters*, 120(14):143001, 2018.

[215] Hwanhui Yun, Mehmet Topsakal, Abhinav Prakash, Bharat Jalan, Jong Seok Jeong, Turan Birol, and K Andre Mkhoyan. Metallic line defect in wide-bandgap transparent perovskite basno3. *Science advances*, 7(3):eabd4449, 2021.